Measuring the Nuclear Level Density and γ-Decay Strength for the ^{92}Sr(n, γ) Reaction

by

Adriana Sweet

A dissertation submitted in partial satisfaction of the

requirements for the degree of

Doctor of Philosophy

in

Engineering – Nuclear Engineering

in the

Graduate Division

of the

University of California, Berkeley

Committee in charge:

Professor Jasmina Vujic, Chair
Adjunct Professor Lee A. Bernstein
Professor Michael Nacht
Dr. Darren L. Bleuel

Summer 2020

Measuring the Nuclear Level Density and γ-Decay Strength for the ^{92}Sr(n, γ) Reaction

Copyright 2020
by
Adriana Sweet

Abstract

Measuring the Nuclear Level Density and γ-Decay Strength for the ^{92}Sr(n, γ) Reaction

by

Adriana Sweet

Doctor of Philosophy in Engineering – Nuclear Engineering

University of California, Berkeley

Professor Jasmina Vujic, Chair

Neutron-induced reaction cross sections on short-lived neutron-rich nuclei, such as fission fragments play a crucial role for a wide range of nuclear physics applications, from nuclear energy and astrophysics to U.S. stockpile stewardship and other national security missions. However, our ability to model these cross sections are limited by theoretical uncertainties that range over orders of magnitude. Indirect methods are utilized to determine cross sections when direct measurements are not possible. These indirect methods can provide an experimental constraint on nuclear properties used in determining the (n,γ) cross section using Hauser-Feshbach reaction modeling including the nuclear level density (NLD), γ-ray strength function (γSF), and parameterizations of the optical model potential. One example of this is the fission fragment ^{92}Sr. The direct measurement of ^{92}Sr neutron-capture cross section is not possible, as the half-life of 2.66 hours is too short to allow the manufacturing of a target and subsequent irradiation of the target using neutrons. While it may not be possible to measure neutron capture on ^{92}Sr, β decay of ^{93}Rb (Q=7.466(9) MeV) can be used to probe average nuclear properties of the ^{93}Sr compound nucleus. In this dissertation we present the results of such a study where the emitted β-delayed γ rays were measured using a total absorption spectrometer (TAS) known as the Summing NaI(Tl) detector (SuN) to simultaneously determine the γ-ray energies and excitation energies. The experiment utilized a combination of the SuN detector together with a plastic scintillator to measure coincidence events with the emitted β particle, and a Tape Station for Active Nuclei (SuNTAN) to remove γ-ray background from the decay daughter activity. The measured ^{93}Sr γ-ray energies as a function of excitation energy were analyzed using the β-Oslo Method to extract statistical nuclear properties that were implemented in the reaction code TALYS. The resulting calculated ^{92}Sr neutron capture cross section is constrained by the experimental uncertainty and systematic uncertainties of the β-Oslo Method.

To Moya and Toya,

who spent my childhood summers raising me and teaching me to love learning.

Contents

Contents **ii**

List of Figures **v**

List of Tables **viii**

List of Abbreviations **ix**

List of Symbols **x**

1 Introduction **1**
1.1 Nuclear Fission 1
1.2 Nuclear Stockpile Security 4
1.3 Cosmogenic Nucleosynthesis 7
1.4 Thesis Outline 8

2 Underlying Nuclear Theory **10**
2.1 β Decay 12
2.1.1 Kinematics of β Decay 13
2.1.2 Classification of β Decays 14
2.1.3 Fermi Theory of β Decay 15
2.1.4 Angular Momentum Distributions 18
2.1.5 β-delayed Neutron Emission 18
2.1.6 β-delayed γ Emission 20
2.2 The Nuclear Level Density 21
2.2.1 Constant Temperature Model 22
2.2.2 The Back-Shifted Fermi Gas Model 22
2.2.3 Additional Phenomenological Models 23
2.2.4 Microscopic Models 25
2.2.5 Experimental Determination of Nuclear Level Density 26
2.3 The γ-ray Strength Function 26
2.3.1 γ-ray Emission 28
2.3.2 Porter-Thomas 30

2.3.3 Photon Response in Nuclei . . . 30
2.3.4 γ-Ray Strength Function Models . . . 33
2.3.5 Indirect Techniques for Extracting γSF from Experimental Data . . . 34
2.4 Optical Model Potential . . . 36
2.5 Hauser-Feshbach Formalism . . . 37
2.6 Databases of Neutron Resonance Parameters . . . 37

3 Experimental Setup: β decay of ^{93}Rb **43**
3.1 Thermalized Radioactive Isotope Beam . . . 43
3.2 Detector Setup . . . 44
3.2.1 Total Absorption Spectroscopy (TAS) . . . 44
3.2.2 Summing NaI(Tl) Detector (SuN) . . . 47
3.2.3 SuN Tape Transport of Active Nuclei (SuNTAN) . . . 49
3.3 Data Analysis . . . 51
3.3.1 ^{93}Sr Production . . . 53
3.3.2 Decay Products as Contamination . . . 58
3.4 Response Function for ^{93}Rb$\rightarrow$^{93}Sr Experiment . . . 62

4 Methodology: β-Oslo Method **66**
4.1 Unfolding the γ-Ray Spectra . . . 66
4.2 Distribution of First-Generation γ Rays . . . 69
4.3 Extraction of the Nuclear Level Density and γ-ray Strength Function . . . 72
4.4 Normalization of the Nuclear Level Density & γ-ray Strength Function . . . 74

5 Experimental Results **77**
5.1 ^{93}Rb Decay . . . 77
5.2 From β-γ Coincidence Data to Primary γ-ray Spectra . . . 78
5.3 Obtaining the Normalization Parameters . . . 82
5.4 Simultaneously-Extracted Nuclear Level Density and γ-ray Strength Function 87
5.5 Normalizing the Nuclear Level Density . . . 88
5.6 Normalizing the γ-ray Strength Function . . . 91
5.6.1 Limited Spin Population from the Initial β Decay . . . 92
5.6.2 Additional Normalization to Known Photoabsorption Data . . . 94

6 Neutron-Capture Cross Section Calculations **97**
6.1 Theoretical Reaction Calculation . . . 97
6.2 Final Calculation of ^{92}Sr(n,γ) Cross Section and Reaction Rate . . . 99
6.3 Propagation of Systematic Error . . . 99

7 Conclusion **104**
7.1 Summary . . . 104

7.2 Outlook 105
7.2.1 Future β-Oslo Experiments: ^{93,94,95}Sr(n,γ) 105
7.2.2 β-Delayed Neutron Emission Experiments 106

Bibliography **108**

A Fermi Theory Golden Rule **114**
A.1 Density of Final States for β Decay 114
A.2 Probability of γ Transition 115
A.3 Connecting Probability of γ Transition to Decay Width and Photoabsorption Cross Section 116

B Additional Phenomenological γ-Ray Strength Functions **118**
B.1 Kadmenskiĭ, Markushev, and Furman (KMF) model 118
B.2 Modified Lorentzian (MLO) model 118

C Additional Experimental Details **119**

D TALYS calculations of the ^{92}Sr(n,γ) cross section **121**

List of Figures

1.1 Fragment mass distribution as a function of fissioning nucleus. 2
1.2 β-Oslo experiment to determine the ^{92}Sr(n, γ) cross section 3
1.3 U.S. Nuclear Weapons Stockpile, 1962-2017 [11] 4
1.4 Fission products in a fission environment 5
1.5 Binding energy per nucleon 8
1.6 Comparison of observed and predicted abundances of Rb, Sr, Y and Zr [19] . . . 9

2.1 Chart of the Nuclides 12
2.2 Simulated β-decay spectrum for decay ^{93}Rb to second excited state of ^{93}Sr . . . 18
2.3 β-decay feeding intensities of ^{93}Rb and ^{93}Sr 19
2.4 ^{235}U(n, f) mass distribution 20
2.5 Known discrete levels from the NNDC 24
2.6 Experimental verification of the generalized Brink-Axel hypothesis for ^{64,65}Ni [49] 28
2.7 Dipole response in nuclei. 31
2.8 Giant resonance modes of the nucleus. 32
2.9 Photoabsorption data for Sr isotopes. 35
2.10 Systematics of Sr isotopes: Resonance spacing. 38
2.11 Systematics of Sr isotopes: Resonance width. 39
2.12 Systematics of Sr isotopes: Resonance width. 40

3.1 Determination of the ^{92}Sr neutron-capture cross section and fission product burn up 44
3.2 Experimental setup. (*Left*) Schematic of SuN and the Tape station for Active Nuclei (SunTAN). (*Right*) Experimental setup of SuN, fiber detector, and tape station (covered in blackout fabric) installed in the low-energy experiment area. 45
3.3 The level scheme of ^{93}Sr plotting the first few levels in a complete level scheme, where the number of level continues to increase with increasing excitation energy. 46
3.4 Chart of the nuclides in the A = 93 mass region. The direct measurement of the neutron-capture reaction of ^{92}Sr(n,γ) is inaccessible. Alternatively, the compound nucleus ^{93}Sr can also be formed by the β decay of ^{93}Rb. ^{93}Sr formed through β decay itself subsequently decays, which produces a decay daughter that is considered a contaminant in the experimental data. 47

3.5 Comparison of modified and original GEANT4 simulation of SuN 48
3.6 The Summing NaI(Tl) detector (SuN). (*Left*) Schematic and (*right*) cross-section along beam axial line. [74] 49
3.7 Simulated summing efficiency (open circles) plotted as a function of number of segments that "fired" $\langle N_s \rangle$ and fitted with a linear function (solid line) along with experimental results (red data point) from Reference [74]. 50
3.8 Fiber detector with PMT components. (*Left*) Schematic of fiber detector with attached fiberoptic cables connects to two PMTs. (*Center*) Cross sectional view in-line with beam axis of fiber detector, showing film (9-track tape) holder placed in the center of the fiber detector. (*Right*) Rear-view of the two PMTs located outside the SuN detector setup in a stainless steel PMT chamber. 50
3.9 Gain matched PMTs of SuN. 52
3.10 Calibrated segments of SuN. 53
3.11 ^{40}K background peak monitored through week-long experiment. 54
3.12 Radionuclides produced by the β-decay of ^{93}Rb. 55
3.13 Measured activity of daughter runs for ^{93}Rb experiment 58
3.14 Observed background activity throughout experiment 59
3.15 Observed background energy spectra throughout experiment 60
3.16 Measured activity of a production run for the ^{93}Rb experiment 61
3.17 TAS Spectra of raw β-gated excitation energy, time-gated decay of decay daughter, and isolated decays of parent nucleus ^{93}Rb. 61
3.18 γ-Ray Spectra of raw β-gated excitation energy, time-gated decay of decay daughter, and isolated decays of parent nucleus ^{93}Rb. 62
3.19 Raw 2D β-Oslo matrix for the decay of ^{93}Rb 63
3.20 Comparison of original and modified GEANT4 simulation of detector setup . . . 64
3.21 Comparison of the results of the original and the modified GEANT4 simulations of detector response to γ rays 65

4.1 A hypothetical decay scheme [85] 70
4.2 Hypothetical normalization parameters shifting the NLD and γSF 74

5.1 Parent and daughter TAS Spectra of raw β-gated excitation energy 79
5.2 Parent and daughter γ-Ray Spectra of raw β-gated excitation energy 80
5.3 Raw β-Oslo Matrices of Initial Measurement and Decay Contamination Removal 81
5.4 Unfolded and Primary β-Oslo Matrices of ^{93}Sr 82
5.5 Average γ-ray multiplicity of ^{93}Sr unfolded matrix 83
5.6 Raw, unfolded and primary γ-ray spectra of ^{93}Sr 84
5.7 Unfolded total, higher-generation, and primary γ-ray spectra of ^{93}Sr 85
5.8 Experimental and theoretical primary γ-ray spectra 88
5.9 Investigating the excitation and γ-ray energy thresholds for the ^{93}Sr primary γ matrix 89
5.10 Normalization Approaches applied to the extracted NLD of ^{93}Sr 90

5.11 Impact of decay daughter contamination in starting experimental β-Oslo matrix 92
5.12 Tabulated Spin Distribution of ^{93}Sr 93
5.13 γSF normalized using phenomenological and microscopic model approaches . . . 94
5.14 γSF normalized using estimated GDER parameters 95

6.1 Theoretically calculated cross section of ^{92}Sr(n,γ)^{93}Sr 98
6.2 Experimental cross section of ^{92}Sr(n,γ)^{93}Sr influenced by OMP 100
6.3 Experimentally determined cross section of ^{92}Sr(n,γ)^{93}Sr 101
6.4 NLD and γSF systematic error propagation to the experimentally determined neutron-capture cross section 102
6.5 Influence of an $M1$ upbend on the experimentally determined neutron-capture cross section 103

List of Tables

2.1 Classification of β-decay transitions 15

5.1 Calculated NLD Parameters for ^{93}Sr 85
5.2 Estimated NLD at Neutron Separation for ^{93}Sr 86
5.3 Estimated s-Wave Neutron-Resonance Spacing for ^{93}Sr 87
5.4 Tabulated Microscopic Model of the NLD for ^{93}Sr 87
5.5 Giant Electric Dipole Resonance Parameters for ^{93}Sr 88

6.1 Available Microscopic Models in TALYS 98

C.1 Final scaling factors after gain matching the SuN PMTs using the ^{40}K background peak. The label of individual PMTs refers to the top "T" or bottom "B" half of SuN and the first number refers to the segment of SuN, while the second number refers to the PMT within the segment. 119
C.2 Sources used in calibrated segments of SuN. 120

List of Abbreviations

γSF	γ-ray **S**trength **F**unction
NLD	**N**uclear **L**evel **D**ensity
CN	**C**ompound **N**ucleus
GS	**G**round **S**tate
$E1$	Electric Dipole
$E2$	Electric Quadrupole
$M1$	Magnetic Dipole
GDR	**G**iant **D**ipole **R**esonance
GDER	**G**iant **D**ipole **E**lectric **R**esonance
GDMR	**G**iant **D**ipole **M**agnetic **R**esonance
GQER	**G**iant **Q**uadrupole **E**lectric **R**esonance
NNDC	**N**ational **N**uclear **D**ata **C**enter
ENSDF	**E**valuated **N**uclear **S**tructure **D**ata **F**ile
ENDF	**E**valuated **N**uclear **D**ata **F**ile
RIPL	**R**eference **I**nput **P**arameter **L**ibrary
IAEA	**I**nternational **A**tomic **E**nergy **A**gency
BA	**B**rink-**A**xel
SLO	**S**tandard **Lo**rentzian
GLO	**G**eneral **Lo**rentzian
EGLO	**E**nhanced **G**eneral **Lo**rentzian
MLO	**M**odified **Lo**rentzian
KMF	**K**admensky-**M**arkushev-**F**urman
CTF	**C**onstant **T**emperature **F**ormula
BSFG	**B**ack-**S**hifted **F**ermi **G**as
SP	**S**ingle **P**article
ICC	**I**nternal **C**onversion **C**oefficients
SuN	**Su**mming **N**aI(Tl)
TAS	**T**otal **A**bsorption **S**pectrometer

List of Symbols

XL	multipole type
D_J	level spacing of spin J at excitation energy E
D_0	average neutron resonance spacing for s-wave neutrons
S_n	neutron separation energy
E_G	giant resonance peak energy
E_γ	γ-ray energy
E_x	excitation energy
E_i	initial excitation energy
E_f	final excitation energy
E_c	cut-off energy
$\overrightarrow{f}_{XL}$	strength function for photoexcitation by radiation of type X and multipolarity L
$\overleftarrow{f}_{XL}$	strength function for de-excitation by radiation of type X and multipolarity L
Γ_G	width of the giant resonance
$\langle\Gamma_0\rangle$	average total radiative width at the neutron separation energy
I_γ	Individual γ-ray intensity
J, J_t, J_{cs}, J_{gs}	spin of the compound, target, capture, and ground state, respectively
σ_G	peak giant dipole resonance cross section
σ	spin-cutoff parameter
$\rho(E, J, \pi)$	nuclear level density as a function of excitation energy E, spin J, and parity π
$g(E, J)$	spin distribution function
a	level density parameter

E_0, E_1	energy backshift for the Constant Temperature Formula and Back-Shifted Fermi Gas, respectively
T	nuclear temperature
$\mathscr{T}_{i\to f}^{XL}$	transition probability between an initial state i and a final state f by radiation of type X and multipolarity L
$\mathscr{B}_{i\to f}^{XL}$	reduced transition probability between an initial state i and a final state f by radiation of type X and multipolarity L
ϵ_0	vacuum permittivity

Acknowledgments

Throughout my nine years at UC Berkeley, I have been lucky in more ways than I can count. My entire college experience has truly shaped the person who I am today, both professionally and personally. During my early days in 2011 as a young freshman taking introductory physics classes, I could hardly have imagined that in 2020 I'd be sitting here now completing my doctoral dissertation. Moreover, considering the innumerable unknowns of the world today and how so many of our day-to-day interactions over the years will very likely remain changed in the coming years in ways we haven't yet imagined, I am now evermore sincerely grateful for each and every opportunity that I have had to develop personal and working relationships with National Lab colleagues, advisors and UC Berkeley professors.

The person who first made all of these academic relationships possible, whom I would like to thank first and foremost, is Dr. Bethany L. Goldblum. Dr. Goldblum hired me as an undergraduate research apprentice in 2013 at a time when I was only hoping to find my first opportunity for involvement in the field of nuclear physics. Throughout my undergraduate and graduate career at the Nuclear Science and Security Consortium (NSSC), Dr. Goldblum has been a shining example of research excellence and integrity. Her encouragement of me to develop beyond simply technical skills, but to focus on refining my scientific communication skills in particular, has enabled me to be able to effectively convey myself as a capable researcher across interdisciplinary fields and inspired me to pursue new areas of academic expertise. I will also dearly miss Dr. Goldblum's weekly Bay Area Neutron Group (BANG) meetings, which were a vibrant collaborative experience. My hope is that these meetings will continue to have as significant of an impact on other young researchers in the future as they had on me.

Dr. Jasmina Vujic has been a constant foundational support for me throughout my undergraduate and graduate careers as my academic advisor, and I feel that I am unable to adequately thank her for her patience and understanding with life's unexpected turns, and for her unwavering commitment to me as a student, researcher and scientist. I am extremely grateful for the numerous bridges that Dr. Vujic has created between UC Berkeley students, faculty, and National Lab scientists, which enabled the entirety of this dissertation work, and I would also like to thank Dr. Vujic for her attention to detail in helping me to craft and refine my Master's of Science thesis and Ph.D. dissertation.

I would also like to thank Dr. Lee A. Bernstein for his infectious enthusiasm that he brought (along with a side of Cheeseboard bread!) to NE101. To say that Dr. Bernstein is a physicist doesn't do him justice, as each class he taught demonstrated he is also a skilled storyteller. In Dr. Bernstein's classroom, I was not only learning the material of the curriculum, but was truly internalizing fundamental physics and was pushed to think more critically than ever before. In addition, I would like to thank Dr. Bernstein for the experts whom he brought into the classroom, such as Dr. Walid Younes and Dr. Augusto O. Macchiavelli, who are both inspirations to me.

Among the most impactful courses that I have taken at Cal have been Dr. Michael Nacht's U.S. nuclear security policy courses, through which he lends a unique perspective on

nuclear security and public policy that I believe cannot be found anywhere else but here in Berkeley, an institution with a deeply rooted history in the field of nuclear engineering. It has been such a pleasure to participate in Dr. Nacht's courses and to engage my colleagues in debates during our crisis simulations! Dr. Nacht in particular taught me that beyond just being part of such a long and storied institutional legacy, it is the responsibility of nuclear scientists from the Department of Nuclear Engineering at UC Berkeley to remain actively at the forefront of developing future U.S. nuclear security policy. I would like thank Dr. Nacht for training the next generation of nuclear scientists to be able to effectively communicate their work in their field to other researchers in a multidisciplinary environment.

To everyone in NSSC and BANG, I would like to express a heartfelt thanks. In particular, I would like to thank Charlotte Carr for her coordination of numerous NSSC events and incredible ability to manage last minute submission of presentations. I am also grateful to Dr. Josh Brown, Dr. Juan Jose Manfredi Jr, Dr. Christopher Stewart, Chris Brand, Gino Gabella, and Joseph Gordon, who helped me prepare for my oral qualifying examination through two months of rehearsal presentations. Thankfully, these rehearsals were also followed by our weekly Very Important Physics (VIP) meetings moderated by Dr. Darren L. Bleuel at Jupiter, where our physics quandary of the week was debated.

This work would also not have been possible without the Beam Physics Group and operators of the National Superconducting Cyclotron Laboratory (NSCL), Dr. Artemis Spyou, Dr. Sean Liddick, and their tireless band of students who facilitated the setup and takedown of countless experiments. I am also grateful to Dr. Spyrou and Dr. Liddick, with their wealth of experimental experience, for their advisement as I completed my dissertation. Specifically, I must extend my sincerest thanks to Dr. Spyrou and Dr. Mallory Smith for their 2:00 am troubleshooting capabilities, which helped me successfully complete my dissertation experiment!

Furthermore, I would like to thank the staff and students of the Physics Department at the University of Oslo for welcoming me in their research group for nearly three weeks. The immeasurably impactful experiences that I had whilst living and learning in Norway over the Summer of 2019 are entirely thanks to the efforts of Dr. Sunniva Siem and the Norwegian Research Council in developing a successful and enduring international collaboration between the University of Oslo and UC Berkeley. In particular, I would like to thank Dr. Ann-Cecilie Larsen, who took the time to thoroughly explain the "wibbly wobbly" ball of stuff that is the Oslo Method! I would also like to say *tusen takk* to my friends and colleagues Dr. Jørgen Eriksson Midtbø, Fabio Zeiser, Wanja Paulsen, and Nora Pettersen for introducing me to your research, as well as the introductory Norwegian lessons!

Moreover, my greatest personal growth as a scientist, researcher and down-right person is thanks to my LLNL mentor, Dr. Darren L. Bleuel, who's guidance, advice and support has encouraged and enabled me to strive for, achieve and take the most out of each one of these experiences and relationships that I've had the great fortune to develop throughout my academic career. I am most grateful for our weekly meetings, where we discussed the "meaning of error", to its excruciatingly minutest detail, and which often led to rabbit-holes that I was obsessively compelled to investigate. Thank you, Darren, for helping me over the

past 8 years to make my own contribution to the field of nuclear physics with my dissertation work, and for helping me to find the nuclear physics research direction and opportunities that I am passionate to pursue in the future. Most importantly, thank you for listening to my endless doubts and for giving me the personal confidence to keep persevering throughout my academic career, and I cannot stress enough how truly cathartic and meaningful VIP meetings have been (and continue to be!) at the end of a hard week where *t*hings *a*ren't *s*umming-up.)'(

Lastly, I would like to thank my husband, Eric Sweet, who deserves an honorary doctorate in Nuclear Engineering after the hours he's spent at VIP meetings hearing the ins and outs of nuclear physics, and now, hours he's spent with me as I write my dissertation into the wee hours of the morning. Eric is not only my rock, but simultaneously my favorite comfy sweater, here for me when I doubt myself most. We first met in freshman-year physics, and since then we have helped each other grow into our respective careers. Thank you for sharing each and every moment of the past nine years of college with me, nine years which would also not be possible without the support and love of my new family, the Sweets: Kevin, Suzanne, Zoe, and Liz, as well as my mother and father, Carmen and Adrian Ureche, and my aunt Tina Caloianu. Of course, I would be remised if I were to not also include my four-legged family, Lucy, Murphy, Phoebe, Henry, Duke, and Winnie (sort of); your unconditional love, support, and wet kisses that reminded me that I can do this.

The material featured in this dissertation is based upon work supported by the Department of Energy National Nuclear Security Administration through the NSSC under Award Number DE-NA0003180, and their support is most gratefully appreciated.

Disclaimer: This report was prepared as an account of work sponsored by an agency of the United States Government. Neither the United States Government nor any agency thereof, nor any of their employees, makes any warranty, express or limited, or assumes any legal liability or responsibility for the accuracy, completeness, or usefulness of any information, apparatus, product, or process disclosed, or represents that its use would not infringe privately owned rights. Reference herein to any specific commercial product, process, or service by trade name, trademark, manufacturer, or otherwise does not necessarily constitute or imply its endorsement, recommendation, or favoring by the United States Government or any agency thereof. The views and opinions of authors expressed herein do not necessarily state or reflect those of the United States Government or any agency thereof.

Chapter 1

Introduction

> *On account of their close packing and strong energy exchange, the particles in a heavy nucleus would be expected to move in a collective way which has some resemblance to the movement of a liquid drop. If the movement is made sufficiently violent by adding energy, such a drop may divide itself into two smaller drops.*
>
> — Lise Meitner and Otto R. Frisch, *Nature (1939)*

1.1 Nuclear Fission

The year 1939 is recognized as the year nuclear fission was discovered; however, the idea of fission stretches back four years prior to a paper by Ida Noddack, where she offers criticism on Fermi's announcement of possible transuranic elements [1, 2]. The proposed idea in her 1934 paper was that

> When heavy nuclei are bombarded by neutrons, it is conceivable that the nucleus breaks up into several large fragments, which would of course be isotopes of known elements but would not be neighbors of the irradiated element.

This concept reappeared in a number of papers in 1939 published by Otto Hahn and Fritz Strassmann [3, 4] as well as Lise Meitner and O. R. Frisch [5, 6]. At the Kaiser Wilhelm Institute for Chemistry of the University of Berlin, Hahn and Strassmann, having received input from Lise Meitner through correspondences via mail, officially discovered fission by chemical separation, which they referred to as "Uranspaltung (uranium fission)" in their 1939 paper that details the production of barium, strontium, yttrium, krypton, and xenon from uranium by neutron bombardment [4]. The day after this paper was published, February 11, 1939, Lise Meitner and O. R. Frisch published a paper in Nature which first used the word fission to describe this process, describing it in terms of the liquid drop model (LDM), where the nucleus continues to elongate until it breaks, resulting in a light and heavy fragment split [5]. Through decades of subsequent experimental research, the nuclear community's understanding of fission has evolved beyond the rudimentary picture of a nucleus simply splitting in two during a fission event, as it is now known that in addition to the fission fragments, neutrons, electrons, antineutrinos, γ's, and β-decay products are also produced

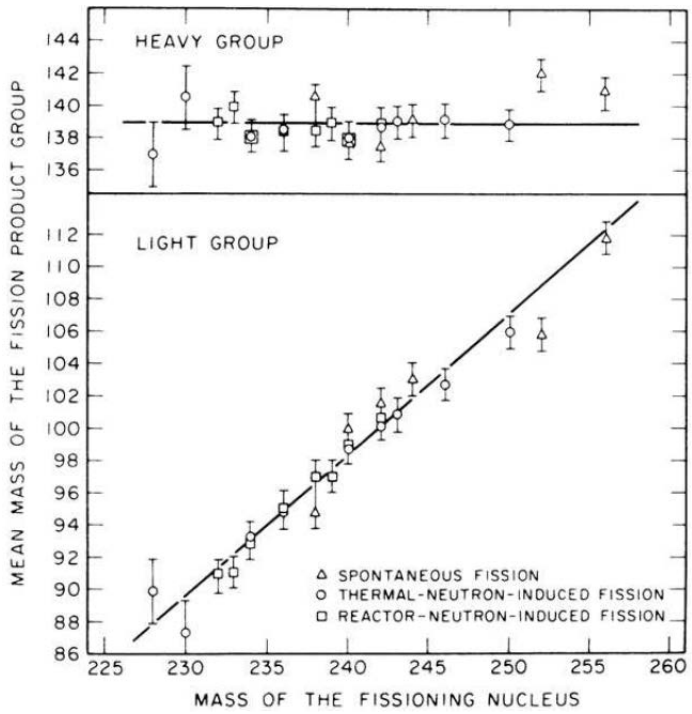
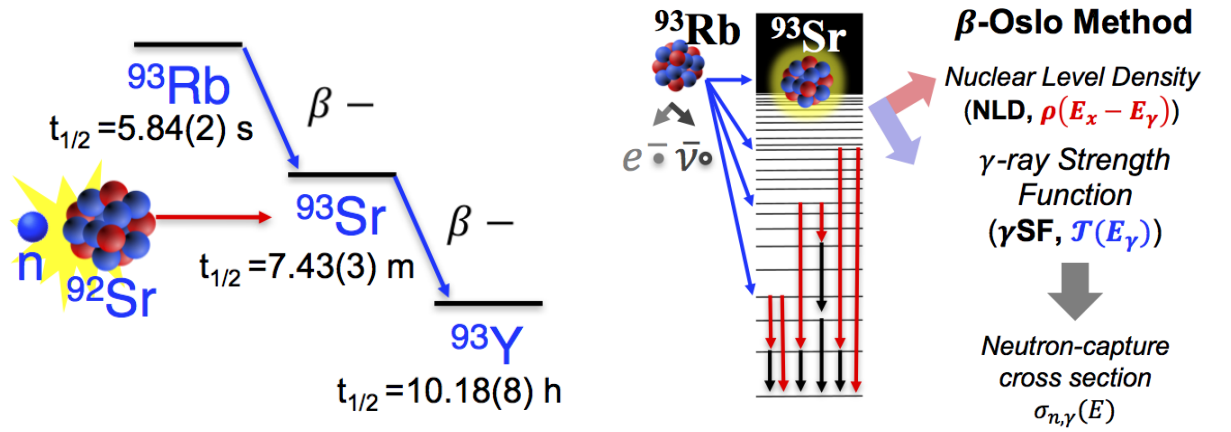


Figure 1.1: Fragment mass distribution curve as a function of fissioning nucleus [8].

within the first 10^{-18} and 10^{-6} seconds of a fission event [7]. Our improved understanding of the fundamental particle interactions that occur during fission has supported many practical applications of nuclear technology, such as nuclear power, the U.S. science-based Stockpile Stewardship Program, and the field of cosmogenic nucleosynthesis.

One important signature of neutron-induced fission on fissile material is the fragment mass distribution, where production favors a heavy fragment at about $A = 140$, and a light fragment with a mass as a linear function of the fissioning nucleus and a proton number at about $Z = 38$, as illustrated in Fig. 1.5 [8]. The production of the light fragment, a neutron-rich nucleus which undergoes further decay by β, γ, and delayed neutron emission, is particularly important, as its yield can be used to determine the number of prior fission events, making it a useful tool for the U.S. science-based Stockpile Stewardship mission.

Very little is currently known about the statistical properties of the unresolved highly-excited states in these nuclei which are key to modeling neutron capture rates on them. For instance, theoretical uncertainties for a single-isotope reaction rate can be between a single to several orders of magnitude. Moreover, the neutron-capture cross section, which describes the probability of a nucleus to capture a neutron, is an important set of statistical nuclear information which is difficult to directly measure; yet, well-determined neutron-capture cross sections are highly important for fields such as nuclear reactor physics, nuclear astrophysics, as well as are key to technical support of U.S. nuclear security and policy.



(a) Production of ^{93}Sr by β decay

(b) Schematic of β-Oslo Method

Figure 1.2: ^{93}Sr is (a) produced by neutron capture on ^{92}Sr or β decay of ^{93}Rb. ^{93}S is β-unstable, producing ^{93}Y. γ rays (b) emitted by β-populated states decay to states below. By using the β-Oslo Method the NLD and γSF are extracted from the distribution of measured γ rays [9, 10]. The NLD and γSF are used to determine the experimentally-constrained neutron-capture cross section: ^{92}Sr(n,γ)^{93}Sr.

As direct methods of measuring fission fragments are generally impossible, indirect methods, such as the β-Oslo Method, were developed to experimentally determine average properties of neutron-rich nuclei and calculate the neutron-capture cross section [9, 10]. The fission fragment ^{95}Sr, for example, has the highest independent yield of the $A = 95$ chain, and thus is a key nuclear data need for the U.S. science-based Stockpile Stewardship Program. To address the nuclear data need in neutron-induced cross section data, the aim of this dissertation is to experimentally constrain the statistical nuclear properties of ^{93}Sr, a neutron capture predecessor of ^{95}Sr, to improve theory-based predictions of heavier Sr isotopes.

The work presented here investigates the structure of ^{93}Sr through average nuclear properties such as the nuclear level density (NLD) and γ-ray strength function (γSF). These properties can be probed through γ-ray emission from highly excited states near the neutron separation energy where individual levels can no longer be resolved. As ^{92}Sr is a short-lived isotope, the neutron-capture reaction is not directly measurable, and thus by using the β-Oslo Method, the ^{93}Sr nucleus is accessible by β decay of ^{93}Rb as shown in Fig. 1.2a. Highly excited states near and above the neutron separation energy of ^{93}Sr are populated by β decay, following which, γ rays are emitted from these excited states to lower excited states or to the ground state as shown in Fig. 1.2b. The β-Oslo Method is used to extract from this distribution of γ rays the NLD and γSF, which are key ingredients in the Hauser-Feshbach calculation of the neutron-capture cross section.

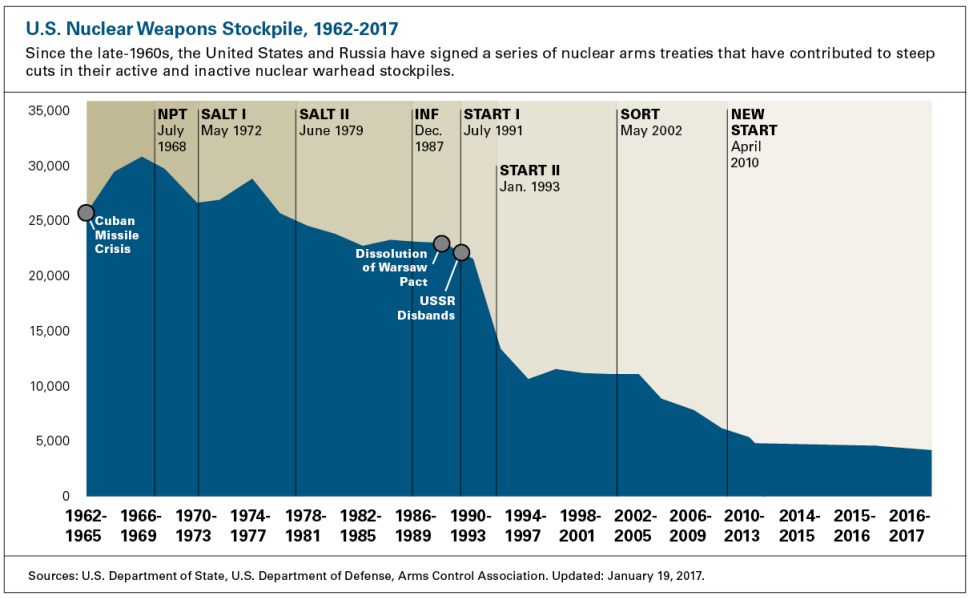


Figure 1.3: U.S. Nuclear Weapons Stockpile, 1962-2017 tracking the stockpile of nuclear weapons over course arms control treaties [11].

1.2 Nuclear Stockpile Security

The New STrategic Arms Reduction Treaty (New START), which limits the number of weapons in the United States and Russia's nuclear arsenals, is set to expire in February 2021, unless the two nations agree to a five year extension. Since the early days of nuclear testing, from the U.S.'s Trinity Test on July 16, 1945 and the Soviet Union's first nuclear weapon test, RDS-1, in 1949, a global arms race has led to the emergence of several nuclear weapon states (NWS). During the Cold War, nuclear deterrence theory, spearheaded by Bernard Brodie at the RAND Corporation, was adopted as the preferred strategy in attempt to discourage potential adversaries from pursuing nuclear war and control the proliferation of nuclear weapons, which began the long road to international nuclear nonproliferation and arms control agreements. Subsequently, several arms control treaties between the U.S. and the Russia were signed, ratified, and put into force [13]:

- Partial/Limited Test Ban Treaty (PTBT/LTBT) in 1963, which prohibited the testing of nuclear weapons in the atmosphere, underwater, and in outer space,
- Strategic Arms Control Treaty (SALT I) in 1972, which was the first major arms control agreement,
- Threshold Test Ban Treaty (TTBT) in 1974, which limited nuclear weapon tests to 150 kT,

- Strategic Arms Reduction Treaty I (START I) in 1994, which limits the number of strategic nuclear weapons,
- and New START in 2011, which reduced strategic nuclear weapons by half, i.e., 1550 warheads.

While these treaties limited the number and testing of nuclear weapons, the Comprehensive Test Ban Treaty (CTBT) signed in 1996 firmly prohibited nuclear testing in its entirety, yet the treaty was not ratified by the U.S. In the field of global security, a bilateral non-commitment from the U.S. and Russia to re-ratify expiring international arms control treaties, compounded by the U.S.'s withdrawal from the Anti-Ballistic Missile Treaty in 2002 and, more recently, from the Intermediate-Range Nuclear Forces Treaty (INF) in 2019 [14, 15], poses potentially considerable harm towards international nuclear disarmament efforts.

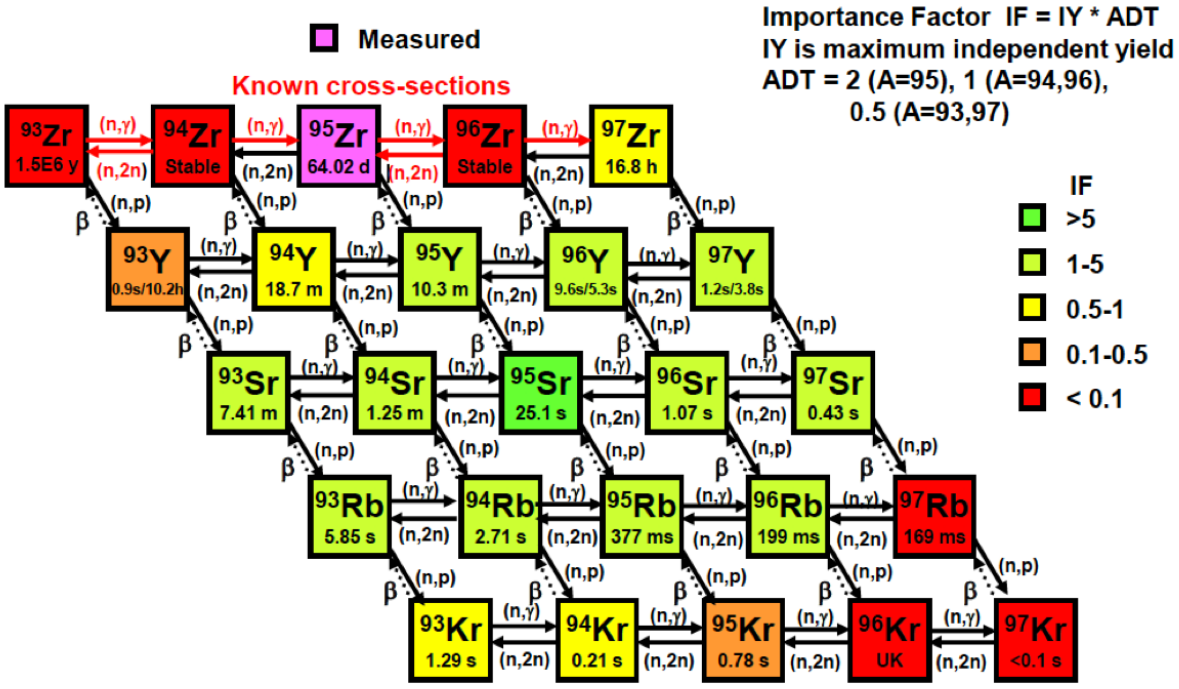


Figure 1.4: Chart of key reaction cross sections near A=95 [12]. To the right of the figure is a scale describing the importance of each isotope. The importance factor is a product of the independent fission yield (IY) and a mass dependent term (ADT). High importance factors are indicted in bright green.

The future of nuclear arms control agreements is uncertain due to numerous technological and political reasons; moreover, the U.S.'s strategic position to modernize its nuclear forces as outlined in the 2018 Nuclear Posture Review might prove to be a destabilizing factor for traditional arms control treaties [16]. This nuclear policy, however, might also be instrumental in facilitating strategic dialogue not only with Russia but with China as well, two nations that have advanced their military capabilities to act as global powers. Future arms control treaties could be in the form of trilateral agreements if the U.S.'s posture to modernize its nuclear force includes further arms reduction. This is particularly likely if the U.S. simultaneously maintains a strategic position of diversity and flexibility in the U.S. nuclear deterrent to respond effectively and proportionally to nuclear attack of any scale from potential adversaries, as well as to contribute to the assurance of its allies and partners through extended deterrence, attribution of proliferation and re-establishment of deterrence, and hedging strategies to reduce risk of strategic competition between states [16]. The work featured in this dissertation can be incorporated in future nuclear arms control agreements through supporting the safety, security, and effectiveness of the U.S. nuclear stockpile, which consequently enables U.S. policy makers to engage in dialogue from a position of strength.

One ever-strengthening component of the U.S.'s nuclear deterrent capability, however, has been the advancement of the nuclear community's technical skills towards applications such as nuclear forensics for the identification and attribution of a nuclear detonation by possible adversaries. The characterization of nuclear explosions via isotopic signatures was developed during the era of nuclear explosive testing in the mid-20th century at the Nevada Test Site when considerable data was collected from more than 100 atmospheric and 928 underground conducted nuclear tests [17]. In the years since the last U.S. nuclear test in 1992 when the U.S. placed a voluntary moratorium on underground testing and began its U.S. science-based Stockpile Stewardship Program, these extensive data sets on nuclear explosions have provided, and continue to provide, invaluable nuclear data for the development and improvement of the neutron-induced reaction databases for forensic applications.

The first Nuclear Posture Review was published in 1994, which outlined the role of the U.S. nuclear stockpile in U.S. security strategy. In the 2018 Nuclear Posture Review, the priority of U.S. "ability to maintain and certify a safe, secure, and effective nuclear arsenal" was reaffirmed [16]. Additionally, emphasis was placed on both global elimination of nuclear weapons, as well as the need to modernize the U.S. nuclear capability [16]. In order to fulfill these goals, the U.S. places particular importance on the partnership of policy and technology, which so far has seen the decrease of nuclear weapons from tens of thousands to under 5,000 in the U.S. shown in Fig. 1.3 [11]. The U.S. science-based Stockpile Stewardship Program serves to strengthen the nation's central deterrence capabilities, in order to protect its domestic security, as well as its extended deterrence capabilities, to protect the security of U.S. forces abroad and of U.S. allies. These capabilities are strengthened through ensuring the health of the U.S. Stockpile, demonstrating recurring commitment to nonproliferation and arms control efforts, preventing of unauthorized or accidental nuclear detonations and identifying and holding potential adversaries accountable for testing of nuclear devices [16].

The U.S. science-based Stockpile Stewardship Program is highly dependent on accurate

and reliable nuclear data, which affects the U.S.'s ability to certify, without the need to perform physical testing of nuclear explosives, the reliability of the U.S. nuclear arsenal. Pivotal to the science-based mission is cross section data for neutron-induced reactions on fission products, as illustrated in the reaction network near $A = 95$ mass region of Fig. 1.4 [12]. The reaction network presents several possible decays and reactions that occur during and after a fission event to a fission fragment in a nuclear explosion. To the right of the figure is a scale describing the importance of each isotope, where the importance factor (IF) is a product of the independent fission yield (IY) and a mass dependent term (ADT) that described the distance from the $A = 95$ mass chain. For instance, ^{95}Sr is given the highest importance factor as it has the highest independent yield along the $A = 95$ chain. This fission fragment β-decays to ^{95}Zr, which is measured in debris post-detonation to determine the yield of a nuclear weapon. However, as the reaction network illustrates, additional interactions other than β decay can influence the production of isotopic signatures; neutron capture on lighter Sr isotopes such as ^{92}Sr(n,γ)^{93}Sr, for instance, influences the distribution of ^{95}Zr.

This dissertation is motivated by the critical role that neutron-induced reactions on ^{92}Sr, in particular, play in a number of fundamental physics and application-driven programs, from the U.S. science-based Stockpile Stewardship mission of ensuring the safety, security, and effectiveness of the U.S. nuclear deterrent, to cosmogenic nucleosynthesis. Specifically, the work presented in this dissertation aims to experimentally constrain the statistical nuclear properties of ^{93}Sr beyond available theoretical models, and to determine using the Hauser-Feshbach formalism the neutron-capture cross section, which is serves the nuclear data needs of the U.S. science-based Stockpile Program.

1.3 Cosmogenic Nucleosynthesis

In addition to the application-driven need for comprehensive neutron-induced reaction cross section data, neutron-induced reactions play a key role in understanding the creation of elements beyond iron. Stellar nucleosynthesis began with the proton-proton chain where proton-proton fusion followed by β decay leads to production of deuterium, which also combines with a proton to form ^{3}He. The fusion of two ^{3}He leads to ^{4}He and two protons, which increases the high proton field and continues the proton-proton chain. The presence of ^{4}He in addition to carbon, nitrogen, and oxygen in stellar environments leads to the CNO cycle and eventually α-particle capture reactions to produce iron. The process of fusion is thermodynamically favored, as shown in Fig. 1.5 by binding energy per nucleon as a function of mass number A, where stability increases with binding energy per nucleon. However, beyond iron, fusion is not thermodynamically favored and the Coulomb barrier as a function of charge increases for heavy elements; thus, the heaviest elements are produced by slow neutron capture reactions, s-process, and the rapid neutron capture process, r-process which produce elements heavier than iron through repeated capture of a neutron followed by β decay back toward stability to a nucleus that may capture a neutron once more and repeat

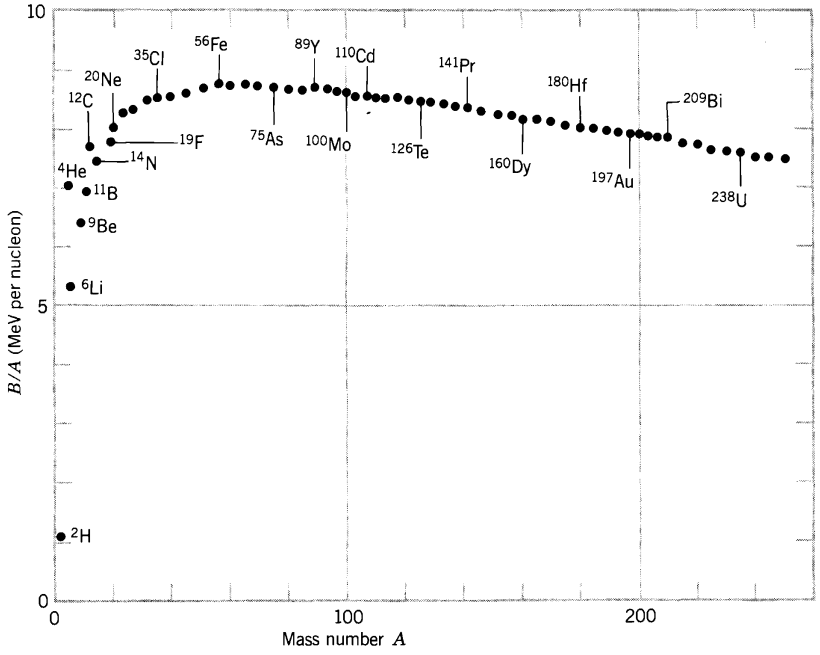


Figure 1.5: Binding energy per nucleon [18].

the process of successive β decays and neutron captures [18].

However, discrepancies between predicted and observed abundances of elements Rb, Sr, Y and Zr may be the result of an intermediate neutron-capture process known as the i-process. Changes to the surface chemical composition of the post-asymptotic giant branch (post-AGB) star Sakurai's object among other observations indicate that the i-process may be a possible solution explaining the discrepancy [19]. Denissenkov et al. used various theoretical models to calculate solar-scaled abundances of Rb, Sr, Y and Zr in Sakura's object and compare it to the observed abundances shown in Fig. 1.6. While progress was achieved in studying the impact of nuclear uncertainties on i-process predictions, reduction of uncertainties in observations, nuclear physics, or both must be achieved in order to determine if the i-process predictions are appropriate especially in the case of Sr and Zr. In particular, nuclear physics uncertainties can be reduced be using indirect techniques such as the β-Oslo Method to constrain the NLD and γSF, and consequently, the neutron-capture cross sections which nucleosynthesis calculations rely upon.

1.4 Thesis Outline

The experimental details of measuring the γ-ray spectra of ^{93}Sr and using it to determine statistical properties of ^{93}Sr via the β-Oslo Method are presented and discussed in the following chapters. Chapter 2 discusses foundational concepts of β decay, nuclear level density,

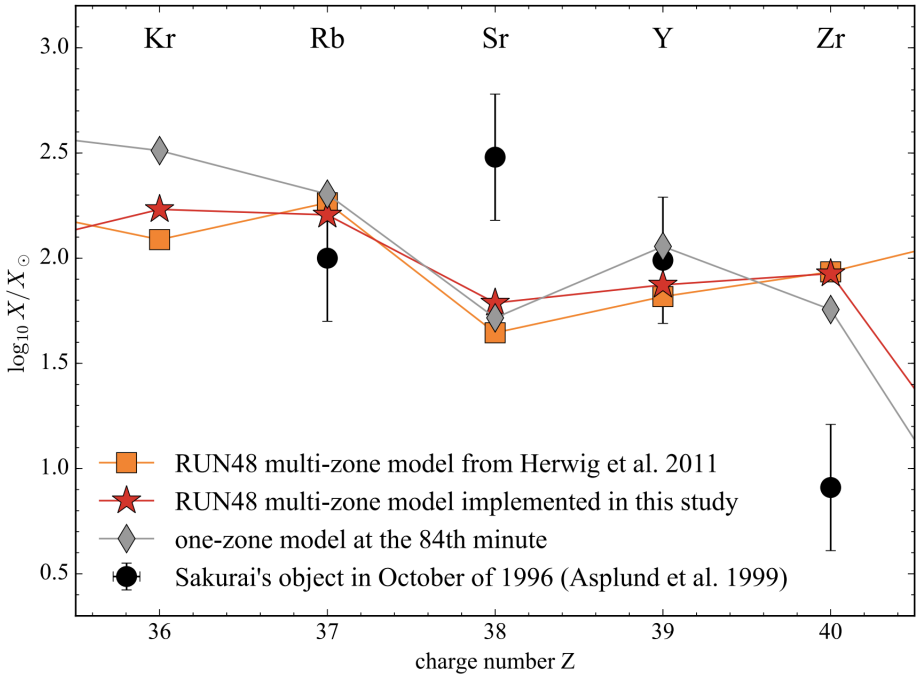


Figure 1.6: The observed (black circles with error bars) and predicted (other symbols) solar-scaled abundances of Rb, Sr, Y and Zr in Sakurai's object [19].

and the γ-ray strength function. Chapter 3 details an experiment which was performed as part of this doctoral work, utilizing a radioactive isotope beam of ^{93}Rb to produce ^{93}Sr, in order to measure emitted β-delayed γ rays of ^{93}Sr using a total absorption spectrometer (TAS) called the Summing NaI(Tl) detector (SuN). Chapter 4 discussed the four main steps of the β-Oslo Method: (i) unfolding the γ-ray spectra, (ii) extraction of the first generation γ rays, (iii) extraction of the NLD and γSF, and (iv) normalization of the NLD and γSF. Chapter 5 presents the results of the β-Oslo analysis of the data collected from the experiment described in Chapter 3 and discusses the impacts of various normalization approaches. Chapter 6 presents the determined ^{92}Sr(n,γ) cross section using the reaction code TALYS [20] and the experimentally-obtained NLD and γSF, and further discusses the propagation of systematic error through the β-Oslo Method. Conclusions to this dissertation are provided in Chapter 7.

Chapter 2

Underlying Nuclear Theory

In this chapter we will discuss the theoretical framework used to calculate neutron capture including the concept of the compound nucleus (CN); the statistical properties of highly-excited nuclear states including nuclear level density (NLD) and γ-ray strength functions (γSF) and Hauser-Feshbach (HF) reaction modeling. The concept of an intermediate nuclear state formed upon the capture of an incident particle by a target nucleus was first proposed by Niels Bohr in 1936 [21]. This intermediate state, known as a CN, is formed with a characteristic excitation energy given by the sum of the projectile kinetic energy in the center of mass frame plus the binding energy of the projectile. An important characteristic of the compound nuclear system is a long lifetime compared to the time required for the average nucleon to traversal the nuclear diameter or photon emission, which results in the formation of well-defined nuclear structures. The Fermi gas model, a thermodynamic picture of the nucleus, describes the total excitation energy as shared by a large number of nucleons through numerous collisions until a thermal equilibrium is reached, where individual nucleons in the compound system do not have sufficient energy, on average, to be re-emitted. However, other de-excitation pathways become more probable, such as γ decay which is a relatively slow nuclear process compared to the time required for nucleons to move about the nucleus [7]. Thermal equilibrium inside of a CN, and hence the long lifetime, leads to an important feature: the decay mode of the CN will be completely independent of the means by which it is formed.

The nuclear absorption of the incident particle results in an increase in total excitation energy of the CN, as compared to the initial energy of target nucleus, as well as an increase of possible nucleon configurations. The possible configurations, Ω, and thus entropy, $S = k_B \ln(\Omega)$, of the CN is directly related to the average energy per particle in a CN. Bethe proposed that the difficulty in calculating the NLD can be simplified by calculating the entropy of a Fermi gas, where the NLD is related to entropy as $\rho \propto \Omega$. The temperature T of the nucleus as it relates to the excitation energy E is given as $T = \sqrt{E/a}$, where a is a parameter representing nuclear level spacing [22]. From the second Law of Thermodynamics, $TdS \geq dE$, the entropy of the compound system is related to the nuclear temperature such that the derivation leads to the simple expression of $S = 2aT$. The temperature can then be

expressed in terms of possible nucleon configuration, or the NLD, as $2aT \propto \ln(\rho)$ which is Bethe's first description of the NLD as a function of the excitation energy: $\rho(E) \propto e^{2\sqrt{aE}}$. A more in-depth discussion of the NLD, considering various phenomenological models as well as microscopic calculation of the NLD, will be presented in Section 2.2.

The CN has several channels by which it can de-excite into a more stable configuration. The probability of exiting through a particular channel is given by the ratio of the width for that particular channel to the total width, which is the sum of widths of all possible channels. This two-step process, consisting of an entrance and an exit channel, is known as the Bohr hypothesis [21], where the width is directly related to the transmission probability and the level spacing. The transmission probability can be compared to the transition rate λ from an initial state $|i\rangle$ to a final state $|f\rangle$ as described by Fermi's golden rule [7]:

$$\lambda = \frac{2\pi}{\hbar}|\langle f|H_{int}|i\rangle|^2\rho(E_f), \tag{2.1}$$

where H_{int} is the transition operator and $\rho(E_f)$ is the density of final states at energy E_f. Numerous initial and final states each with a particular set of decay properties are possible within each excitation-energy bin, and thus average quantities can describe statistical processes at high excitation energies.

For instance, a neutron hitting a neutron-rich nucleus at high excitation energies near or below the particle emission threshold forms a CN which subsequently statistically decays to levels below and the ground state by emitting γ rays. While the NLD describes the distribution of levels in the CN, the partial radiative widths describe the probability of a transition from an initial excitation energy E_i to levels at an energy E_f by emitting a γ ray of energy E_γ. The total γ width of a state is the sum of partial widths, which vary in transition type and γ-ray energy. At high excitations energies, i.e., energies near the neutron separation energy, transitions are generally dipole transitions. Section 2.3 will discuss γ decay of a CN, as well as phenomenological models describing the γ-decay strength, i.e., the γSF.

Calculating the neutron capture cross section is therefore dependent on determining energy-averaged radiative widths and the NLD, as well as the probability that a neutron will enter the target nucleus and form the CN, as described by the neutron optical model. Phenomenological nuclear level density models which are parameterized with experimental data, as well as microscopic models of the NLD, are discussed in Section 2.2. In addition to the NLD, common models for the γSF and the optical model potential (OMP) will also be discussed in Sections 2.3 and 2.4. In particular, this dissertation focuses on the formation of the ^{93}Sr CN by β decay of ^{93}Rb, rather than by a neutron-capture reaction, utilizing the experimental setup presented in Chapter 3. Before statistical nuclear properties can be discussed, however, it is important to understand the β-decay mechanism that is responsible for populating highly excited states in ^{93}Sr.

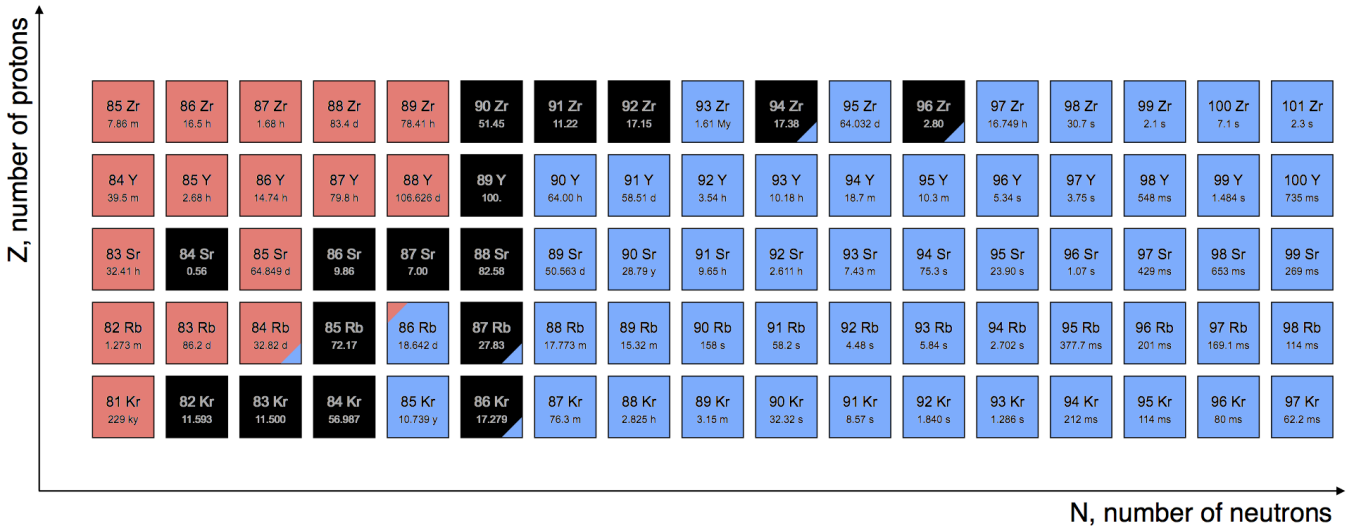


Figure 2.1: Chart of the Nuclides. The portion of the nuclide chart shown includes stable nuclides (black), β^- decay unstable nuclides (blue), and β^+/EC decay unstable nuclides (pink) for Kr, Rb, Sr, Y, and Zr isotopes [23].

2.1 β Decay

The β-decay process is a mechanism, governed by the weak nuclear force, whereby an unstable nuclide approaches a more stable nuclear configuration through an optimal charge ratio. The β decay of a parent nuclide results in an isobar daughter with a greater binding energy. Binding energy is increased through β decay by three effects: increasing the symmetry between the number of protons Z and the number of neutrons N (i.e., Z=N), decreasing the Coulomb energy, and increasing the pairing energy. The three β decay modes are:

- β^- decay: ${}^A_Z X_N \rightarrow {}^A_{Z+1} Y_{N-1} + e^- + \bar{\nu}_e$
- β^+ decay: ${}^A_Z X_N \rightarrow {}^A_{Z-1} X_{N+1} + e^+ + \nu_e$
- electron capture (EC): ${}^A_Z X_N + e^- \rightarrow {}^A_{Z-1} X_{N+1} + \nu_e$

where a nucleon in the parent nucleus ${}^{\mathrm{A}}_{\mathrm{Z}}\mathrm{X}_{\mathrm{N}}$ undergoes decay with the creation of a lepton pair, such as an electron e^- and an electron antineutrino $\bar{\nu}_e$ or a positron e^+ and an electron neutrino ν_e. Each decay mode adheres to laws of the conservation of energy, momentum, nucleon number, and leptons. However, C. S. Wu *et al.* proved, when studying ^{60}Co, that parity is not conserved in β decay [24].

2.1.1 Kinematics of β Decay

For neutron-deficient nuclides, the N/Z ratio can be increased through electron capture and β^+ decay. β^+ decay from the ground state of the parent nucleus to the ground state of the daughter nucleus can be expressed using the following mass-energy relationship [7]:

$$\mathrm{N(Z,A)} = \mathrm{N(Z\text{-}1,A)} + \mathrm{m}_{e^+} + \mathrm{m}_\nu + \mathrm{Q}_{\beta^+}/c^2, \tag{2.2}$$

where N(Z,A) and N(Z-1,A) are the nuclear rest mass of the (Z,A) and (Z-1,A) nuclei and Q_{β^+} is the Q value for the transformation. As the neutrino mass is less than 2 eV/c^2 [18], negligibly small compared to the mass of the electron and positron $\mathrm{m}_e = 0.511\mathrm{MeV}/c^2$, the Q value can then be written in terms of atomic rest mass (the nuclear masses are converted to atomic masses by $\mathrm{N(Z,A)} + \mathrm{Zm}_e = \mathrm{M(Z,A)} + \sum_{i=1}^{\mathrm{Z}}(\mathrm{b.e.})_{\mathrm{Z},i}/c^2$, where $(\mathrm{b.e.})_{\mathrm{Z},i}$ represents the binding energy of the ith atomic electron) as

$$\mathrm{Q}_{\beta^+} = [\mathrm{M(Z,A)} - \mathrm{M(Z\text{-}1,\ A)} - 2\mathrm{m}_e]c^2. \tag{2.3}$$

The β^+ decay mode is only energetically possible if a specific threshold condition is satisfied that the mass difference between the initial and final states is $> 2\mathrm{m}_e c^2$. In addition, the nuclear recoil of the daughter nucleus is very small and can be neglected, so the Q value can be written in terms of kinetic energy:

$$\mathrm{Q}_{\beta^+} = T_{e^+} + T_\nu. \tag{2.4}$$

As a three-body problem where the nucleus recoil kinetic energy is neglected, the kinetic energy of the positron is at a maximum when the kinetic energy of the neutrino is at a minimum, and vice versa: $T_{e^+,\mathrm{max}} = T_{\nu,\mathrm{max}} = \mathrm{Q}_{\beta^+}$. This implies that the emitted positron is characterized by a continuous energy distribution from zero to Q_{β^+}.

Additionally, the N/Z ratio can also be increased by electron capture (EC) decay, whereby an atomic electron is captured by a nucleus and a proton in the nucleus is converted into a neutron, which results in a simultaneously emitted neutrino. Furthermore, the electron vacancy in the daughter nuclide is filled with an electron that transitions from a higher atomic shell by the emission of one or several characteristic X rays. The Q value for the EC decay can be written as

$$\mathrm{Q}_{EC} = [\mathrm{M(Z,A)} - \mathrm{M(Z\text{-}1,\ A)}]c^2 - B_n, \tag{2.5}$$

where B_n is the binding energy of the captured n-shell electron (n = K, L, ...). Similar to β^+ decay, EC decay is energetically possible if the threshold condition is satisfied that the mass difference between the initial and final states is greater than the n-shell electron binding energy.

Finally, β^- decay is the most relevant to this dissertation as it is the most prevalent decay mode of ^{93}Rb and is the optimal decay mode for decreasing the N/Z ratio for proton-deficient nuclei. The rate of production and destruction of radionuclides play a key role in

cosmogenic nucleosynthesis; thermal reactor design, maintenance, and safety; and supporting the science-based U.S. Stockpile Stewardship mission. The Q value of β^- decay using atomic masses is given by Eq. 2.6:

$$\mathrm{Q}_{\beta^-} = [\mathrm{M(Z,A)} - \mathrm{M(Z{+}1,\ A)}]c^2, \tag{2.6}$$

while the Q value in terms of kinetic energy is given by Eq. 2.7:

$$\mathrm{Q}_{\beta^-} = T_{e^+} + T_{\bar{\nu}}. \tag{2.7}$$

As is the case with both β^+ and EC decay, the proton recoil kinetic energy, T_p, and the antineutrino mass, $\mathrm{m}_{\bar{\nu}}$, are neglected. The implicit result is that the maximum electron kinetic energy is equal to Q_{β^-}, and consequently, $T_{\bar{\nu}} = 0$. Once again, the energy distribution of the electron is continuous from zero to Q_{β^-}.

The mass-energy relationship discussed for all three modes of β decay is between the ground states of the parent and daughter nuclei; however, β decay is possible between excited states of both nuclei, as well. The Q value for the β decay from an initial excited state in the parent nucleus to an excited state in the daughter nucleus is determined from the Q value for the ground state to ground state transition Q_{ground} plus the excitation energy difference, which can be expressed as

$$\mathrm{Q}_{ex} = \mathrm{Q}_{\mathrm{ground}} + E_{x,p} - E_{x,d}, \tag{2.8}$$

where $E_{x,p}$ is the energy of the level in the parent and $E_{x,d}$ is the energy of the level in the daughter. In cases where β decay populates an excited state in the daughter, a nucleon may be emitted from the resulting nucleus if the Q value is greater than the nucleon separation energy. However, in the case that the Q value is less than the nucleon separation energy, γ rays are emitted to decrease the excitation energy of nucleus until a more stable nuclear configuration is achieved, i.e., an isomeric state or the ground state is reached by γ decay. As the β-decay Q value of ^{93}Rb is greater than the neutron separation energy of ^{93}Sr, both β-delayed neutron and γ emission are possible and will be discussed in the following sections.

2.1.2 Classification of β Decays

The β decay of a parent nucleus to the ground state or an excited state of the daughter nucleus can be classified as either *allowed* or *forbidden* to describe the probability of decay from an initial state ψ_i to a final state ψ_f. Decays classified as forbidden do occur, but with a smaller probability than those classified as allowed. The classification of β decay is determined by the change in parity $\Delta\pi$ and the change in total angular momentum ΔJ, adhering to conservation of momentum, and can be express as

$$\Delta J = J_p - J_d = J_e + J_{\bar{\nu}}, \tag{2.9}$$

where J_p is the total angular momentum of the parent, J_d is the total angular momentum of the daughter, J_e is the total angular momentum of the electron and $J_{\bar{\nu}}$ is the total angular

momentum of the antineutrino (for β^- decay). The classification as an allowed transition is an approximation describing the similarity between the initial state wavefunction and final state wavefunction, i.e., if the states are very similar, the decay probability is large. In the following section, the Fermi Theory of β decay will be discussed, as it relates the probability of a transition to the properties of the perturbation potential (the potential of the weak nuclear force) and the initial and final states of the system. Table 2.1 lists the classification of β-decay transitions between ψ_i and ψ_f. The label assigned to each β-decay transition described by the change in total angular momentum and parity are each listed in Table 2.1. In addition, the last column of Table 2.1 gives the $\log_{10} ft$ value of the transition, which is related to the β-decay probability discussed in the next section.

Table 2.1: Classification of β-decay transitions. The first two columns list the change in total angular momentum and parity between the initial and final states of the β-decay transition. The third column lists the label assigned to the transition. In the final column, lower limits of the experimentally determined $\log_{10} ft$ value are listed [7].

ΔJ	$\Delta\pi$	Name	Range of $\log_{10} ft$
$0^+ \rightarrow 0^+$	no	superallowed	$\approx$3.5
0,1	no	allowed	$\geq 2.9 - 6.5$
0,1,2	yes	first-forbidden	$\geq 6.5 - 8.5$
2,3	no	second-forbidden	$\geq 11.0 - 12.8$
3,4	yes	third-forbidden	$\geq 14 - 20$
4,5	no	fourth-forbidden	≈ 20

2.1.3 Fermi Theory of β Decay

In this section, the Fermi Golden Rule #2 as it relates to β^- decay will be discussed. The decay probability, w, from an initial state ψ_i^o to a final state ψ_f^o is given by Fermi Golden Rule #2,

$$\mathrm{w} = \frac{2\pi}{\hbar} \left| \left\langle \psi_f^o \right| \mathrm{H}' \left| \psi_i^o \right\rangle \right|^2 \rho(\mathrm{E}_f), \tag{2.10}$$

where $\rho(\mathrm{E}_f)$ is the density of final states, i.e., the number of final states per unit energy at E_f. In the case of β^- decay, the initial and final states are the time-dependent wavefunctions, ψ_i^o and $\psi_{f,total}^o$, respectively. The wavefunction $\psi_{f,total}^o$ is the sum of time-dependent wavefunctions of the final state of the daughter nucleus, the emitted electron and the antineutrino. Consequently, the perturbed potential H_β due to the weak nuclear force acting on ψ_i^o can be expressed in terms of the final products:

$$\left\langle \psi_{f,total}^o \right| \mathrm{H}_\beta \left| \psi_i^o \right\rangle = \int \psi_{f,total}^o{}^* \mathrm{H}_\beta \psi_i^o \mathrm{d}\tau = \int \psi_f^o{}^* \psi_e{}^* \psi_{\bar{\nu}}{}^* \mathrm{H}_\beta \psi_i^o \mathrm{d}\tau, \tag{2.11}$$

where ${\psi^o_{f,total}}^*$ denotes the complex conjugate of $\psi^o_{f,total}$. The matrix element $M_{f,i} = \left\langle \psi^o_{f,total} \right| \mathrm{H}_\beta \left| \psi^o_i \right\rangle$ is given by the integral over all of the variables contained in the wavefunctions and encapsulated as $\mathrm{d}\tau$.

The wavefunctions of the leptons are approximated relative to the dimensions of the nucleus. The wavefunction of the antineutrino, $\psi_{\bar{\nu}}$, is described as a plane wave normalized to the volume of the nucleus, V. The following assumptions can be used to further simplify the expression:

- the mass of the antineutrino is negligible compared to the Q value,
- the wavelength of the antineutrino is significantly larger than the nuclear radius r_n,
- consequently, the wavefunction is constant within the nucleus, i.e., $\psi_{\bar{\nu}}.(r = r_n) = \psi_{\bar{\nu}}(r = 0)$

Thus, $\psi_{\bar{\nu}}$ can be approximated as

$$\psi_{\bar{\nu}} = \frac{1}{V^{1/2}}. \tag{2.12}$$

Similar assumptions can be taken into account regarding the wavefunction of the electron, ψ_e. However, as the electron has charge and interacts with the Coulomb field of the protons, the plane wave approximation of the wavefunction is distorted as a function of Z protons and the electron energy, E_e. Fermi introduced a function known as the Fermi function, $\mathrm{F(Z, E}_e)$, to approximate the distortion independent from the wavefunction; the distorted wavefunction of the electron at the origin of the nucleus is given by

$${\psi_e}^*(0) = \frac{\mathrm{F(Z, E}_e)^{1/2}}{V^{1/2}}. \tag{2.13}$$

With these approximations of the lepton wavefunctions, Eq. 2.10 in the case of β-decay transitions becomes

$$\mathrm{w} = \frac{2\pi}{\hbar}\frac{1}{V^2}\mathrm{F(Z, E}_e) \left| \int {\psi^o_f}^* \mathrm{H}_\beta \psi^o_i \mathrm{d}\tau \right|^2 \rho(\mathrm{E}), \tag{2.14}$$

where H_β is a potential, g, with a constant magnitude and local range as well as an operator, Q_n, transforming a neutron into a proton and creating a lepton pair. The remaining term on the right-hand side of Eq. 2.14, ρ(E), represents the number of possible transitions to a final state. The derivation of the density of final states ρ(E) is complex and is presented in the Appendix A, while the expression is simply stated here:

$$\rho(\mathrm{E}_o = \mathrm{E}_e + \mathrm{E}_{\bar{\nu}}) = \frac{16\pi^2 V^2}{(2\pi\hbar)^6 c^3}(\mathrm{E}_o - \mathrm{E}_e)^2 \mathrm{p}_e^2 d\mathrm{p}_e, \tag{2.15}$$

where p_e is the momentum of the electron. Finally, if w in Eq. 2.10 represents the differential total decay constant $\mathrm{d}\lambda$ with respect to the momentum of the electron, then the final

expression for the total decay constant, or decay probability, is given as

$$\lambda = \left| \int \psi_{o,f}{}^{*} Q_n \psi_{o,i} \mathrm{d}\tau \right|^2 \frac{32\pi^3}{\hbar(2\pi\hbar)^6 c^3} g^2 \int_{\mathrm{E}_e=0}^{\mathrm{E}_o} \mathrm{F(Z,E}_e)(\mathrm{E}_o - \mathrm{E}_e)^2 \mathrm{p}_e^2 d\mathrm{p}_e. \tag{2.16}$$

In Eq. 2.16, the matrix element $M_{f,i} = \int \psi_{o,f}{}^{*} Q_n \psi_{o,i} \mathrm{d}\tau$ is the component that describes the similarity between the initial and final state wavefunctions. The remainder of Eq. 2.16 can be described by two main components: a Coulomb interaction factor, $\mathrm{F(Z,E}_e)$, and a statistical factor that characterizes the lepton, $(\mathrm{E}_o - \mathrm{E}_e)^2 \mathrm{p}_e^2$.

The decay constant as expressed by Eq. 2.16 provides insight into both the distribution of electrons and the half-life of the β-decay transition ($t_{1/2} = \ln(2)/\lambda$). The β spectrum can be approximated as the product of the Fermi function and the statistical factor. For instance, the hypothetical β spectrum of a Z =37 nucleus shown in Fig. 2.2 is a softened spectrum due to the Fermi function that represents presence of a Coulomb field. In addition, the half-life is approximated as inversely dependent on matrix element $M_{f,i}$, a product of physical constants $\Gamma = g^2 m_e^2 c^4/(2\pi^3\hbar^7)$, and the Fermi function in terms of the total energy of the electron in units of electron rest mass W, and thus expressed as

$$t_{1/2} = \frac{\ln(2)}{\Gamma \left| M_{f,i} \right|^2 f(Z, W_o)}. \tag{2.17}$$

The $f(Z, W_o)$ term is the integral of the Fermi function from $W = 1$ to the total decay energy W_o. As the half-life ranges widely, the half-time is referenced as $\log_{10}(f(Z, W_o)t_{1/2})$, or simply as $\log_{10}(ft_{1/2})$. For instance, the ground state to ground state β decay of ^{93}Rb is a first-forbidden transition with a $\log_{10}(f(Z, W_o)t_{1/2})$ value of 6.14; however, this transition has the greatest β-decay intensity compared to known ^{93}Sr excited states. Values of $\log_{10}(ft_{1/2})$, such as those listed in Table 2.1, are experimental measurements of the β-decay classification as allowed or forbidden transitions. In the case of the β decay experiment analyzed in this dissertation, generally, the β decay from the ground state of ^{93}Rb to excited states of ^{93}Sr consists of allowed transitions, first-forbidden transitions, and occasionally second-forbidden transitions according to ΔJ and $\Delta\pi$ selection rules and the corresponding $\log_{10}(ft_{1/2}) = 5.0$ to 9.0. However, the spin-parity assignments of ^{93}Sr energy levels are all tentative assignments other than the $5/2^+$ assignment of the ground state, and thus, classification of β-decay transitions are uncertain. The β-decay feeding intensity of the existing decay scheme of ^{93}Rb, as well as the decay of ^{93}Sr, from the National Nuclear Data Center (NNDC) is shown as function of excitation energy in Fig. 2.3. The β-decay daughter ^{93}Sr is populated predominantly at the ground states and excited states near 3.80 and 4.00 MeV, while the β-decay daughter ^{93}Y is populated at excited states near 1.60, 2.60, and 2.80 MeV. The analysis of ^{93}Sr in this dissertation is limited to excitation energies above 3.00 MeV to avoid interference from the β-decay of ^{93}Sr.

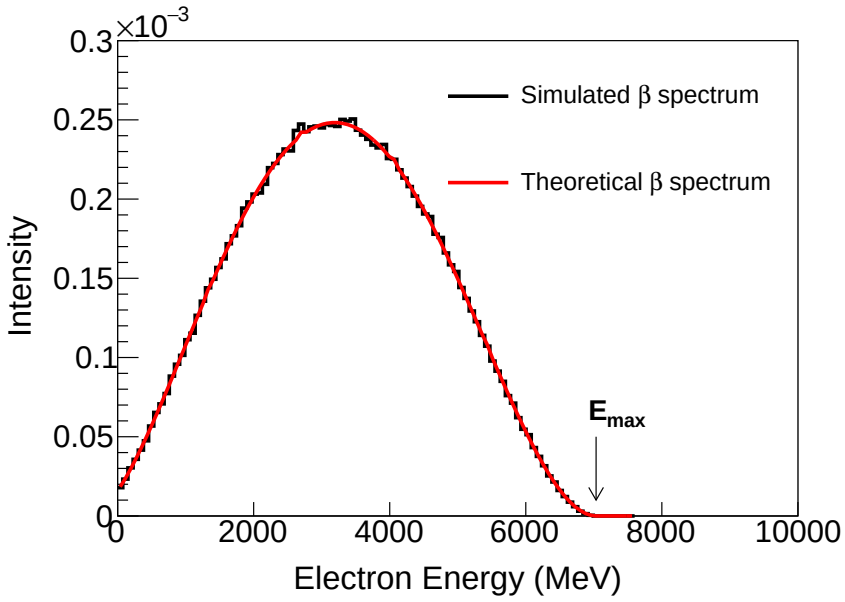


Figure 2.2: Simulated β-decay spectrum (black) for decay of ^{93}Rb ground state to second excited state of ^{93}Sr compared to theoretical spectrum [7, 25]. The maximum kinetic energy of the electron is Q-$E_{2^{nd}ex}$=7.03 MeV. The area beneath the spectrum is unity.

2.1.4 Angular Momentum Distributions

The lepton pair created at the decay site of the nucleon is emitted with either parallel or anti-parallel spins. A transition which occurs with a lepton pair with anti-parallel spins, i.e., $S = s_e + s_\nu = 0$, is known as a Fermi Transition. Whereas, if a transition occurs with a lepton pair with parallel spins, the leptons carry away a single unit of angular momentum $S = 1$ and the transition is referred to as a Gamow-Teller Transition. The classification of β-decay transitions listed in Table 2.1 can be further classified as either Fermi or Gamow-Teller Transitions.

2.1.5 β-delayed Neutron Emission

β-delayed neutron emission is an important process in the fission chain reaction of nuclear power reactors. In nuclear-powered thermal reactors, fissile material undergoes fission after capturing thermal neutrons. The A+1 nucleus then scissions, creating two primary fragments, which emit prompt neutrons and γ rays. Scission occurs asymmetrically at thermal (0.025 eV), resonance (10 - 300 eV), and intermediate (300 eV - 1 MeV) energies, generating a light-mass fragment around A=95 and a heavy-mass fragment around A=140. As shown for the case of ^{235}U(n, f) in Fig. 2.4, the mass distribution becomes more symmetric with increasing incident neutron energy. The fragments are then referred to as secondary fragments

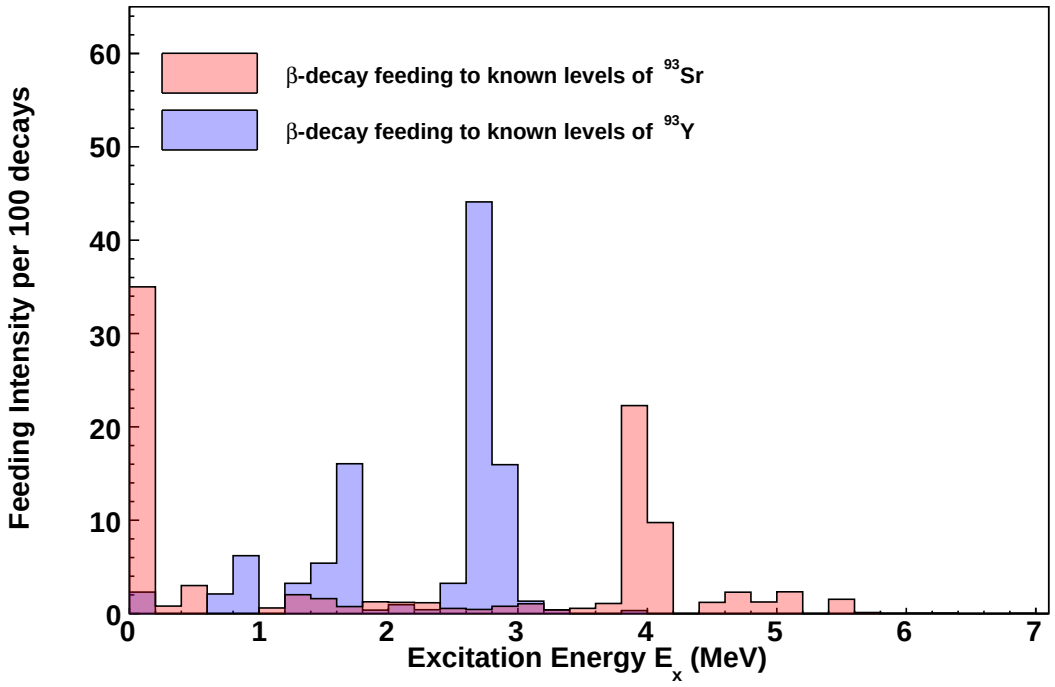


Figure 2.3: β-decay feeding intensities of ^{93}Rb and ^{93}Sr from the Evaluated Nuclear Structure Data File (ENSDF) [25].

that are still in an excited state. To reach a stable nuclear configuration of lower energy, the secondary fragments decay by β-particle emission. In relevance to the work in this dissertation, ^{93}Sr is a fission fragment with a relevantly large independent yield of 2.57(5)%, which is approximately half that of ^{95}Sr, the isotope in the A=95 chain with the highest independent yield [26]. Understanding the production and destruction of fission fragments is of great interest to basic nuclear physics and the science-based U.S. stockpile stewardship mission. In addition, β-delayed neutron emission plays an important role in r-process nucleosynthesis.

While ^{93}Rb undergoes β^- decay, the β-delayed neutron branching ratio is only 1.39 (7)%. The Q_{β^-} value of ^{93}Rb is 7.466 (9) MeV while the neutron separation energy, S_n, of ^{93}Sr is 5.290 (8) MeV; as a result, the β-decay from ^{93}Rb to ^{93}Sr can populate excitation energies above S_n, whereby particle-unbound levels will decay by neutron emission to levels in the neutron decay daughter ^{92}Sr. The first excited state in ^{92}Sr is 814.7 keV, and thus the analysis of ^{93}Sr in this dissertation is limited to an upper excitation energy of < 6.10 MeV. However, an upper threshold is placed on the γ-ray energy of 1.5 MeV, and thus excitation energies above S_n can be analyzed without interference from γ rays emitted from the ^{92}Sr nucleus.

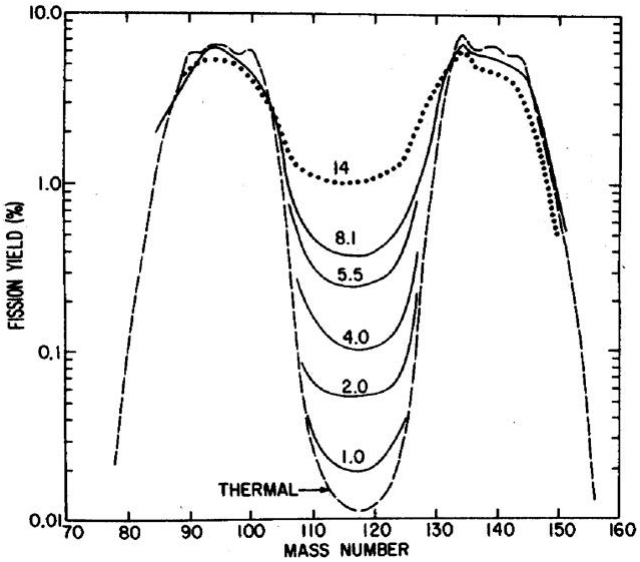


Figure 2.4: Mass distribution of ^{235}U$(n,\ f)$ where incident neutron energies range from thermal (0.025 eV) to high energy (14 MeV) [27].

2.1.6 β-delayed γ Emission

Decay by γ emission is mediated by the electromagnetic force, and thus transitions from excited states initially populated by β decay to lower excitation energies, as well as to the ground state, emit γ rays characterized as electric or magnetic type ($X = E$ or M) and multipole L. γ emission will be discussed in further detail later in Section 2.3 as it relates to the γSF. β-delayed γ emission is relevant to this dissertation as an experiment was performed to analyze the γ rays emitted by ^{93}Sr, the β decay daughter of ^{93}Rb. The β decay of ^{93}Rb primarily populates the ground state of ^{93}Sr; however a considerable percent of β decays populate states between 3.8 and 4.0 MeV as reported by nuclear data libraries shown in Fig. 2.3 and confirmed by the experimental data presented in this dissertation shown by the measured TAS of ^{93}Sr in Fig. 3.17 of Chapter 5. Analysis of the experimental data is discussed in Chapter 5.

An alternative decay mode that competes with γ emission is internal conversion (IC), which is favored when the change in angular momentum is $\Delta J = 0$, e.g, an initial 0^+ excited state decays to a final 0^+ state. Internal conversion is also enhanced when the difference between initial and final states is small, the change in angular momentum is large, and the Z of the nucleus is large. The theory of photon emission and internal conversion as well as the corresponding matrix elements are discussed in the Appendix A. Briefly, internal conversion is a process of direct energy transfer from the nucleus to atomic electrons, i.e., an atomic orbital electron is ejected. The process is energetically possible when the threshold condition is satisfied such that the transition energy is greater than the binding energy of the n-shell

electron to be ejected. A vacancy remains following internal conversion, and as a result this process is followed by X-ray or auger electron emission. The half-life of an excited level is determined by the combined decay probability of both internal conversion and γ emission, and thus, the total decay probability λ_{total} is the sum of the γ decay constant and the internal conversion decay constant:

$$\lambda_{total} = \lambda_{\gamma} + \lambda_{IC}. \tag{2.18}$$

While internal conversion always competes with γ emission, the contribution of internal conversion to the decay probability of an excited state is usually small. For instance, in the case of ^{93}Sr, the ratio of internal conversion to γ emission, $\alpha = \lambda_{IC}/\lambda_{\gamma}$, is only reported for the first two excited states at 213.431 keV and 432.604 keV, and the α values are relatively small compared to heavier nuclei such as ^{243}Pu which is produced by neutron capture and has nine excited states below 500 keV with α values two orders of magnitude larger.

2.2 The Nuclear Level Density

One of the first theoretical descriptions of the NLD was, put forth by H. Bethe [22]. This picture of the nucleus only considers the potential acting on each particle to calculate the NLD $\rho(E, J, \pi)$, i.e., the number of levels within an energy bin around an excitation energy, E, for a certain spin, J, and parity, π. However, the details of the wavefunction of each nuclear level cannot be extracted using this phenomenological description. The total level density at an excitation energy E includes degenerate states for each level:

$$\rho(E) = \frac{\sqrt{\pi}}{12} \frac{e^{2\sqrt{aU}}}{a^{1/4}U^{5/4}}, \tag{2.19}$$

with effective energy U defined by

$$U = E - \Delta, \tag{2.20}$$

where the empirical parameter Δ accounts for the energy shift equal to the pairing energy. The level density parameter, a, also represents the idea of the nucleus as a volume confining free neutrons and protons. Ericson further expanded upon Bethe's initial description, deriving a spin, J, and parity, π, dependent NLD for high excitation energies and heavy nuclei [28, 29]. The theoretical model is known as the Fermi Gas (FG) model of the NLD, where the observable level density is expressed as

$$\rho_{FG}(E) = \sum_{J}\sum_{\pi} \rho(E, J, \pi) = \sum_{J}\sum_{\pi} g(E, J)P(\pi)\rho(E) = \frac{\sqrt{\pi}}{12} \frac{e^{2\sqrt{aU}}}{a^{1/4}U^{5/4}} \frac{1}{\sqrt{2\pi}\sigma}. \tag{2.21}$$

The spin-cutoff parameter, σ^2, represents the angular momentum distribution of the level density. The level density $\rho(E, J, \pi)$ can be factorized as a function of spin distribution $g(E, J)$ and parity distribution $P(\pi)$. The spin distribution is given by

$$g(E, J) = \frac{2J + 1}{2\sigma^2} e^{\left[\frac{-(J+1/2)^2}{2\sigma^2}\right]}, \tag{2.22}$$

for states around excitation energy, E, with spin, J. Ericson first observed an energy shift in NLD curves of even and odd isotopes: ^{55}Fe, ^{57w}Fe, and ^{58}Fe, which was approximately equal to the pairing energy of these nuclei [28]. From an investigation of the systematics of nuclear level density parameters for 310 nuclei, Egidy and Bucurescu developed several empirical formulations of σ^2 [30, 31, 32].

While the Fermi gas model best describes the NLD at high excitation energies, experimental data is best fit by a nuclear temperature-dependent model at low excitation energies [33]. Several NLD models will be discussed in the following sections. The first two models to be introduced, the Constant Temperature (CT) and the Back-shifted Fermi gas (BSFG) models, do not take into consideration a few important aspects of nuclear interactions such as pairing and shell effects or collective effects. A challenge which often occurs when using phenomenological models is the completeness of the formalism and parameterization [34]. Egidy and Bucurescu [30, 31, 32] provide the most complete determination of level density parameters for 310 nuclei between ^{18}F and ^{251}Cf and have developed relatively-simple formulas for the extrapolation to nuclei far from stability.

2.2.1 Constant Temperature Model

At low excitation energies (up to approximately 10 MeV) a constant nuclear temperature dependence model best fits experimental data from the previous work of A. Gilbert and A. G. W. Cameron [33]. The cumulated number of experimental levels $N(E)$ with energies up to E (and below 10 MeV) can be fit using the formula:

$$N(E) = e^{(\frac{E-E_0}{T})}, \tag{2.23}$$

whereby the derivative of $N(E)$ with respect to a change in excitation energy is the total level density $\rho(E)$ given by Eq. 2.24,

$$\rho(E) = \frac{1}{T} e^{(\frac{E-E_0}{T})}, \tag{2.24}$$

where the nuclear temperature, T, and energy shift, E_0, are free parameters used to fit experimental data. The published compilations of systematics of nuclear level density parameters by Egidy and Bucurescu describes simple empirical formulas for E_0 and T developed by fitting low-excitation-energy levels and neutron resonance spacings at the neutron separation energy [30, 31, 32]. In previous experiments utilizing standard as well as β-Oslo Method analytical methods, the CT model has been used to successfully describe nuclei in the surrounding mass region of ^{93}Sr, e.g., the neutron-capture cross section of ^{76}Ge obtained using the β-Oslo Method was found to be in agreement with recent experimental data measured using the Nuclear Resonance Fluorescence (NRF) technique [10, 35].

2.2.2 The Back-Shifted Fermi Gas Model

A modified form of the FG model is the BSFG model, as shown in Eq. 2.21 [30, 31]. This phenomenological model describes the total level density as a function of excitation energy,

E, given by Eq. 2.25,

$$\rho(E) = \frac{e^{2\sqrt{a(E-E_1)}}}{12\sqrt{2}\sigma a^{1/4}(E-E_1)^{5/4}}, \tag{2.25}$$

with the back-shift energy, E_1, and level density parameter, a, defined as free parameters that serve to adjust the model to fit experimental discrete levels. The level density parameters a and E_1 are tabulated for the nuclei studied by Egidy and Bucurescu [30, 31, 32] as well as formalized using fitted parameters representing regional systematics. Prior experiments performed for a set of 310 nuclei from Reference [30] demonstrated that E_1 correlates strongly with pairing, and thus E_1 is parameterized as a function of a pairing correction term. Also, from the work of Reference [30], a showed an almost linear dependence on the mass A. The remaining parameter σ is often formalized using one of two main forms, one being energy independent and another being energy dependent. The BSFG model with an energy dependent spin-cutoff parameter will be henceforth referred to in this dissertation as the *BSFG-ED model*. These two models, as well as the CT model, are visualized alongside the reported discrete levels of ^{93}Sr [25] in Fig. 2.5. The plot of model NLD includes various parameterizations of the nuclear temperature, T, and the spin-cutoff parameter, σ, taken from References [30, 31, 32].

2.2.3 Additional Phenomenological Models

The additional phenomenological models presented here are referenced from the user manual of the nuclear reaction code known as TALYS1.9 [20]. TALYS uses different NLD models to determine energy levels above discrete states through a continuum approximation. Similarly to the CT and BSFG models, the Generalized Superfluid Model (GSM) does not consider nuclear collective effects, but implicitly incorporates effects through semi-empirical parameters. In contrast, a collective enhancement factor is introduced in the Collective Enhancement Model (CEM) to explicitly account for collective effects, and thus assess transitions from single-particle to collective excitation.

The Generalized Superfluid Model

Similar to the CT model, the GSM is effective in describing the NLD below a critical excitation energy, above which the Fermi Gas Model is more suitable. The GSM incorporates pairing effects according to the Bardeen-Cooper-Schrieffer (BCS) theory of superconductivity [37]. At low energy up to a critical energy, U_c, and temperature, T_c, the NLD is expressed in terms of entropy, S, and a parameter, D:

$$\rho_{GSM}(E_x) = \frac{1}{\sqrt{2\pi}\sigma}\frac{e^S}{\sqrt{D}}, \tag{2.26}$$

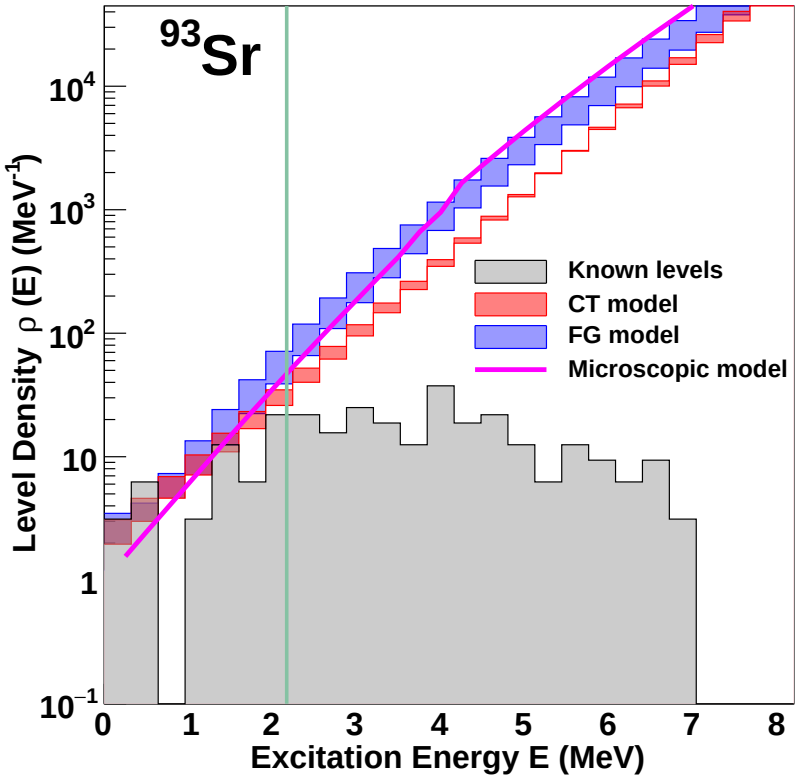


Figure 2.5: The number of known discrete levels of ^{93}Sr per 320 keV wide bins plotted as a function of excitation energy [25]. Also shown is the nuclear level density according to phenomenological models: CT model, FG model, and the tabulated nuclear level density of the microscopic model, Hartree-Fock-BCS, from the nuclear reaction code TALYS. The CT model (red band) represents variation in the parameterization of the nuclear temperature as studied by Egidy and Bucurescu [30, 31, 32]. Similarly, the FG model (blue band) represents variation in the parameterization of the spin-cutoff parameter taken from References [30, 31, 32]. The vertical solid line at 2.1686 MeV represents the number of levels forming a complete level scheme taken from RIPL-3 [36].

where, once again, σ is the spin-cutoff parameter. The variables in Eq. 2.26 are defined at the critical energy as

$$S_c = 2a_c T_c. \tag{2.27}$$

$$D_c = \frac{144}{\pi} a_c^3 T_c^5. \tag{2.28}$$

As before, a_c is the level density parameter at the critical energy U_c. At $U' \geq U_c$, the Fermi Gas Model applies with an energy shift Δ_{GSM} related to the pairing energy Δ_0, which in turns defines the threshold of breaking Cooper pairs as roughly $2\Delta_0 = 2 \times 12/\sqrt{A}$. Ignatyuk *et al.* [38, 39] pioneered this phenomenological description of the NLD [38, 39].

Collective Enhancement Model

The CT and BSFG models implicitly incorporate collective effects through the energy dependent level density parameter, a. In contrast, the collective behaviors of nuclear vibrations and rotations are explicitly described by the Collective Enhancement Model (CEM) [34]. Beginning with an intrinsic level density $\rho_{int}(E, J, \pi)$ given by the Fermi Gas Model, the vibrational and rotational motions can be explicitly accounted for by $K_{rot}(E)$ and $K_{vib}(E)$, the rotational and vibrational enhancement factors, respectively. The deformed Fermi gas level density is given by

$$\rho_{def}(E, J, \pi) = K_{rot}(E) K_{vib}(E) \rho_{int}(E, J, \pi). \tag{2.29}$$

The shape of the nucleus plays an important role in the CEM, as it does in the case of fission where deformation is a key ingredient in the process [34]. The nuclear shape significantly influences rotational enhancement such that $K_{rot} \approx$ 10-100 while $K_{vib} \approx 3$. A criticism of the CEM is the implementation of a phenomenological damping factor that represents the decrease of rotational enhancement at high excitation energies. However, the CEM can be applied to various phenomenological level density model as well as to various excitation regions. For instance, below a high energy part E_M, the CTM is applied to the discrete level and low-energy region, while above E_M the CEM is applied in order to account explicitly for collective effects. As discussed throughout, this is an example of a matching problem between regions fit best by various phenomenological models describing the experimentally observed effects of collective behavior.

2.2.4 Microscopic Models

While phenomenological models utilize formulations that generally approximate a representative shape of the nuclear level density as well as employ adjustable parameters that tune to experimental data where available, phenomenological models do not sufficiently address shell effects, pairing effects, and parity distribution. Microscopic methods of calculating the level density, such as the Hartree-Fock-BCS (HF-BCS) [40, 41], Hartree-Fock-Bogolyubov plus combinatorial method (HFB-comb.) [42], and temperature-dependent Hartree-Fock-Bogolyubov [43] methods, are powerful predictive tools to employ when experimental data is not available These methods do, however, prove to be considerably computationally-costly. Relevant to the work presented in this dissertation, nuclear data for ^{93}Sr is sparse; there are only 20 known levels in a complete level scheme and no experimentally determined neutron resonance parameters. In Section 2.6, microscopic approaches to calculating the level den-

sity along with phenomenological models are utilized in an χ^2-minimization fit of neutron resonance data in the A = 93 mass region to estimate the NLD of ^{93}Sr.

2.2.5 Experimental Determination of Nuclear Level Density

Generally, at low energies the NLD is determined simply by counting discrete states obtained from γ-ray spectroscopy. The Oslo Method, which is discussed in greater detail in Chapter 4, offers an alternative approach to such a direct method, by measuring γ rays emitted as a function of excitation energy, from which primary γ rays can be isolated and the NLD and γSF can be extracted. It is important to note, however, that the extracted NLD and γSF both depend on normalization parameters obtained from available nuclear data. For unstable nuclei, experimental data may not be available and an estimate of normalization points from regional systematics is utilized. In cases where neutron resonance data is available from neutron capture experiments, the level density at the neutron separation energy is determined as the inverse of the measured average neutron resonance spacing for s-wave neutrons $D_{\ell=0}$, which then must be adjusted to the total level density over all angular momentum states using the spin-cutoff parameter. The three parameters used in the Oslo Method to normalize the NLD and γSF are discrete levels at low energy, the level density at the neutron separation energy, and neutron resonance parameters. The capture of an s-wave neutron results in spin states of $J = J_t \pm 1/2$, where J_t is the spin of the target nucleus, as well as equal formation of each parity; as a result, D_0 can therefore be written as a function of the level density of the capture state as described by Eq. 2.30:

$$\frac{1}{D_0} = \frac{1}{2}[\rho(S_n, J_t + 1/2) + \rho(S_n, J_t - 1/2)]. \tag{2.30}$$

In the case of ^{92}Sr(n,γ), since $J_t^\pi = 0^+$, the expression for D_0 can be written in the form shown in Eq. 2.31:

$$\frac{1}{D_0} = \frac{1}{2}\rho(S_n, 1/2), \tag{2.31}$$

and if D_0 is a known value, the total level density at S_n can be calculated by the expression: $\rho(S_n) = \frac{2}{D_0}\sum_{J=J_t\pm1/2}\frac{1}{g(S_n,J)}$. In Section 2.6, the available nuclear data for Sr isotopes used to determine the level density is discussed.

2.3 The γ-ray Strength Function

Bartholomew *et al.* [44] first defined the γSF as the distribution of the average transition widths of a particular multipole L and type X (either electric E or magnetic M) as a function of γ-ray energy, which can be expressed in the form shown in Eq. 4.19,

$$f_{XL}(E_\gamma) = \frac{\langle\Gamma_{XL}(E, J^\pi)\rangle}{E_\gamma^{2L+1} D_\ell}. \tag{2.32}$$

The γSF $f_{XL}(E_\gamma)$ depends only on the γ-ray energy E_γ, the total width $\langle \Gamma_{XL}(E, J^\pi) \rangle$ averaged over states of a given spin J and parity π around an energy E, and the ℓ-wave neutron level spacing D_ℓ (usually s- or p-wave). The width of a state is directly connected to the lifetime, τ, of the state ($\Gamma = \hbar/\tau$), and thus describes the state's decay probability. Moreover, the generalized Brink-Axel hypothesis [45, 46] leads to the assumption that the strength function for photoabsorption $\overrightarrow{f}_{XL}(E_\gamma)$ equals the strength function for de-excitation by emitting a γ ray, $\overleftarrow{f}_{XL}(E_\gamma)$.

The generalized Brink-Axel hypothesis [45, 46] states that the properties of the γSF at higher excited states are shifted upward in energy from, yet in all other manners identical to, those built on the ground state. Brink [45] and Axel [46] identify that if angular momentum and parity selection rules are followed, the photoabsorption cross section has the same dependence on the photon energy, regardless of whether or not the absorption occurred at the ground state or at an excited state. The photoabsorption cross section, $\sigma_{XL}(E)$, at an energy E depends on the probability of the reaction described by the width of the entrance channel, $\Gamma_{1=\gamma}$, in this case absorbing a photon, as well as the decay probability described by the width of the exit channel, Γ_2. The form of the $\sigma_{XL}(E)$ around a resonance is known as a Lorentzian function, shown in Eq. 2.33 [44],

$$\sigma_{XL}(E) \sim \frac{\Gamma_\gamma \Gamma_2}{(E - E_r)^2 + \left(\frac{\Gamma_\gamma + \Gamma_2}{2}\right)^2}. \tag{2.33}$$

Here E_r is the energy of a resonance, an energy where the σ_{XL} is enhanced. The $\overrightarrow{f}_{XL}(E_\gamma)$ can be determined from the average photoabsorption cross section, $\langle \sigma_{XL}(E) \rangle$, summed over all possible spins of final states [47, 48], described by Eq. 2.34:

$$\overrightarrow{f}_{XL}(E_\gamma) = \frac{1}{(2L+1)(\pi\hbar c)^2} \frac{\langle \sigma_{XL}(E) \rangle}{E_\gamma^{2L+1}}. \tag{2.34}$$

From the generalized Brink-Axel hypothesis, the strength function for emitting a γ ray is also related to the photoabsorption cross section. The generalized Brink-Axel hypothesis was beautifully illustrated by the work of L. Crespo Campo *et al.* [49] analyzing the primary γ-ray spectra of ^{64,65}Ni. This work has become a seminal study of the generalized Brink-Axel hypothesis as the Ni isotopes are light nuclei with a low NLD and thus larger Porter-Thomas fluctuations compared to the fluctuations observed for ^{238}Np which was investigated by M. Guttormsen *et al.* [50] to test the generalized Brink-Axel. Figure 2.6 presents the results of Reference [49], illustrating that the γSF does not change as a function of excitation energy.

As demonstrated, the γSF is related to the average total radiative width, the decay lifetime, and the photoabsorption cross section. In addition, the γSF can be obtained from the γ-transmission coefficient, $\mathscr{T}(E_\gamma)$ using Eq. 2.35:

$$\mathscr{T}(E_\gamma) = 2\pi f_{XL}(E_\gamma) E_\gamma^{2L+1}. \tag{2.35}$$

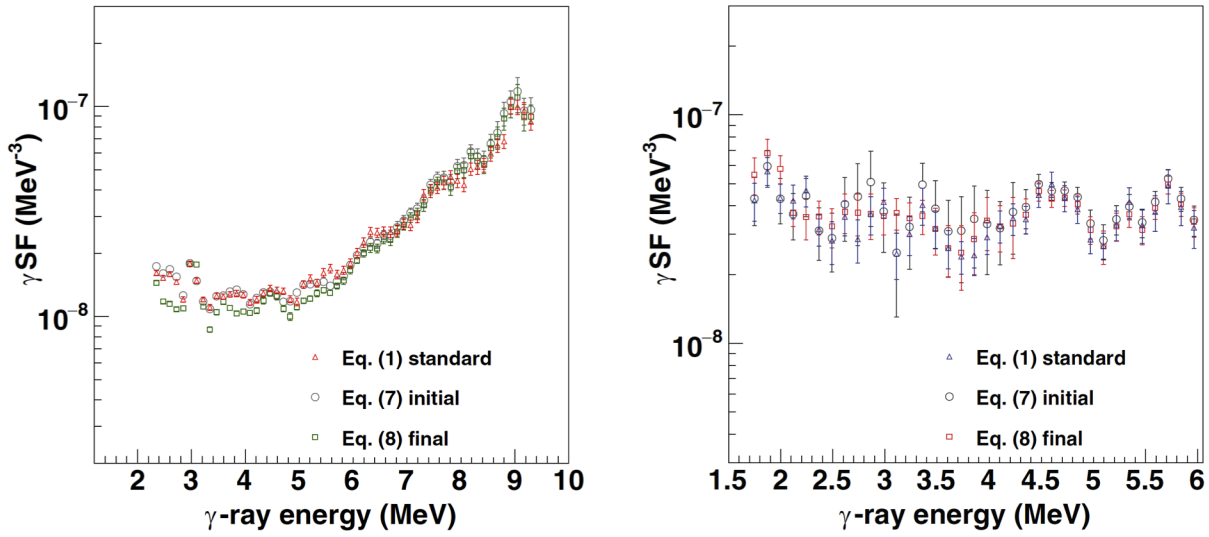


Figure 2.6: Experimental verification of the generalized Brink-Axel hypothesis for (a) ^{64}Ni and (b)^{65}Ni. The cited equations Eq. (1), (7), and (8) are those from Reference [49]. The excitation energy independent γSFs are compared to the γSFs obtained as a function of initial excitation energy, E_i and final excitation energy, E_f.

The γ-transmission coefficient (or γSF) and the NLD are simultaneously extracted from γ-ray spectra using the Oslo Method [9] and used in Hauser-Feshbach calculations to determine the neutron-capture cross section. The extracted $f_{XL}(E_\gamma)$ is characterized predominantly by the $E1$ strength observed as a broad resonance structure referred to as the Giant Dipole Electric Resonance (GDER), which prevails around and above the neutron separation energy [7]. The $E1$ and $M1$ strength functions together represent the Giant Dipole Resonance (GDR), and will be discussed in the following sections.

2.3.1 γ-ray Emission

The γ rays emitted from a nucleus in an excited state can reveal many properties about the nucleus itself, such as the energies, spins, parities, and branching ratios of excited states through conservation laws of energy, momentum, and angular momentum. Conservation of energy and momentum stipulate that a nucleus at rest of mass M decays from an initial excited state, E_i, to a final state, E_f, by emitting a γ ray of energy E_γ, which can be expressed using Eq. 2.36:

$$\begin{aligned} E_i &= E_f + E_\gamma + T_R \\ 0 &= p_R + p_\gamma. \end{aligned} \tag{2.36}$$

The final state is not at rest, but experiences a recoil with energy $T_R = p_R^2/2M$. The assumption is most often made that the recoil energy can be entirely neglected, therefore

the difference in energy of two states equals the γ-ray energy [7].

Unlike fermions, γ rays are massless particles of at least spin-1, in addition to being electromagnetic waves. The radiation field of an emitted γ ray, whether electric or magnetic, depends on the relative parity of the initial and final states, i.e., $\Delta\pi$, as well as the angular momentum of the γ ray. From conservation of angular momentum, the angular momentum, L (multipole) of the γ ray is determined by

$$|J_i - J_f| \leq L \leq J_i + J_f \quad (L \neq 0) \tag{2.37}$$

when the transition is from an initial state of angular momentum J_i to a final state of J_f. In addition, the parity selection rules describe the nature of the radiation field [7]:

1. if $\Delta\pi = 1$, the radiation is *magnetic* for L = even and *electric* for L = odd,
2. if $\Delta\pi = 0$, the radiation is *electric* for L = even and *magnetic* for L = odd.

For instance, a transition from an initial to final state $7/2^+ \rightarrow 3/2^+$ would occur with $E2$, $M3$, $E4$, or $M5$. The rate of each of these possible transitions varies dramatically.

Using Fermi's Golden rule, the probability to transition from the initial state i to final state f is given by Eq. 2.38,

$$T_{i\rightarrow f} = \frac{2}{\epsilon_0 \hbar} \frac{(L+1)}{L[(2L+1)!]^2} \Big(\frac{E_\gamma}{\hbar c},\Big)^{2L+1} |M_{f,i}|^2 \tag{2.38}$$

which shows a strong dependence on the matrix element squared $|M_{f,i}|^2$ for a γ-ray transition. The matrix element here is also known as the reduced transition probability, $B^{(XL)}_{i\rightarrow f}$, which relates to the decay width, Γ, and the photoabsorption cross section, $\sigma_{XL}(E)$, and is discussed in further detail in the Appendix A. The transition is dependent on the relative energy and angular momentum of the transition from an initial state ψ_i to a final state ψ_f. Solving $|M_{f,i}|^2$ for electric and magnetic transitions, the EL and ML transition probabilities can be determined. Weisskopf estimates of transition rates assume a single-particle model to calculate transition rates [7]. For instance, Weisskopf estimates applied to a medium size nucleus ($A = 125$) yield the following general trends,

1. the transition probability for EL is two orders of magnitude larger than ML,
2. depending on the γ-ray energy, the transition probability of type X for L is five to ten orders of magnitude greater than XL' (where $L' = L + 1$),
3. and depending on the γ-ray energy, the transition probability for ML is five to ten orders of magnitude greater than EL' (where $L' = L + 1$).

Experimentally, some observed transition probabilities are several orders of magnitude smaller than the Weisskopf estimates, which suggests dissimilar initial and final states. In contrast, observed transition probabilities that are several orders of magnitude larger than the

Weisskopf estimates indicate that a collective behavior model is more representative of the nucleus.

A competing mechanism to γ decay is internal conversion. Internal conversion is the process whereby the energy from the nucleus is transferred to an orbital electron. This electromagnetic process is the only decay pathway when $J_i = J_f = 0$ thus resulting in $L = 0$, a prohibited radiation transition. For an experimental setup using a Total Absorption Spectrometer (TAS), internal conversion could contribute an uncertainty to excitation energy measurements.

2.3.2 Porter-Thomas

At low excitation energies, the properties of individual states are generally known from experimental data, whereas at high excitation energies, such properties are usually described using a statistical approach. C. E. Porter and R. G. Thomas [51] observed that partial radiative widths, $\Gamma_{i\gamma f}$, of initial to final states ($i \rightarrow f$) fluctuate. The work of Porter and Thomas showed that the reduced partial radiative widths for a compound nucleus follow a χ^2 distribution with one degree of freedom called the Porter-Thomas distribution:

$$P(x) = \frac{1}{\sqrt{2\pi x}} e^{-x/2}, \tag{2.39}$$

whereby x is the reduced partial radiative width $x = \Gamma_{i\gamma f}/\bar{\Gamma}_{i\gamma f}$.

2.3.3 Photon Response in Nuclei

The collective excitation of the nucleus results in several prominent structures, such as the Giant Dipole Resonance (GDR), the Pygmy Resonance, and Scissors Resonance. Each of these structures are shown in Fig. 2.7, which depicts the relative characteristics of each structure. The GDR is dominated by $E1$ transitions (i.e., Giant Dipole Electric Resonance) of statistical γ decay around particle emission energies. In other words, the γSF is a maximum at about 10-18 MeV. In Fig. 2.7, the plot of the γSF as a function of γ-ray energy illustrates the macroscopic properties of the GDER such as the centroid at $\sim$14 MeV, the width of 2-5 MeV, and the strength as a significant portion of the γ absorption/emission probability. The strength of the GDER, Pygmy Resonance, and Scissors Resonance can be expressed in terms of Thomas-Reiche-Kuhn (TRK) sum rule:

$$\int_0^\infty \sigma(E_\gamma) dE_\gamma = \frac{2\pi^2 e^2 \hbar}{mc} \frac{NZ}{A} \approx 60 \frac{NZ}{A} \text{ MeV mb}, \tag{2.40}$$

where $\sigma(E_\gamma)$ is the photoabsorption cross section. A large portion of TRK sum rule is exhausted by the GDER, while the remaining strength is divided among various other resonances.

From the macroscopic perspective of the nucleus described by the liquid drop model, proton fluid and neutron fluid have a range of vibrational and rotational motion as shown in

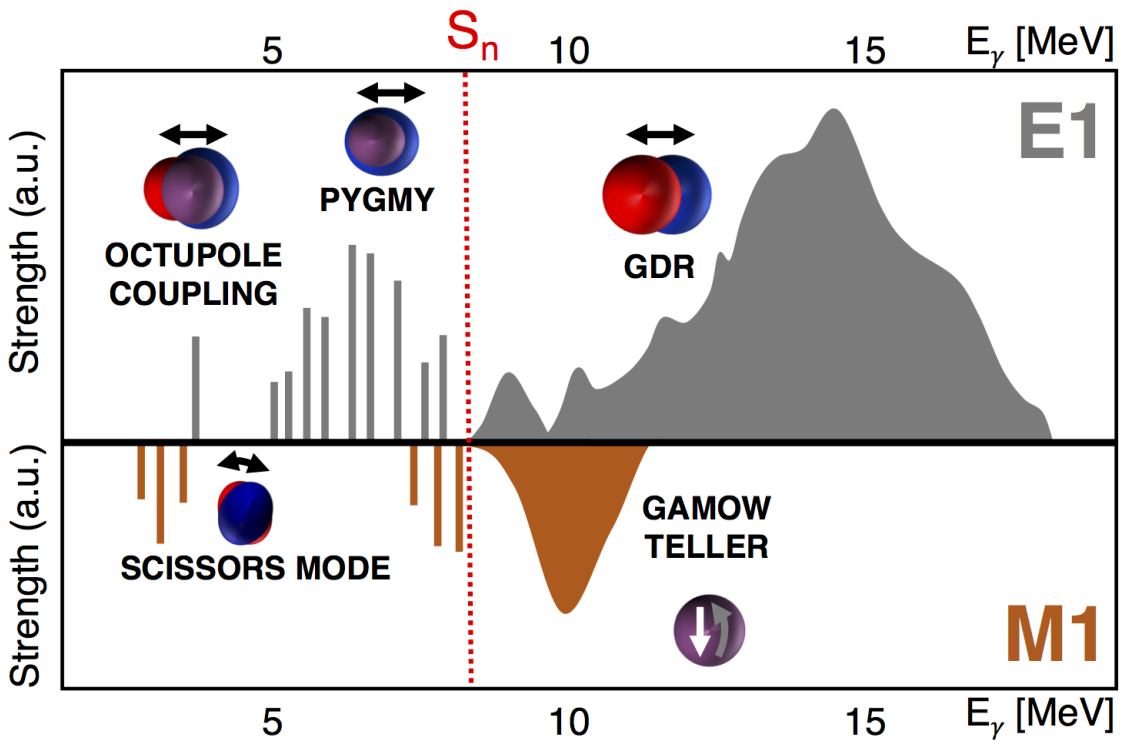


Figure 2.7: Dipole response in nuclei. Illustration of γ-ray strength function as a function of γ-ray energy depicting possible electric or magnetic dipole ($E1$ or $M1$) resonances produced by collective excitations in the nucleus. Illustration is taken from Reference [52].

Fig. 2.8. The motion of proton and neutron fluid, which is observed as a giant resonance in measurements of photoabsorption cross sections (and consequently, γSF), can be described in terms of the quantum numbers: multipolarity L, spin S, and isospin T. Isoscalar electric vibrations ($S = 0$ and $T = 0$) represent in phase oscillation of proton and neutron fluid, while isovector electric vibrations ($S = 0$ and $T = 1$) represent out of phase oscillation of proton and neutron fluid. Similarly, $S = 1$ modes represent oscillations where the spin of protons is flipped relative to the spin of neutrons. The GDER is a measurable observation of this underlying motion of protons and neutrons in the nucleus known as isovector giant dipole electric resonance (IVGDER). For deformed nuclei, the GDER is characterized as a double peak Lorentzian.

The Pygmy Dipole Resonance (PDR) is a low-lying $E1$ resonance theorized to be split into two parts, an isoscalar and isovector response as observed by (α, $\alpha'\gamma$) and (γ, γ') experiments, respectively. Compared to the GDER, the PDR only exhausts 1% of the TRK sum rule. Suzuki *et al.* generalized the concept of the PDR as the motion of excess protons and neutrons relative to a closed core nucleus [54]. While the GDER is visible for all nuclei, the PDR strength is enhanced for deformed nuclei as well as with increasing number of

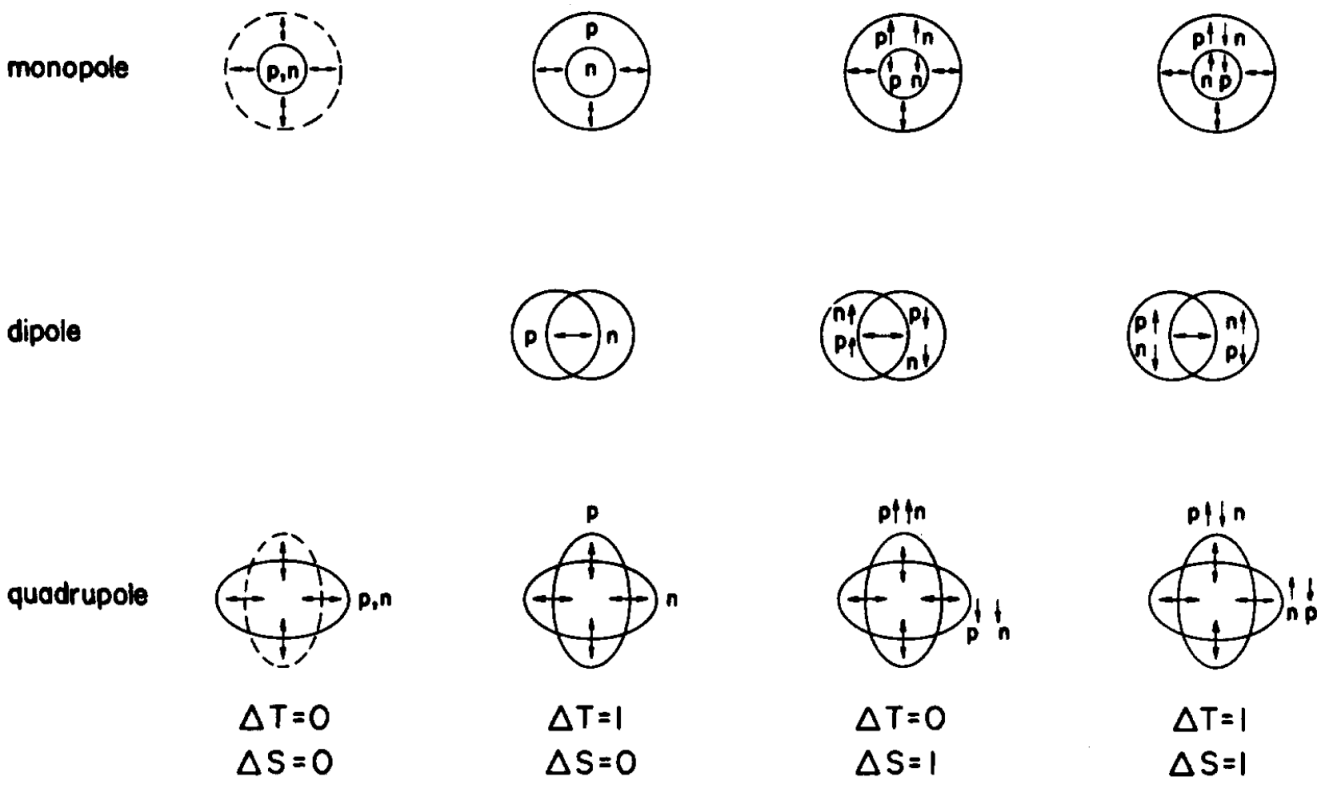


Figure 2.8: Giant resonance modes of the nucleus. Macroscopic description of the basic excitation modes in the nucleus in terms of the quantum numbers: multipolarity L, spin S, and isospin T. Monopole ($L = 0$), dipole ($L = 1$), and quadrupole ($L = 2$) resonances are either isoscalar ($T = 0$) or isovector ($T = 1$) and either electric ($S = 0$) or magnetic ($S = 1$). Chart is taken from Reference [53].

neutrons and linked to shell effects [55].

The Gamow-Teller (GT) Resonance is an $M1$ collective excitation at 6-10 MeV represented by the quantum numbers: $\Delta L = 0$, $\Delta S = 1$, and $\Delta T = 1$ and known as a spin-isospin flip resonance [56]. While the GT Resonance is observable in medium-heavy nuclei, the $M1$ strength is small relative to the $E1$ strength as well as heavily mixed with the $E1$ strength. The GT Resonance was first observed by Doering *et al.* in a ^{90}Zr(p, n)-experiment [57].

The Scissors Resonance is a low-lying $M1$ resonance that was first theoretically predicted by Bohr-Mottelson model in 1975 and experimentally observed in the strongly deformed nucleus ^{156}Gd by D. Bohle *et al.* in 1984. Several characteristics observed by studies of the scissors mode for chains of isotopic nuclei, such as Xe, Ba, Ce, Nd and Sm, are an excitation energy that remained constant with mass number A and a $M1$ strength that increases with the square of the deformation parameter. A simplified macroscopic description of the Scissors Resonance is a rotational oscillation of proton fluid versus the neutron fluid. Early calcula-

tions of the $M1$ strength based on this geometric collective model overestimated the strength compared to experimental values [56]. In addition to considering deformation correlations, later calculations considered pairing correlations, which reduced the number of protons and neutrons to valence nucleons only participating in the scissors motion. The resulting calculated $M1$ strength was too large by only a factor of two compared to experimental values [56].

2.3.4 γ-Ray Strength Function Models

In Chapter 5, the experimentally determined γSF for ^{93}Sr is compared to several of the prevailing GDER models discussed here. The Giant Dipole Magnetic Resonance (GDMR) can also be described with a Lorentzian function. However, scarce amount of experimental data for the $M1$ strength in this mass region is available as the $M1$ strength is weak relative to the $E1$ strength. The total dipole strength is as follows:

$$f(E_\gamma) = f_{E1}(E_\gamma) + f_{M1}(E_\gamma). \tag{2.41}$$

The first f_{E1} model considered is the Brink-Axel (BA) model, or the Standard Lorentzian (SLO), parameterized by resonance structures: centroid energy, E_G (in MeV), width, Γ_G (in MeV), and cross section, σ_G (in mb) and given by Eq. 2.42:

$$f_{BA}(E_\gamma) = \frac{1}{(2L+1)(\pi\hbar c)^2}\frac{\sigma_G E_\gamma \Gamma_G^2}{(E_\gamma^2 - E_G^2)^2 + E_\gamma^2\Gamma_G^2}. \tag{2.42}$$

In the case of $E1$ strength, the resonance structures are those of the GDER and $L = 1$. For deformed nuclei which are charactered by a double hump GDER, the SLO model is a sum of two Lorentzian curves. The SLO model as well as additional theoretical models are plotted along side photoabsorption data of stable Sr isotopes in Fig. 2.9 [48].

An alternative model proposed by J. Kopecky and M. Uhl [58] is the Generalized Lorentzian (GLO) model which incorporates an energy- and temperature-dependent width $\Gamma_k(E_\gamma, T)$. In the case of characterizing the $E1$ strength, the GLO model is expressed by Eq. 2.43,

$$f^{E1}_{GLO}(E_\gamma, \Theta) = \frac{\sigma_G\Gamma_G}{3(\pi\hbar c)^2}\Big[\frac{E_\gamma\Gamma_k(E_\gamma, T)}{(E_\gamma^2 - E_G^2)^2 + E_\gamma^2\Gamma_k^2(E_\gamma, T)} + 0.7\frac{\Gamma_k(E_\gamma = 0, T)}{E_G^3}\Big], \tag{2.43}$$

where $\Gamma_k(E_\gamma, T)$ is defined as

$$\Gamma_k(E_\gamma, T) = \frac{\Gamma_G}{E_G^2}(E_\gamma^2 + 4\pi^2 T). \tag{2.44}$$

In some formulations of the GLO model, the nuclear temperature T of the final state is dependent on the excitation energy of final states, which violates the generalized Brink-Axel hypothesis. The (Enhanced) Generalized Lorentzian (EGLO) is essentially a form of Eq.

2.43 with an additional empirical function so as to better reproduce experimental data of deformed nuclei.

Other models of the γSF also describe the strength as a Lorentzian function, such as the model based on Fermi liquid theory proposed by Kadmenskiĭ, Markushev, and Furman (KMF) [59] and the Modified Lorentzian (MLO) model [48, 60, 61]. These models, in addition to SLO and (E)GLO, have some drawbacks including the inability to describe structures at low E_γ, as well as to represent the $E1$ strength of exotic nuclei [48]. Formulations of these additional models are included in the Appendix B. Figure 2.9 illustrates the differences between these theoretical γSF at low γ-ray energy.

Alternatively, a more complex approach is to utilize microscopic models to predict in a more reliable manner the behavior the GDER and low-lying resonance structures. For instance, the nuclear reaction code TALYS utilizes the random-phase approximation (RPA) microscopic approach. Furthermore, S. Goriely and E. Khan calculated the γSF using Quasi-particle RPA (QRPA) model for more than 6000 nuclei [62]. In addition to the theoretical Lorentzian function based models describing the giant resonance, the tabulated QRPA-based γSF is an additional option when experimental nuclear data is sparse for neutron-rich nuclei.

2.3.5 Indirect Techniques for Extracting γSF from Experimental Data

Generally, the γSF is extracted from experimental photoabsorption measurements [64] reported by the Reference Input Parameter Library (RIPL-3) [36] and Experimental Nuclear Reaction Data (EXFOR) library [65]. Photoabsorption experiments rely on a stable target to measure, for example, the (γ, xn) cross section to determine the (n, γ) cross section. The incident photon beam is generated, for instance, by bremsstrahlung radiation which has a broad excitation energy range with no selectivity of excitation energy. Consequently, the measured photon response of the nucleus includes the full excitation energy range up to the endpoint-energy bremsstrahlung beam. Bremsstrahlung beams of different endpoint-energies are used to irradiate the target, and after subtracting the measured response for the lower bremsstrahlung endpoint-energy, the photon response for a single energy is obtained. Another experimental method is nuclear resonance fluorescence (NRF), where photons scatter on selected states of the target absorber nucleus [66]. For NRF experiments, the (γ, γ') interaction can be produced by bremsstrahlung beams or Laser Compton Scattering (LCS) γ rays, which produces a tunable beam of quasi-monochromatic γ rays. However, for short-live nuclei such measurements are not possible.

Alternatively, when the γSF cannot be extracted directly from experimental photoabsorbtion data, various indirect methods can be used, such as surrogate techniques [67], the standard Oslo Method [9], the β-Oslo Method [10], and the standard Oslo Method in inverse kinematics [68] to generate the γSF. Surrogate techniques and the Oslo method utilize charged particle reactions: e.g., ^{234}U(t, pf) for surrogate techniques and (^{3}He, $\alpha\gamma$) and (^{3}He, ^{3}He'γ) for the Oslo Method. While surrogate techniques were originally used to obtain (n,

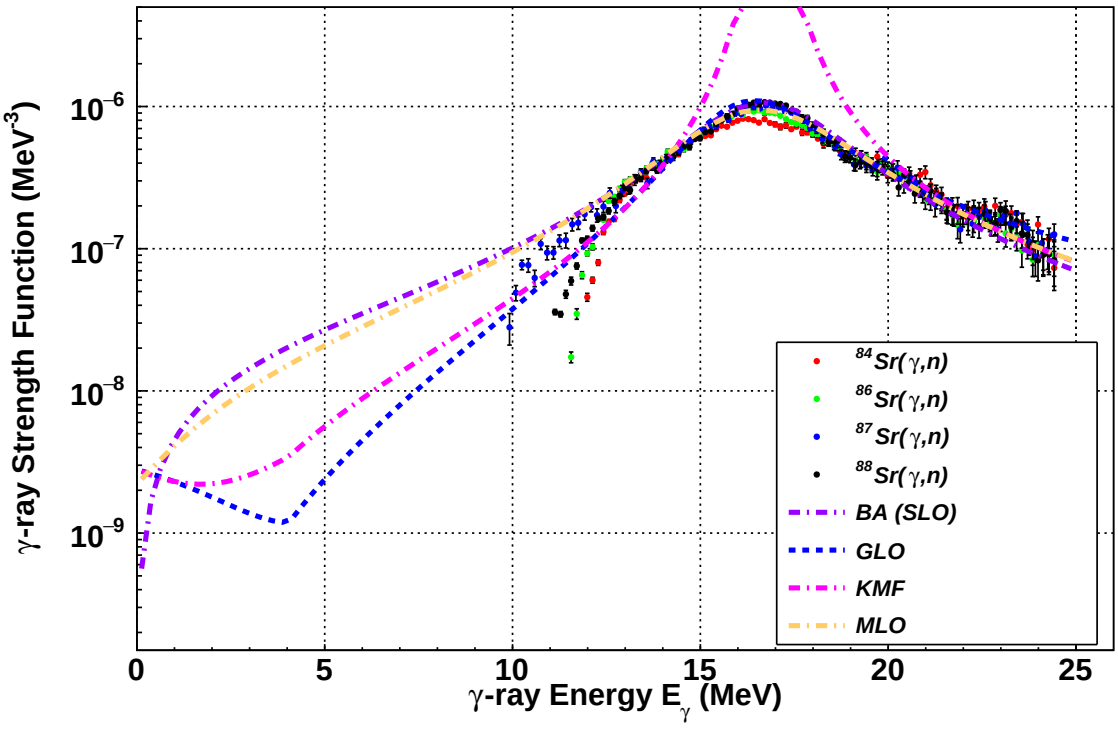


Figure 2.9: γSF calculated from photoabsorption cross sections of stable Sr isotopes obtained from Reference [63]. The dashed curves represent theoretical γSF models using GDER parameters of $^{\text{avg}}$Sr: $E_G = 16.94$ MeV, $\Gamma_G = 4.50$ MeV, and $\sigma_G = 206.00$ mb [36].

f), the surrogate $(d, p\gamma)$ reaction is an alternative means to determining the (n, γ) reaction for short-lived isotopes. The Oslo Method is also used to determine (n, γ) cross sections by extracting NLD and γSF from γ-ray spectra and normalizing the statistical nuclear properties to structural properties of the nucleus: discrete levels, level density at the neutron separation energy (obtained from the average s-wave neutron resonance spacing D_0), and the mean total radiative width, $\langle\Gamma(S_n)\rangle$. In contrast, the surrogate technique used for obtaining (n, γ) cross sections does not require additional nuclear properties; however, there are several challenges in performing such surrogate techniques. For instance, the mismatch between the spin-parity populations produced in the surrogate reaction and the desired reactions as well as identifying γ rays emitted from high excitation energies are challenges in accurately determining the neutron-capture cross section. For instance, A. Ratkiewicz *et al.* demonstrated $(d, p\gamma)$ as a surrogate reaction for (n, γ) in the case of ^{95}Mo [69]. A. Ratkiewicz *et al.* use a recently developed (d, p) reaction description to account for the spin-parity mismatch. In this method, the outgoing particle of the surrogate reaction is measured in coincidence with the γ emission to determine the γ branching ratio. The γ branching ratio

is the most uncertain quantity compared to the formation cross section, both of which are utilized by the Hauser-Feshbach formalism in calculating the neutron-capture cross section.

The β-Oslo Method, discussed in greater detail in Chapter 4, and the standard Oslo Method in inverse kinematics are both derived following the assumptions and techniques of the standard Oslo Method. Briefly, the β-Oslo Method is used to extract the NLD and γSF from measured γ rays emitted from a CN in coincidence with β particles emitted from the β-decay parent. The standard Oslo Method in inverse kinematics is applied to measured particle-γ coincidences obtained from experiments where a radioactive heavy ion beam impinges on a light target. While the three Oslo Methods depend on the structural properties of the nucleus, these indirect methods provide constraints on uncertainties of neutron-capture cross section data that vary by several orders of magnitude for nuclei far from stability.

2.4 Optical Model Potential

The goal of this work is to determine the neutron-capture cross section for ^{92}Sr via an indirect method where statistical properties of the compound nucleus ^{93}Sr are extracted from experimental γ-ray spectra. The statistical properties of ^{93}Sr, the NLD and γSF, describe the nucleus following the capture of a neutron. The mechanisms of the initial interaction between the target nucleus ^{92}Sr and the incoming neutron, however, are not completely understood.

Through the use of a neutron optical model, various characteristics of the initial interaction can be estimated based on the assumptions of various models, which are categorized as either phenomenological or microscopic optical model potentials (OMP). Phenomenological models assume a potential, such as a Woods-Saxon form, and also adjust parameters according to available experimental data. Parameterization of the OMP heavily depends on the availably of experimental data and can follow one of three methods: the *best-fit* optical model, representing a single nucleus and incident energy; the *local* optical model, representing a single nucleus and energy region; and the *global* optical model, representing a mass and energy region. In addition, the parameterization can be tailored to include isospin dependence and deformation. The standard (near-)spherical OMP developed by Koning and Delaroche [70] determined that using a spherical optical model resulted in an overestimation of the total cross section by 10% compared to experimental values. In the case of limited experimental data, a global parameterization of the OMP is used. In addition to phenomenological models, the semi-microscopic model known as the Jeukenne-Lejeune-Mahaux (JLM) model [71] is another commonly used model in TALYS to calculate neutron-capture cross sections. The neutron-capture cross section calculated using the Hauser-Feshbach formalism, which relies on the NLD, γSF, and neutron OMP, is highly sensitive to the uncertainties of the NLD and γSF compared to the uncertainty of the OMP. For instance, Liddick *et al.* varied optical models for isotopes in the nuclide range Z = 25 - 31, resulting in neutron-capture cross sections which varied by 6% on average [72]. In Chapter 6, various optical models are

implemented in calculating the neutron-capture cross section and the results are compared.

2.5 Hauser-Feshbach Formalism

The Hauser-Feshbach formalism used to calculate the neutron-capture cross section is based on the compound nucleus hypothesis of Niels Bohr [21]. The probability of an interaction between a target nucleus and an incoming nucleon is independent of the decay probability of the intermediate state formed following the interaction, which can be expressed in terms of an interaction cross section, σ_a, and decay cross section, σ_b. In Eq. 2.45, the total cross section for neutron-capture for a given excitation energy, E_x, of the compound nucleus is given as

$$\sigma_{a,b}(E_x) = \frac{\pi}{k_a^2} \sum_{J,\pi} \frac{2J+1}{(2J_a+1)(2J_b+1)} \frac{T_a(E_x J,\pi) T_b(E_{x,J,\pi})}{\sum_l T_l(E_x, J, \pi)}. \tag{2.45}$$

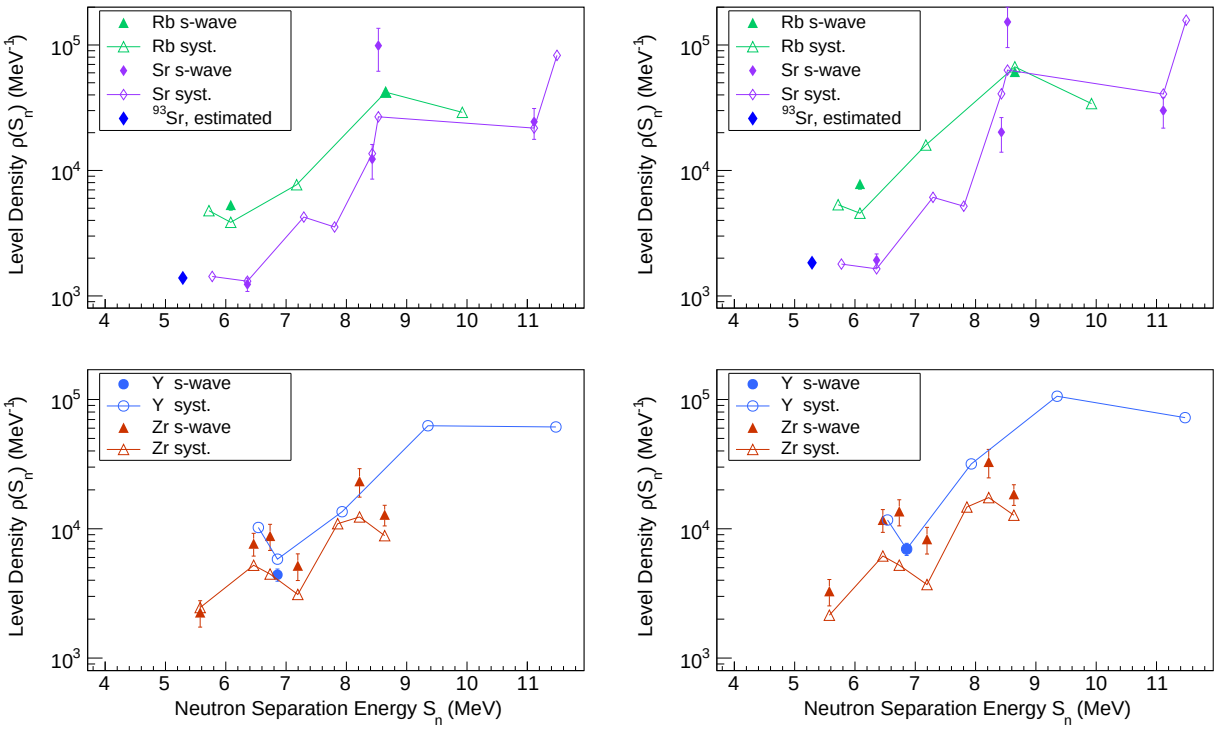
The transmission coefficient of an entrance or exit channel, c, is directly related to the cross section of the channel as the sum of partial waves and is expressed as follows

$$\sigma_c = \frac{\pi}{k_c^2} \sum_l (2l+1) T_c^l = \frac{\pi}{k_c^2} T_c, \tag{2.46}$$

where k_l is the wave number of the l^{th} partial wave, which is approximated as zero for low energies and short range potentials, such as the strong nuclear force. Indirect methods such as the β-Oslo Method can be used to experimentally determine the γSF used to obtain the exit channel: the γ-transmission coefficient, T_b, and the NLD. Knowing the NLD is necessary for both determining the slope of the γSF and for estimating the entrance channel transmission coefficient. While the NLD and γSF are statistical nuclear properties extracted from experimental data using β-Oslo Method, the transmission coefficient of the initial interaction is obtained from an OMP.

2.6 Databases of Neutron Resonance Parameters

The main source of level density parameters and neutron resonance parameters used in this work is the Reference Input Parameter Library (RIPL-3) [36]. The Oslo Method utilizes three normalization points to obtain a NLD and γSF: discrete levels at low excitation energy, the level density at the neutron separation energy (determined by using Eq. 2.31 with experimentally-known D_0), and $\langle \Gamma_0 \rangle$. Of the 91 discrete levels reported by the Evaluated Nuclear Structure Date File (ENSDF) [25] for ^{93}Sr, over two-thirds of the levels were determined through β-decay measurements, while the remaining levels were determined from spontaneous fission of ^{252}Cf and βn decay measurements. A plot of the level density of reported discrete states is shown in Fig. 2.5. The NLD of discrete levels up to 2 MeV follows the CT model reasonably well, and though there are states reported up to 6.71 MeV, many high-lying states are not experimentally known.



(a) Spin-Cutoff Parameter calculated with Back-Shifted Fermi Gas Model

(b) Spin-Cutoff Parameter calculated with Rigid Moment of Inertia Model

Figure 2.10: The unknown $\rho(S_n)$ of ^{93}Sr (blue diamond) is estimated from systematics of neutron resonance parameters of isotopes in the Sr mass region. For stable Rb, Sr (top), Y, and Zr (bottom) isotopes, the NLD was calculated using experimental D_0 and compared to predictions from the global systematics of References [30, 31, 32] through a χ^2-minimization. Figure 2.10a compares calculated and predicted value of $\rho(S_n)$ using the σ_{BSFG} approach. Figure 2.10b compares calculated and predicted value of $\rho(S_n)$ using the σ_{RMI} approach.

For exotic nuclei far from stability, parametrized NLD models based on regional systematics serve as an acceptable alternative approach to estimating neutron resonance parameters. As little nuclear data are available for Sr isotopes heavier than A=88 as reported by RIPL-3, stable Sr isotopes as well as neighboring isotopes of Rb, Y, and Zr were used to estimate the normalization parameters for ^{93}Sr. Figure 2.10 presents an illustration of the landscape of available neutron resonance parameters in the Sr mass region and the estimated values for ^{93}Sr. The neutron resonance spacing, D_0, of ^{86,88}Rb, ^{85,87,88,89}Sr, ^{90}Y, and $^{91-95,97}$Zr taken from Reference [36] were used to calculate $\rho(S_n, J)$ by Eq. 2.31. In addition, several phenomenological approaches to calculating the spin-cutoff were used to determine the total

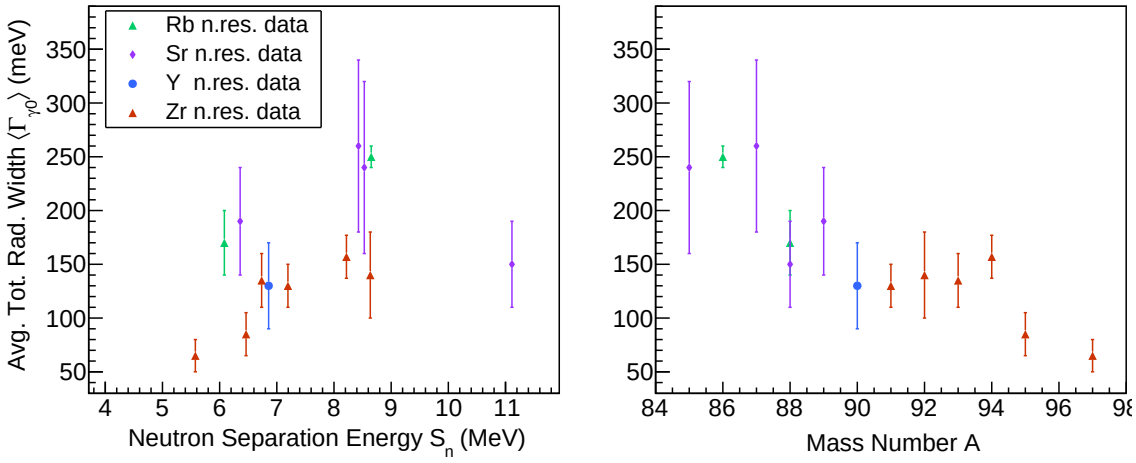


Figure 2.11: The experimental average total radiative widths at the neutron separation energy for ^{86,88}Rb, ^{85,87,88,89}Sr, ^{90}Y, and $^{91-95,97}$Zr are plotted as a function of the neutron separation energy (left-hand side) and mass number A (right-hand side)[36].

level density by the expression:

$$\rho(S_n) = \frac{2\sigma^2}{D_0} \frac{1}{(J_t+1)\exp[-(J_t+1)^2/2\sigma^2] + J_t\exp[-J_t^2/2\sigma^2]}, \tag{2.47}$$

where J_t is the spin of the target nucleus. Egidy and Bucurescu [30, 31, 32] put forth several phenomenological approaches to determining σ. The approaches examined are the energy-dependent σ developed from a study of 310 nuclei, and is as follows:

$$\sigma^2_{BSFG} = 0.391A^{0.675}(E - 0.5P_{a'})^{0.312}, \tag{2.48}$$

expressed as a function of excitation energy, E, and a Fermi Gas model that assumes the nucleus is a rigid sphere of radius $R = 1.25A^{1/3}$ fm and a function of nuclear temperature, T:

$$\sigma^2_{RMI} = 0.0145A^{5/3}T. \tag{2.49}$$

In Eq. 2.48, the deuteron pairing energy, $P_{a'}$, is calculated from tabulated masses. These phenomenological models are used in Eq. 2.47 along with experimental values of D_0 to determine $\rho(S_n)$. These values are compared to the predicted NLD obtained from the global systematics through χ^2-minimization fit, which results in a scaling factor of 0.34 for σ_{BSFG} and 0.31 for σ_{RMI}. The estimated values of $\rho(S_n)$ for ^{93}Sr in Fig. 2.10 are 1390.46 MeV^{-1} for σ_{BSFG} and 1838.05 MeV^{-1} for σ_{RMI}. For this χ^2-minimization fit, even-odd, odd-odd, and even-even nuclei were included; however, if the fit was applied to only even-odd nuclei (as is the case of ^{93}Sr), then $\rho(S_n)$ for ^{93}Sr is 1472.26 MeV^{-1} for σ_{BSFG}. These estimated values for the NLD for ^{93}Sr are a factor of 2 to 4 times smaller than estimates obtained from tabulated level densities calculated using HF-BCS microscopic model.

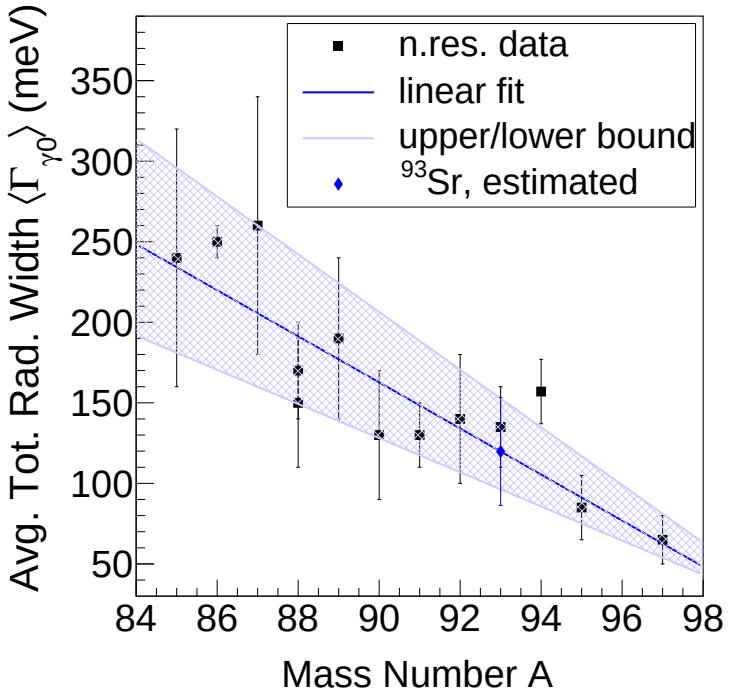


Figure 2.12: The estimated $\langle\Gamma_0\rangle$ for ^{93}Sr (blue diamond) obtained from a linear fit of known values for ^{86,88}Rb, ^{85,87,88,89}Sr, ^{90}Y, and $^{91-95,97}$Zr is 119.8±27% meV and is plotted as a function of mass number A [36]. The upper- and lower-bounds are linear fits to the uncertainty in $\langle\Gamma_0\rangle$.

The $\langle\Gamma_0\rangle$ is dependent on both the NLD and D_0 by the relationship given in Eq. 2.50:

$$\langle\Gamma(S_n, J_{cs}, \pi_{cs})\rangle = \frac{1}{\rho(S_n, J_{cs}, \pi_{cs})} \sum_{XL} \sum_{J_f,\pi_f} \int_{E_\gamma=0}^{S_n} dE_\gamma E_\gamma^{2L+1} \times f_{XL}(E_\gamma)\rho(S_n - E_\gamma, J_f, \pi_f). \tag{2.50}$$

Consequently, the γSF, $f(E_\gamma) = f_{E1}(E_\gamma) + f_{M1}(E_\gamma)$, a statistical nuclear property extracted from experimental γ-ray spectra using the Oslo Method, can be normalized to the $\langle\Gamma_0\rangle$ and D_0 which are previously known resonance parameters. The normalization process of the Oslo Method is discussed in detail in Section 4.4. Similar to the case of experimental D_0 values, the $\langle\Gamma_0\rangle$ of unstable nuclei is generally unknown and must be estimated from systematics of the mass region or calculated used microscopic models. Once more, neutron resonance parameters of stable ^{86,88}Rb, ^{85,87,88,89}Sr, ^{90}Y, and $^{91-95,97}$Zr isotopes taken from Reference [36] were examined as a function of neutron separation energy, S_n, and mass number, A, as shown in Fig. 2.11. As a function of S_n, there is no visible trend of $\langle\Gamma_0\rangle$ values in this mass region. However, a linear trend is visible for $\langle\Gamma_0\rangle$ as a function of A as shown in the right-hand side panel of Fig. 2.11. The unknown $\langle\Gamma_0\rangle$ for ^{93}Sr was estimated from a linear fit

of available data from Reference [36] as a function of A, and thus for $\langle\Gamma_0(^{93}\mathrm{Sr})\rangle = 119.8$ meV with an uncertainty of 27% was obtained.

Another hurdle is that current photoabsorption data of Sr isotopes is available for only stable isotopes. The Experimental Nuclear Reaction Data (EXFOR) [65] library reports photoabsoroption cross sections above $E_\gamma = 11$ MeV for ^{88}Sr(γ,n), ^{87}Sr(γ,n),^{86}Sr(γ,n), and ^{84}Sr(γ,n). Data were obtained from a campaign undertaken by A. M. Goryachev and G. N. Zalesnyy to measure the (γ, n) cross sections of zinc, germanium, selenium, and strontium isotopes [63]. At the Betatron of Saratov Gosudarstvennyi University, Russia, A. M. Goryachev *et al.* measured the photon scattering of Zn, Ge, Se, and Sr isotopes through single target irradiation using bremsstrahlung radiation of electron beams of various maximum kinetic energy. In Reference [63], the photoabsorption cross sections obtained for ^{88}Sr(γ,n), ^{87}Sr(γ,n),^{86}Sr(γ,n), and ^{84}Sr(γ,n) are across an energy range of 12 to 24 MeV. The γSF for these Sr isotopes are plotted in Fig. 2.9 along with the SLO, GLO, KMF, and MLO models using GDER parameters for $^{\mathrm{avg}}$Sr reported by RIPL-3 [36]. The peak of ^{88}Sr γSF is described well by SLO and GLO models; however, the behavior of the γSF at low γ-energy is experimentally unknown.

The landscape of currently available nuclear data for ^{93}Sr lacks information regarding both neutron resonance parameters and the average total radiative width, two of the three critical normalizing points of the β-Oslo Method. However, the previously demonstrated successes of using the β-Oslo Method to constrain the neutron-capture cross section for other nuclei lacking rich nuclear data, such as ^{76}Ge [10] and ^{89}Y [73] as well as many other nuclei using the standard Oslo Method, suggests the β-Oslo Method can be reasonably applied to ^{93}Sr. The work of this dissertation is to supply much needed understanding of nuclear structure properties at low γ-ray energies for the neutron-rich ^{93}Sr β-Oslo.

t

Chapter 3

Experimental Setup: β decay of ^{93}Rb

The experiment featured in this dissertation, titled "Determination of the ^{92}Sr Neutron-Capture Cross Section and Fission Product Burn Up", was performed over the course of one week beginning July 13, 2018 at the National Superconducting Laboratory (NSCL). A thermal beam of ^{93}Rb was produced utilizing the combined techniques of fast fragmentation, fragment separation, and beam thermalization. The eight-fold segmented NaI(Tl) cylinder detector, SuN [74], was installed in combination with the Tape station for Active Nuclei (SuNTAN) at the experimental end-station in order to remove daughter activity. This chapter discusses the accelerator facility, the experimental detector setup, and the data analysis technique of total absorption spectroscopy.

3.1 Thermalized Radioactive Isotope Beam

The Couple Cyclotron Facility (CCF) at the NSCL accelerates stable ions through the K500 cyclotron and injects them into the K1200 cyclotron in order to produce a fast primary stable ion beam. The primary beam impinges on a thin production target which, by means of fast fragmentation reactions, produces a variety of rare radioactive ion beams. The fragments are then separated using the A1900 fragment separator, producing a beam of the desired isotope with high purity which is transported to the beam thermalization region before delivery to the experimental-end-station. A diagram sketch of this experimental setup is featured in Fig. 3.1.

In the featured experiment, a primary beam of $^{96}Zr^{37+}$ was accelerated to 120 MeV/nucleon through the CCF and impinged on a ^{9}Be target, which had a thickness of 394.29 mg/cm^2. The A1900 utilizes both dipole and quadrupole magnets to filter and focus the beam of fragments as well as an Al wedge degrader with a thickness of 151.97 mg/cm^2 to achieve isotopic separation through nuclear charge and kinematic velocity [75]. After the A1900, the secondary beam of ^{93}Rb is then transported to the beam thermalization area (N4 vault), which consists of solid degraders, a monchromatic wedge, and a large volume linear gas cell constructed by Argonne National Lab (ANL) [76, 77]. The ^{93}Rb ions, with an energy of ap-

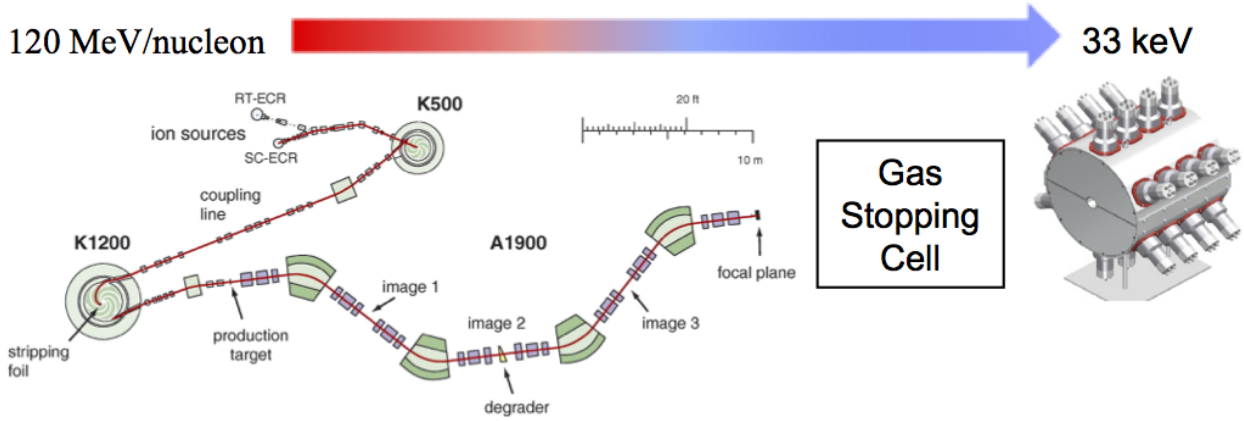


Figure 3.1: Layout of the beam line at the NSCL beginning with a fast primary beam produced by the CCF that hits a production target producing a beam of many radioactive isotopes. The beam travels through the A1900 fragment separator to obtain a high-purity beam of the desired isotope. At the gas stopping cell, the secondary beam (the desired isotope) is slowed to 33 keV. The stopped beam is then transported to the experimental-end-station: the Low Energy Beam and Ion Trap (LEBIT) area, where the Summing NaI(Tl) detector (SuN) [74] is installed at the end of a new beam line extension.

proximately 33 keV and intensity of 12 particles per second, were implanted onto a 9-track magnetic tape placed in the center of the borehole of SuN located at the experimental-end-station.

3.2 Detector Setup

After being delivered to the experimental end-station, the thermal beam of ^{93}Rb subsequently β decays, emitting a β particle and γ rays simultaneously. While the γ rays are detected with the high-efficiency total absorption spectrometer known as SuN, the β particles are detected by a plastic scintillator detector. In addition, a 9-track magnetic tape was installed in the center of the detector setup, as illustrated by Fig. 3.2, to remove contamination from the decay products. This section provides details on the components of the detector setup and measurement technique.

3.2.1 Total Absorption Spectroscopy (TAS)

The β decay of ^{93}Rb is an ideal probe of the compound nucleus ^{93}Sr due to the large Q-value ($Q_{\beta^-} = 7.466(9)$ MeV) compared to the neutron separation energy ($S_n(^{93}\mathrm{Sr}) = 5.290(8)$ MeV), thus enabling the access of highly-excited states around S_n. In current evaluated nuclear data libraries, 74 of the 91 levels reported for ^{93}Sr were identified through β-decay experimental

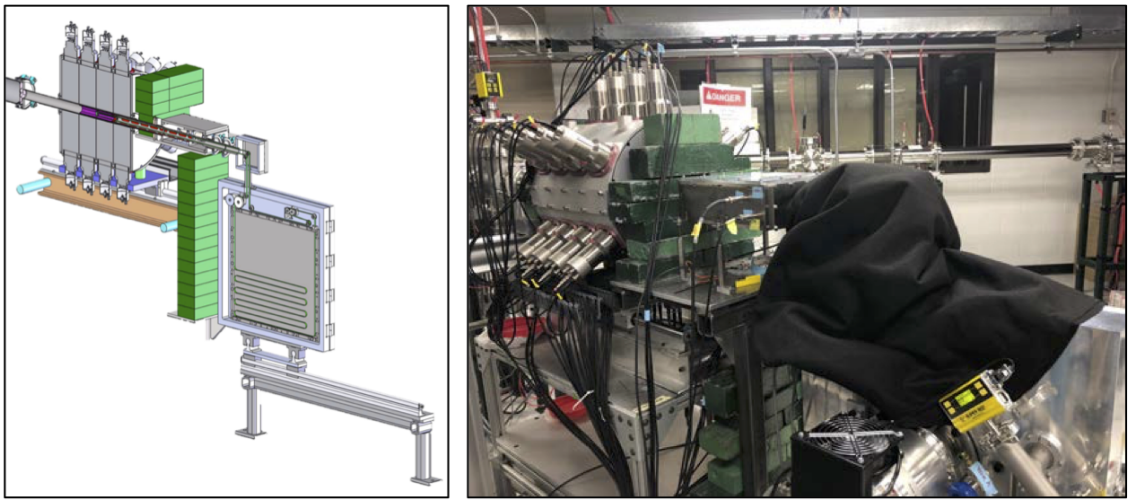


Figure 3.2: Experimental setup. (*Left*) Schematic of SuN and the Tape station for Active Nuclei (SunTAN). (*Right*) Experimental setup of SuN, fiber detector, and tape station (covered in blackout fabric) installed in the low-energy experiment area.

measurements: $\beta - \gamma$ coincidence and $\gamma - \gamma$ coincidence [23]. The remaining levels were identified by measurements of the spontaneous fission of ^{252}Cf [23]. Figure 3.3 illustrates the first 17 levels accessed by β decay of a complete level scheme (20 levels $\approx$ 2.20 MeV). A "complete level scheme" refers to the excitation energy at which the number of experimentally identified levels, i.e., the experimental nuclear level density, no longer increases with excitation energy.

As direct measurement of the neutron-capture reaction rate for ^{93}Sr is inaccessible, an indirect method is via an alternative path way (see Fig. 3.4): the β decay of ^{93}Rb to form the compound ^{93}Sr nucleus, whereby β decay populates highly-excited states in ^{93}Sr, resulting in emitted γ-rays which are measured and subsequently analyzed to extract statistical nuclear properties and to determine the neutron-capture reaction rate. While β decay presents an advantage towards accessing statistical decays, and thus average properties of the nucleus, in the quasi-continuum, the individual levels and order of individual γ rays in a cascade become harder to resolve. When γ-ray energies are high, or if many final states are available, high resolution semiconductor Ge detectors with moderate energy efficiency miss significant γ-ray intensities, referred to as the "Pandemonium effect" by Hardy *et al.* [78]. The Pandemonium effect predicts that for nuclei with complex β-decay schemes (i.e., high Q-value and therefore high nuclear level density), the β-decay feeding intensities obtained using high-resolution detectors are doubtful [78]. G .D. Alkhazov *et al.* suggested the use of total absorption (γ-)spectroscopy (TAS, or TAGS) to address the concern of missing γ-intensities [79]. Their work investigated 40 nuclides through the TAS technique and demonstrated that, with an exception for long-lived isotopes, β-decay feeding intensities measured using high-resolution

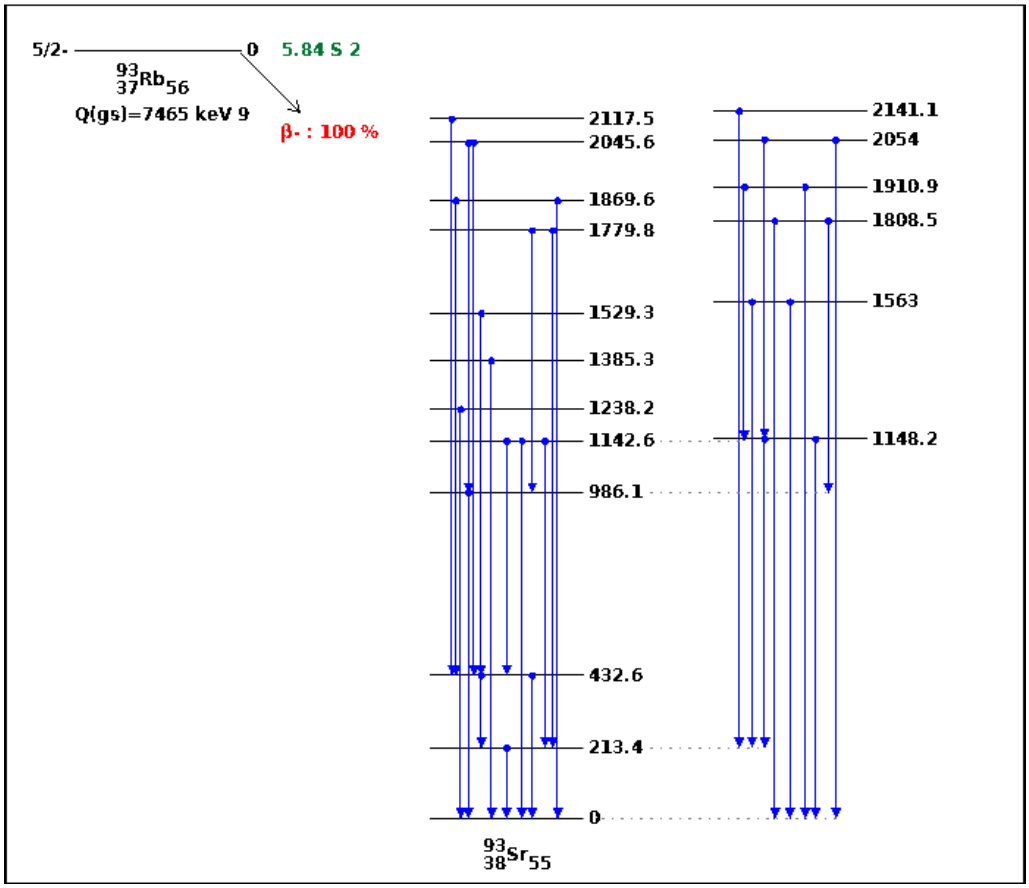


Figure 3.3: The level scheme of ^{93}Sr plotting the first few levels in a complete level scheme, where the number of level continues to increase with increasing excitation energy.

detectors are incorrect [79].

In this work, the β-Oslo Method, discussed in detail in Chapter 4, is used to extract statistical nuclear properties from TAS data. The segmented large-volume SuN detector measures individual γ's emitted from a single cascade which can be summed to determine the excitation energy corresponding to the β-decay populated levels. In addition to identifying the initial excitation energy through the TAS technique, room background was removed by the implementation of a fiberoptic barrel-shaped β-particle detector (henceforth referred to as the fiber detector) to detect electrons from β decay of ^{93}Rb (and consequently, from ^{93}Sr) in coincidence with the subsequent γ rays in SuN. In software, the $\beta-\gamma$ coincidence from the β decay of ^{93}Rb were separated from β decay of ^{93}Sr by taking advantage of the separation in half-lives, as discussed in Section 3.3.1.

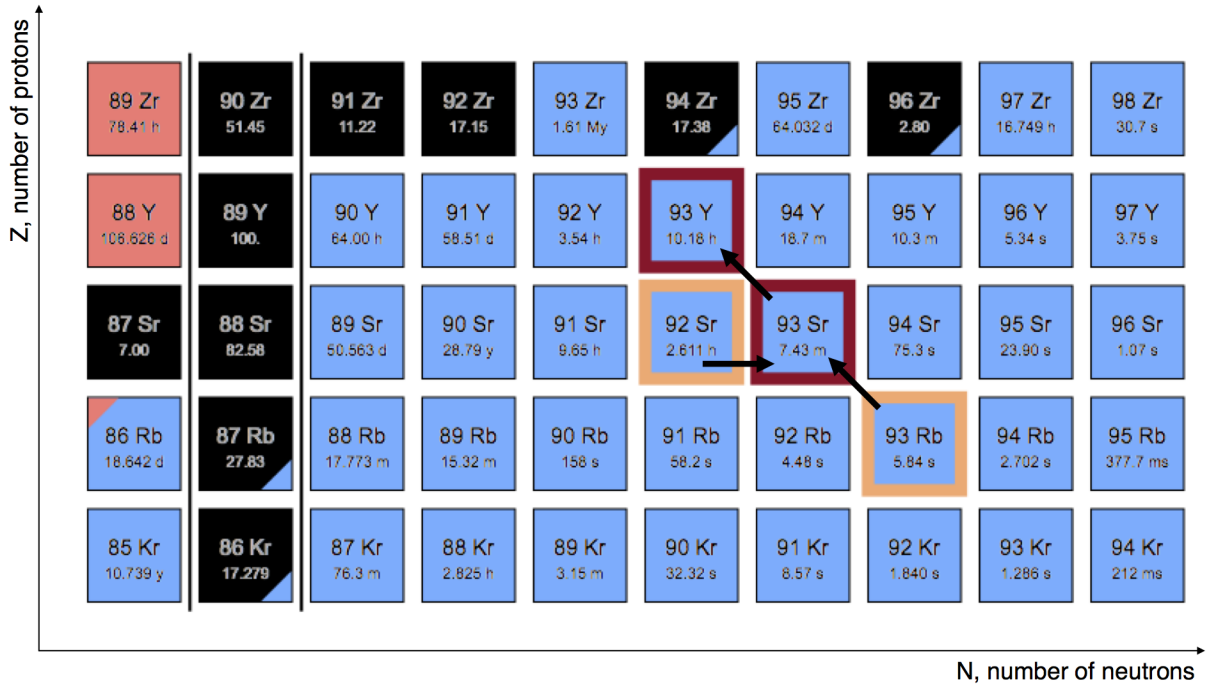
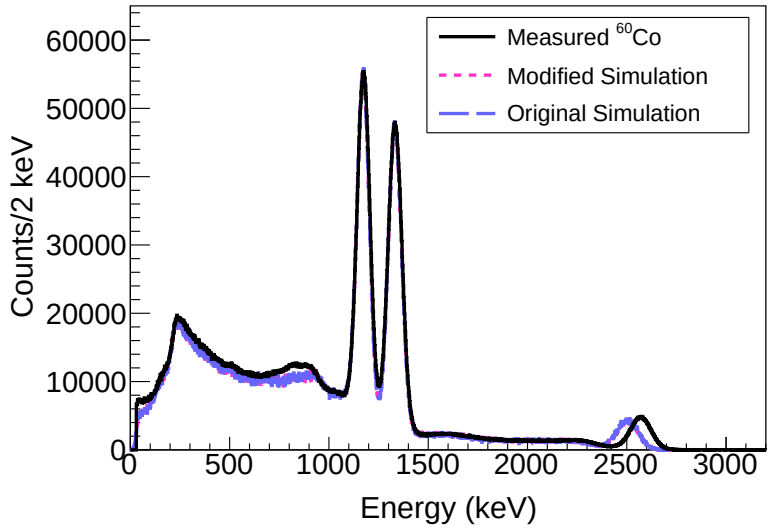


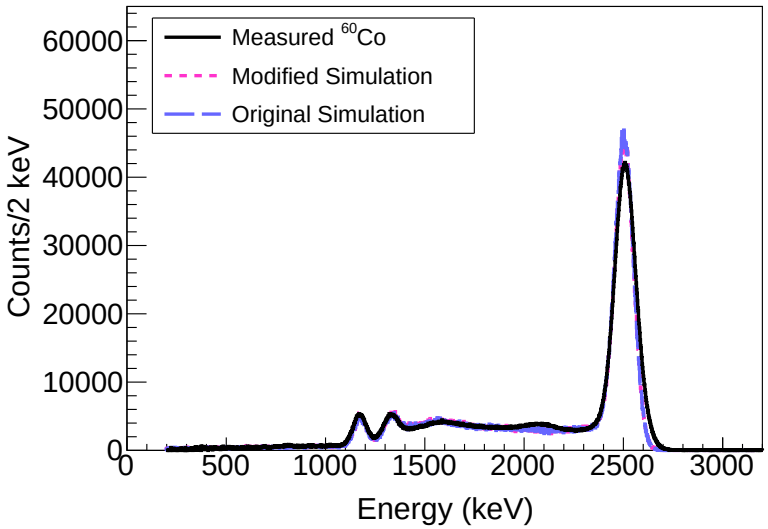
Figure 3.4: Chart of the nuclides in the A = 93 mass region. The direct measurement of the neutron-capture reaction of ^{92}Sr(n,γ) is inaccessible. Alternatively, the compound nucleus ^{93}Sr can also be formed by the β decay of ^{93}Rb. ^{93}Sr formed through β decay itself subsequently decays, which produces a decay daughter that is considered a contaminant in the experimental data.

3.2.2 Summing NaI(Tl) Detector (SuN)

The Summing NaI(Tl) detector (SuN) is a cylindrical total absorption spectrometer (40.64 cm in diameter, 40.64 cm in length) with a 4.57 cm diameter borehole along its axis as illustrated in Fig. 3.6 [74]. The SuN detector is composed of two top and bottom components, each consisting of four optically-separated segments of NaI(Tl) crystals individually read out by three photomultiplier tubes (PMTs). SuN exhibits the combined properties of a large summing efficiency and an acceptable energy resolution, and is thus well suited for TAS experiments analyzed using the β-Oslo Method [74]. The resolution depends not only on energy, but also on the distance from the center of the detector, and therefore varies between the segments of SuN. The average resolution is 6.1(2)% for the 662 keV ^{137}Cs γ ray. Furthermore, the summing efficiency is dependent on multiple factors including distance, the sum-peak energy (event-by-event sum of signals from individual segments), and the average multiplicity $\langle M \rangle$ (the number of sequential γ's de-exciting the nucleus to the ground state). For instance, the summing efficiency is 85(2)% for ^{137}Cs ($\langle M \rangle = 1$) and 65(2)% ($\langle M \rangle = 2$) for



(a) Sum-of-Segments Spectra



(b) Total Absorption Spectra

Figure 3.5: Comparison of background subtracted experimental sum-of-segments spectrum spectrum (top) for ^{60}Co to modified and original simulated spectra. Comparison of background subtracted experimental total absorption spectrum spectrum (bottom) for ^{60}Co to modified and original simulated spectra. The modified simulation includes the fiber detector placed at the center of SuN's borehole.

^{60}Co. Figure 3.5 shows a comparison between experimental spectra for ^{60}Co and simulated spectra. The modified simulation is includes the fiber detector and film holder placed at the center of SuN's borehole. These simulations are quite similar due to the absence of a β-γ coincidence. As ^{60}Co is a sealed source, the electrons were not detected by the fiber detector, and thus the simulation is representative of solely γ-detected events. This illustrates that the additional material of the fiber detector and film holder are negligible. The SuN detector was commissioned using the well-known ^{27}Al(p,γ)^{28}Si resonances in the proton energy range of 2-4 MeV [74]. As an illustration, the experimentally-obtained resonance at $E_p = 2517$ keV was compared to the GEANT4 simulation using the decay scheme of ^{28}Si. Figure 3.7 from Reference [74] plots the simulated summing efficiency (ϵ_Σ) as a function of the number of segments that "fired" along with the experimental results for the 2517 keV resonance and a linear fit to the simulated values. For high energy sum-peaks of approximately 14 MeV, the summing efficiency is 21.1(2)%; however, for the case of ^{93}Sr where the sum-peak energy ranges from 200-7500 keV and $\langle M \rangle$=2-4, the expected summing efficiency is a minimum of 25%.

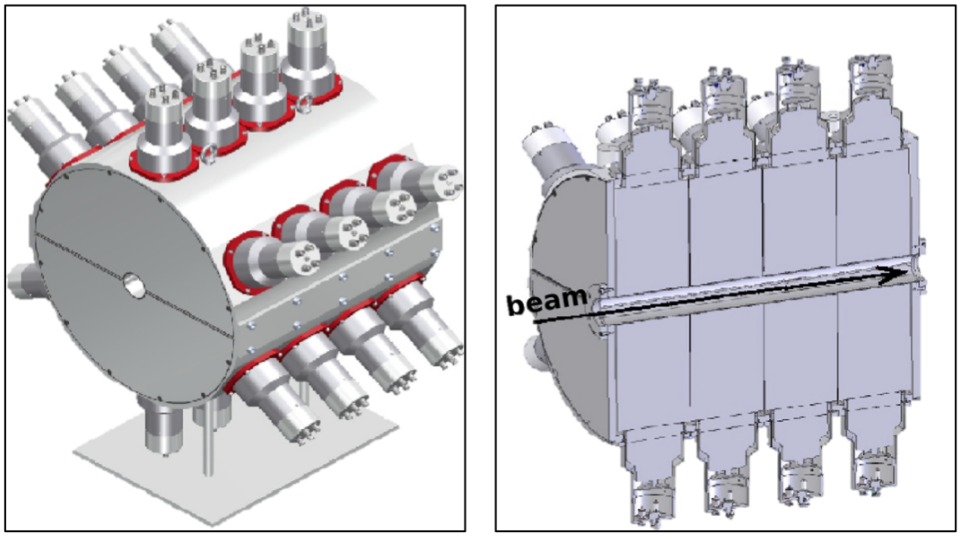


Figure 3.6: The Summing NaI(Tl) detector (SuN). (*Left*) Schematic and (*right*) cross-section along beam axial line. [74]

3.2.3 SuN Tape Transport of Active Nuclei (SuNTAN)

The first TAS experiment performed using SuN and analyzed using the β-Oslo Method was the β-decay of ^{76}Ga to determine the cross section of ^{75}Ge(n,γ)^{76}Ge [10]. From this initial experiment, nuclei approaching the neutron-drip line were investigated using the β-Oslo Method. While ^{76}Ge is a stable isotope, ^{93}Sr has a half-life of 7.43(3) m resulting in the

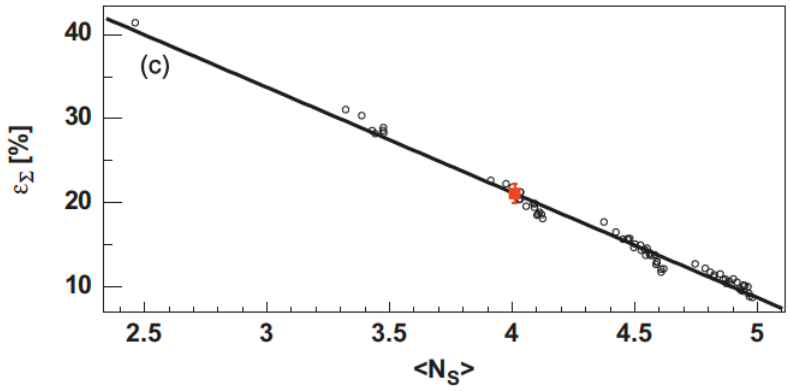


Figure 3.7: Simulated summing efficiency (open circles) plotted as a function of number of segments that "fired" $\langle N_s \rangle$ and fitted with a linear function (solid line) along with experimental results (red data point) from Reference [74].

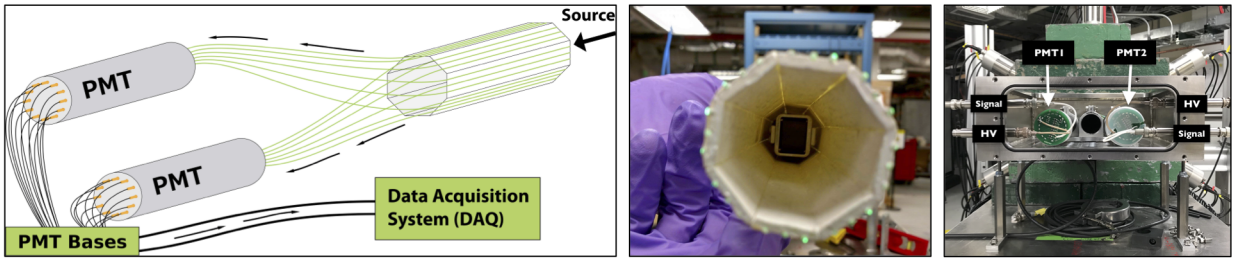


Figure 3.8: Fiber detector with PMT components. (*Left*) Schematic of fiber detector with attached fiberoptic cables connects to two PMTs. (*Center*) Cross sectional view in-line with beam axis of fiber detector, showing film (9-track tape) holder placed in the center of the fiber detector. (*Right*) Rear-view of the two PMTs located outside the SuN detector setup in a stainless steel PMT chamber.

decay daughter ^{93}Y that also produces β-delay γ's. The activity of ^{93}Sr and ^{93}Y is a form of contamination in the experimental results. By utilizing the TAS technique, excitation energies were measured in addition to the individual γ-ray energies, while β decays were identified through $\beta - \gamma$ coincidences measured with SuN plus the fiber detector. The decay daughter contamination was minimized using a tape station setup, where a 9-track tape placed at the center of the detector setup was circulated through the setup, replacing the exposed portion of the tape which accumulated activity from decay daughters with new tape, in-line with the beam of ^{93}Rb. The challenge of reducing decay daughter contamination was balanced with the analysis requirement of high statistics, a required condition for employing the β-Oslo Method. These concerns are addressed in Section 3.3; however, characteristics of

the fiber detector are first discussed in the following section.

Fiber Detector

In addition to SuN, a fiber detector is placed within the beam pipe (i.e., inserted into the borehole of SuN), which surrounds the implantation site at the center of SuN. The fiber detector, pictured in Fig. 3.8, is a 20 cm long and 3 mm thick octagonal sheath of plastic material with four scintillating fibers on each side. Figure 3.8 illustrates the initial iteration of the fiber detector which was developed, consisting of only three optical fibers per side. The plastic material of the barrel base is composed of polyvinyltouene (BC_4O_8) and the fiberoptics are composed of polystyrene. The left-hand side of Fig. 3.8 depicts the optical fibers which extend down the length of the plastic sheath and attach to two PMT's with alternating fibers to either PMT1 or PMT2. The right-hand side of Fig. 3.8 depicts the downstream end of SuN which includes the PMT Chamber housing, comprising these two PMTs, as well as a metal tube which holds the fiber detector inserted into the beam pipe within the borehole of SuN. The PMT Chamber is covered with a back plate which also connects to the Tape and Motor box, as depicted in Fig. 3.2.

Tape Station

The 9-track tape was held in the center of the detector setup by the Tape Holder, which connects to the Fiber Holder and PMT Chamber, as depicted in the center photo of Fig. 3.8. From the back end of the PMT Chamber, the tape is routed to a 90° joint, which feeds the tape through an opening in the top of the Tape and Motor box. The Tape and Motor box is a 64.26×64.26×16 cm stainless steel box consisting of a series of rollers actuated by a motor, the speed of which is controlled through computer software, which controls the tape cycle sequence of implantation time, lag-time before the motor moves, and movement increments. Implantation time is defined as the length of time that the beam is implanted on the exposed portion of the tape in-line with the beam. After a brief delay, the controller signals the motor to rotate the tape by 200 mm. The tape cycle sequence is discussed in more detail in Section 3.3, as it relates to the removal of the decay daughter contamination.

3.3 Data Analysis

Prior to measuring β-γ coincidences, the PMTs of SuN were gain matched and the NaI(Tl) segments of the SuN were calibrated using several calibration sources: ^{60}Co, ^{137}Cs, ^{207}Bi, and ^{241}Am. The 24 PMTs of SuN were first gain matched by adjusting the high voltage applied to each PMT until the 1460.8 keV γ ray from the decay of ^{40}K present in the room background appeared as approximately the same channel number. Then in software, a scaling factor was applied to each PMT such that the 1460.8 keV peak was centered precisely as the same channel. The energy spectra of the PMTs were aligned to the center PMT of the second top segment of SuN to obtain the final scaling factors listed in Table C.1. The PMTs of the

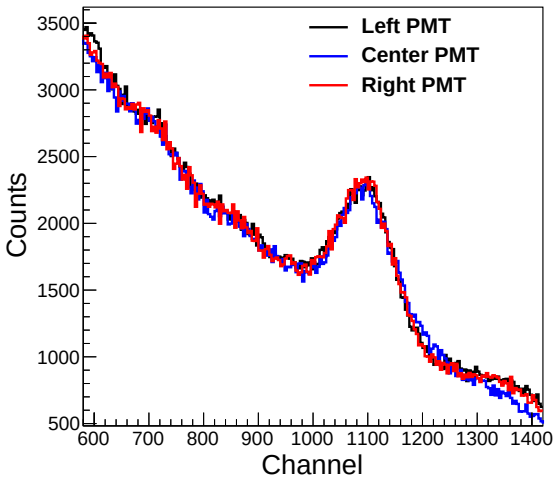


Figure 3.9: Top first segment of SuN (T1) gain matched background spectrum. Individual PMTs of segment scaled such that 1460.8 keV peak was centered precisely as the same channel. The PMTs of the remaining seven segments of SuN were similarly gain matched, resulting in similar centered 1460.8 keV peaks.

top first segment, gain matched using the background peak, are shown in Fig. 3.9, which is representative of the peak shape obtained for the remaining PMTs.

Once the PMTs were gain matched, the three PMTs of each segment were summed to determine the energy deposited in the segment. The eight segments of SuN were calibrated using the sources listed in Table C.2 such that the individual γ-ray peaks corresponded to the correct energy. The individual γ-ray lines of each source measurement were fit with a Gaussian to determine the centroid corresponding to the channel number and standard deviation of the peak. In this thesis, a linear function in the form of $E = Ax + B$ and a quadratic function in the form of $E = Ax^2 + Bx + C$ were examined to achieve the best calibration. The quadratic function approach resulted in an overfitting of the channel number to γ-ray energy. Figure 3.10 shows the linear calibration of each SuN segment. Finally, the individual segments of SuN were summed to obtain the excitation energy.

The experiment took place over the course of one week, during which the PMT response may have possibly drifted. As part of the experiment, the 1460.8 keV background peak was surveyed before, during, and shortly after the end of the experiment to evaluate changes in the gain matching. Both the average and maximum changes in the scaling factor were less than one percent, and as a result a constant gain matching was applied to the experimental energy spectra. In addition, following the experiment, ^{60}Co and ^{137}Cs sources were also measured and no significant drift was observed in the PMTs. A single set of scaling factors

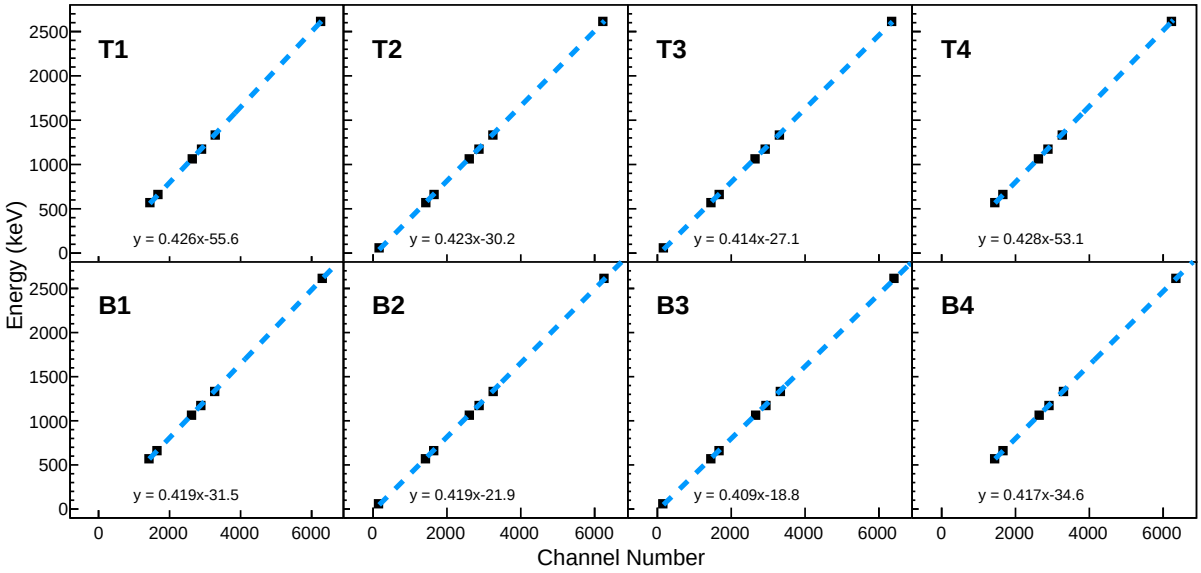


Figure 3.10: Calibration for each segment of SuN. Location of each segment is indicated as the top "T" or bottom "B" half of SuN, and the segment is indicated by the number.

and calibration parameters were therefore used for the whole of the experiment. Figure 3.11 shows no drift in the 1460.8 keV peak.

The fiber detector used to measure β particles was a 20 cm long, 3mm thick octagonal plastic sheath attached through optical fibers to two PMTs external to SuN. The fiber detector was fabricated by the research group of Dr. Paul de Young at Hope College. In this thesis, the fiber detector was used only to measure β-γ coincidence and not the energy of the β particle. In software, the two PMTs of the fiber detector were placed in coincidence to each other in order to eliminate false coincidences driven by noise from the PMTs. While the fiber detector was used to identify β-decay events, β-γ coincidences were not used to distinguish between the β decay of ^{93}Rb and ^{93}Sr due to the poor energy resolution.

3.3.1 ^{93}Sr Production

The radioactive isotope beam of ^{93}Rb has a half-life of 5.84 (2) s and predominantly populates both the ground state ($I_\beta = 35\%$) and highly excited states (states between 3.8-4.00 MeV, $I_\beta = 33.11\%$) in ^{93}Sr. In addition, the decay daughter ^{93}Sr is also unstable with a half-life of 7.43 (3) m and produces the decay grand-daughter ^{93}Y. This radioactive decay chain can be expressed in terms of the decay constants: $\lambda_1 = \ln(2)/t_{1/2}(^{93}\text{Rb})$ and $\lambda_2 = \ln(2)/t_{1/2}(^{93}\text{Sr})$

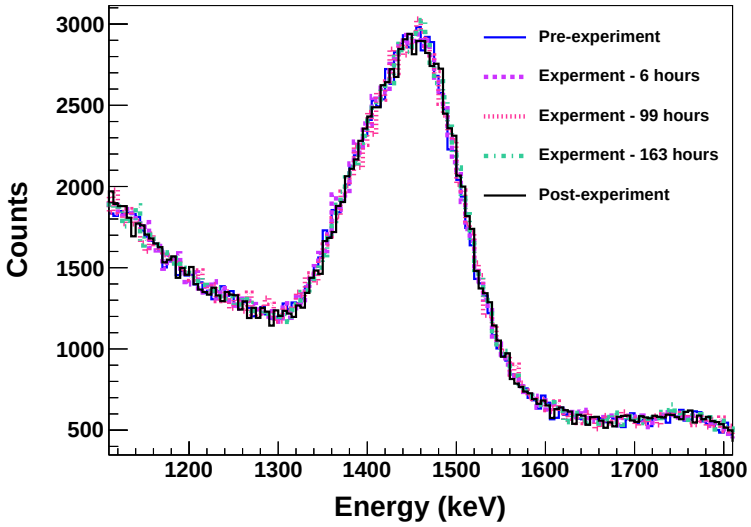


Figure 3.11: ^{40}K background spectra of the first top segment of SuN monitored before, during (6 hour, 99 hours, and 163 hours into the experiment), and after experimental runs measuring the decay of ^{93}Rb. The energy spectra of the remaining SuN segments result in similarly shaped peaks at 1460.8 keV.

such that simultaneous production and decay of β-decaying nuclei at time t is

$$\frac{dN_1(t)}{dt} = R - \lambda_1 N_1(t) \tag{3.1}$$

$$\frac{dN_2(t)}{dt} = \lambda_1 N_1(t) - \lambda_2 N_2(t) \tag{3.2}$$

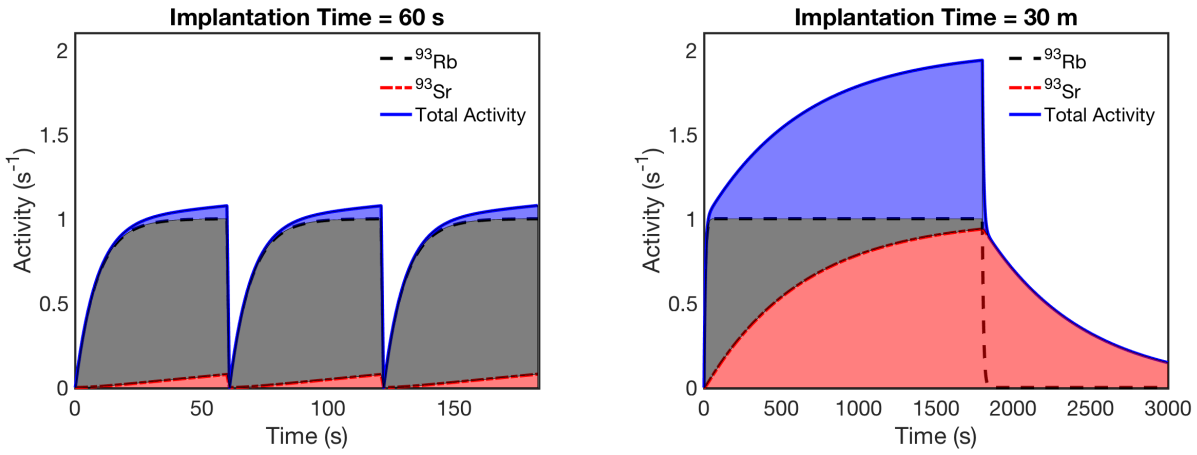
where $N_1(t)$ and $N_2(t)$ are the number of parent nuclei ^{93}Rb and daughter nuclei ^{93}Sr. The production rate R is an implantation rate of approximately 12 pps. In addition, the initial number of parent and daughter nuclei is zero, i.e., $N_1(0) = 0$ and $N_2(0) = 0$. The decay equation for the number of β-decaying ^{93}Rb nuclei is

$$N_1(t) = \frac{R}{\lambda_1}\left(1 - e^{-\lambda t}\right) \tag{3.3}$$

and consequently, the decay equation for the number of decay daughter nuclei is

$$N_2(t) = R\left(\frac{1}{\lambda_2} - \frac{e^{-\lambda_1 t}}{\lambda_2 - \lambda_1}\right) - Re^{-\lambda_2 t}\left(\frac{1}{\lambda_2} - \frac{1}{\lambda_2 - \lambda_1}\right). \tag{3.4}$$

While the maximum β-particle energy emitted from the parent nucleus is more than 3 MeV greater than those of β particles emitted by the daughter nucleus, the SuNTAN system is



(a) Production Run (b) Daughter Run

Figure 3.12: Radionuclides produced by the β-decay of ^{93}Rb. The assumed radioactive isotopes beam rate is 1 pps. *(a)* The production run includes three cycles of 60 s beam on, followed by motor-actuated placement of new tape at the center of the detector setup. The sum of the area beneath the ^{93}Rb (black) and ^{93}Sr (red) decay curves is equivalent to the area beneath the blue curve. *(b)* The daughter run includes one cycle of 30 m beam on followed by 20 m beam off where the decay events are counted.

not able to discriminate between events in the decay chain. However, by using the difference between half-lives, the ^{93}Rb $\rightarrow$ ^{93}Sr and ^{93}Sr $\rightarrow$ ^{93}Y decays were identified in this experiment with SuNTAN. The coupled SuN and fiber detector system is used to identify β-γ coincidences as well as to detect the sum activity of parent and daughter nuclei:

$$\begin{aligned} A_{tot}(t) &= A_1(t) + A_2(t) \\ &= \lambda_1 N_1(t) + \lambda_2 N_2(t) \\ &= R\left(1 - e^{-\lambda t}\right) + \lambda_2 R\left(\frac{1}{\lambda_2} - \frac{e^{-\lambda_1 t}}{\lambda_2 - \lambda_1}\right) - \lambda_2 R e^{-\lambda_2 t}\left(\frac{1}{\lambda_2} - \frac{1}{\lambda_2 - \lambda_1}\right). \end{aligned} \tag{3.5}$$

In this experiment, cycles of implantation and removal were used to identify decay events by exploiting the tape station to manage the activity of the decay daughter, i.e., the level of contamination in the measurement.

The theoretical activity of the decay chain as a function of time, assuming negligible activity from the β-decay of ^{93}Y, is given by Eq. 3.5 and is illustrated in Fig. 3.12. The individual theoretical activities of the parent and daughter nuclei shown in Fig. 3.12a represent an implantation time (and measuring time) of 60 s, which in this experiment is followed by a rapid removal of tape in-line with the beam and replacement with a clean portion of tape for another 60 s implantation period. These 60 s implantation cycles, which will henceforth be referred to as *production runs*, were implemented in the experiment to obtain a low level

of contamination. In addition, the Tape and Motor Box experienced jamming problems for cycles of 30 s and lower. The level of contamination was theoretically calculated as the ratio of the number of decay daughter nuclei to the sum of parent and daughter nuclei expressed as

$$C = \frac{\int_0^T A_2(t)dt}{\int_0^T A_{tot}(t)dt}, \tag{3.6}$$

where time, T, is the implantation time. In the case of $T = 60$ s, the contamination in the production run is $C = 3.85\%$. If the implantation time was increased by a factor of 10, the number of ^{93}Rb would increase by 14%, and conversely, the level of contamination would increase by a factor of six. A 60 s implantation time was selected to balance the need for high statistics and low contamination.

While the contamination level is low, an effort was exerted to remove β decays of ^{93}Sr from the experimental measurements by using the known half life to identify $\beta-\gamma$ coincidence of ^{93}Sr$\rightarrow^{93}$Y. A useful technique to exploit the difference between $t_{1/2}(^{93}\text{Rb})$ and $t_{1/2}(^{93}\text{Sr})$ is to utilize a longer implantation time, such that the total activity approaches a near constant rate, and a longer removal time, such that the activity of ^{93}Rb approaches zero, and thus only the activity of ^{93}Sr is observed. These extended implantation cycles, which will henceforth be referred to as *daughter runs*, consist of a 30 m period of radionuclide implantation on tape centered in the detector setup followed by 20 m of the radioactive isotope beam turned off. Figure 3.12b illustrates the number of ^{93}Rb and ^{93}Sr nuclei during beam on and beam off. After 30 m of beam on, the number of ^{93}Rb and ^{93}Sr nuclei as a function of time, τ, is described by the following decay equations:

$$N_1(\tau) = N_1(t = 30\text{ m})e^{-\lambda_1\tau}, \tag{3.7}$$

$$N_2(\tau) = \frac{\lambda_1 N_1(t = 30\text{ m})}{\lambda_2 - \lambda_1}(e^{-\lambda_1 t} - e^{-\lambda_2 t}) + N_2(t = 30\text{ m})e^{-\lambda_2 t} \tag{3.8}$$

where $N_1(t = 30\text{ m}) = R/\lambda_1$ and $N_2(t = 30\text{ m}) \approx R/\lambda_2$ are the number of ^{93}Rb and ^{93}Sr nuclei at the moment the beam is turned off. Once the beam is off, the activity of ^{93}Rb approaches less than less than 0.1% within 10 half-lives, or one minute, and thus a minute after the beam is off ($\tau' = \tau + 60$ s), the decay equation for the number of ^{93}Sr simply becomes

$$N_2(\tau') = N_2' e^{-\lambda_2\tau'}, \tag{3.9}$$

where N_2' is the number of ^{93}Sr nuclei one minute after the beam is off. The theoretical activities of the parent and daughter nuclei during a daughter run are shown in Fig. 3.12.

In the analysis of the data collected from this experiment, Eq. 3.5 was used to fit the events histogrammed as a function of time when the beam was on, while Eq. 3.9 was used to fit the events recorded one minute after the beam was turned off. For 12 daughter cycles, or 10 hours, β-γ coincidences were measured and analyzed using the described procedure. The fit of the experimental data using Eq. 3.5 (beam on) and Eq. 3.9 (beam off) is shown in Fig. 3.13, which also includes a constant background activity. Background radiation was

measured before, during, and after the experiment shown in Fig. 3.14. While measuring background activity before and after the experiment, the motor actuated tape box was not operated in contrast to the measurement taken during the experiment. The difference in measured background activity between during (0.79±0.02 s^{-1}) and before or after (0.68±0.01 s^{-1} and 0.71±0.01 s^{-1}, respectively) was statistically significant, i.e., greater than three standard deviations (SD), while the difference between background activity before and after was approximately two SD. For beam off, the experimental data from 12 daughter cycles were fit using Eq. 3.9 plus a fit parameter representing the background activity, which resulted in a reduced-χ^2 of 1.06 and a background activity of 0.68±0.04 s^{-1}. The differences between the background activity obtained from the fit and background activity measured before, during, and after the experiment are statistical insignificant, i.e., 0.1, 2.4, and 0.6 SD, respectively. As the difference was statistically insignificant, the background activity measured during the experiment was used as an upper limit in the following fit of the daughter cycles when the beam was on.

The results of the fit for beam on produce a reduced-χ^2 of 1.11 and a beam rate of 12.01±0.02 s^{-1}; whereas, for the fit for beam off, the background activity was not a fit parameter but instead kept fixed at 0.79 s^{-1}, i.e., the background activity measured during the experiment. If the background activity was also treated as a fit parameter, the fit of the data during beam on also resulted in a reduced-χ^2 of 1.11, and the corresponding beam rate was 11.87±0.10 s^{-1} and background activity was 1.03±0.16 s^{-1}. In addition to equivalent goodness of fit for both procedures, the difference in calculated beam of each procedure is 1.2 SD. The difference between the fit-determined background activity for beam on compared to background activity during the experiment is 1.5 SD. If the background activity obtained from the fit of beam off data is compared to the measured background activity from during the experiment, the difference is 2.4 SD. Both approaches to fitting the experimental data for beam on are not statistically different.

While the β decay of ^{93}Rb will predominately populate high excitation energy states, the observed background radiation resulted in low excitation energy populated states and low-energy γ rays shown in Fig. 3.15. In the analysis using the β-Oslo Method, as discussed in Chapter 5, excitation energy and γ-ray energy thresholds were implemented, and thus the influence of the low background activity was minimized such that of the measured background excitation and γ-ray energies were 6% and 14%, respectively, are within the bounds of the analysis region. In addition to limiting the impact of background radiation through energy thresholds, the background radiation is simultaneously removed when subtracting the contamination from the decay daughter from the β-gated γ-ray spectra and TAS spectrum. The energy spectra of the contamination were obtained by fitting the daughter runs for beam off, and thus, time gates for ^{93}Sr γ-ray energies and excitation energies were obtained. The time-gated γ-ray and TAS spectra of the decay daughter are subtracted from the β-gated data of production runs.

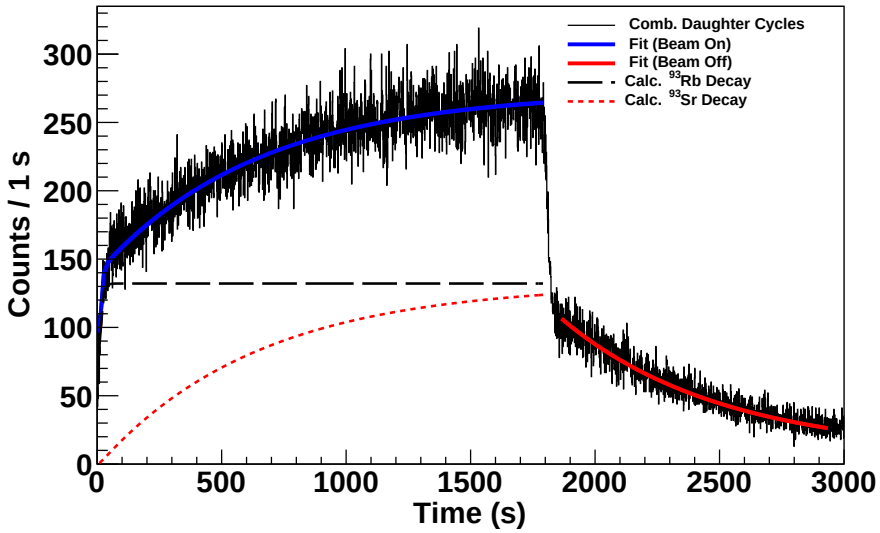


Figure 3.13: The activity measured from two daughter runs for a total measuring time of 10 hours, or 12 cycles of 50 minutes, is plotted along with fits for when beam is on and off. For beam on, the activity was fit using Eq. 3.5 and a background activity of 0.79 s^{-1}. For beam off, the activity was fit using Eq. 3.9 plus a fit parameter representing the background activity, which was applied one minute after the beam is turned off. The individual decays of ^{93}Rb and ^{93}Sr are calculated using the implantation rate (12.01$\pm$0.02 s^{-1}) obtained from the fit (beam on).

3.3.2 Decay Products as Contamination

In software, β-γ coincidence spectra were obtained from decay events, identified by the coincidence of signals when a β particle and γ rays were detected. The total coincidence data includes both the decay of ^{93}Rb and ^{93}Sr, which is considered a decay daughter contaminant. However, the activity of the daughter was isolated by adding a timing requirement between the ^{93}Rb activity approaching zero and the remaining ^{93}Sr activity, producing γ-ray energy and TAS spectra referred to as time-gated spectra. Time-gated spectra of the decay daughter were subtracted from the total coincidence spectra measured during production runs.

The production runs were analyzed in a similar manner as the daughter runs to confirm the production and decay behavior of the radionuclides as well as to investigate sources of possible contamination from background or from impurities in the radioactive isotope beam. The production run shown in Fig. 3.16 illustrates that the radionuclides follow the expected theoretical behavior expressed by Eq. 3.5, that the activity of ^{93}Rb reaches secular equilibrium within one minute of beam on. The cumulative counts recorded over 50 cycles

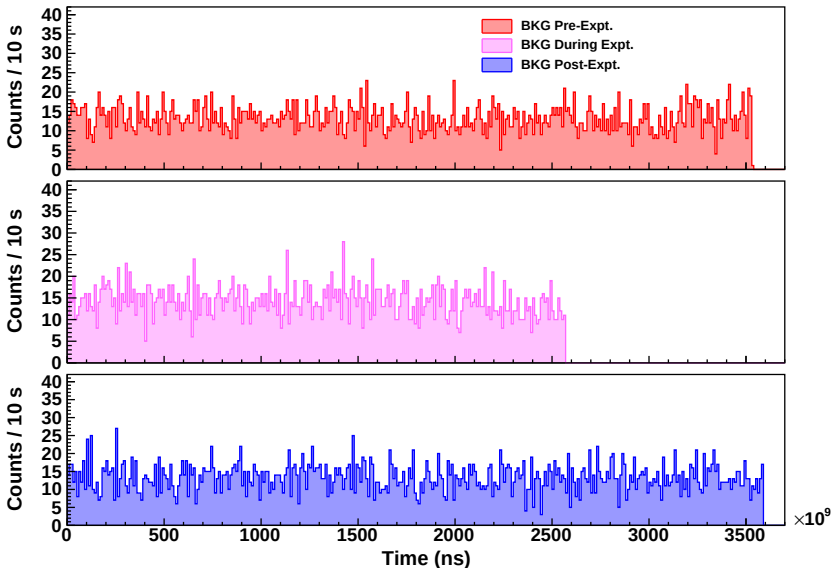


Figure 3.14: The activity of background radiation was measured before, during and after the experiment, and in software, β-gates were utilized to determine the β-γ coincidence. The measured background activity before, during, and after the experiment: 0.68±0.01 s^{-1}, 0.79±0.02 s^{-1}, and 0.71±0.01 s^{-1}, respectively. The difference between the background activity during the experiment and activity before or after is statistically significant. See text for description of difference between background measurements.

were fit using Eq. 3.5 along with a constant background, resulting in a reduced-χ^2 of 0.89 and an implantation rate of 11.36±0.07 pps, which is statistically different from the beam rate obtained from the analysis of the daughter runs. However, investigating the entire data set of 101 production runs resulted in an average beam rate compared to the analysis of the daughter runs that is not statistically different.

Contamination from the β decay of ^{93}Sr was subtracted from the production runs. The contamination was characterized using the β-γ coincidence events obtained from ten daughter cycles when beam was off (i.e., cumulative events of two hours). Daughter TAS and γ-ray spectra were normalized to area of the data collected from productions runs:

$$\mathscr{N} = \frac{C \times \int_{E_{th}}^{E_f} \int_{E_{th}}^{E_f} \hat{M} dE_x E_\gamma}{\int_{E_{th}}^{E_f} \int_{E_{th}}^{E_f} \hat{D} dE_x E_\gamma}, \tag{3.10}$$

where C is the contamination from Eq. 3.6, which is 4% for 60 s implantation time periods. The γ-ray energies and excitation energies measured for β-γ coincidence events are expressed by a 2-D histogram of excitation energy (i.e., TAS spectrum) versus γ-ray energy spectra

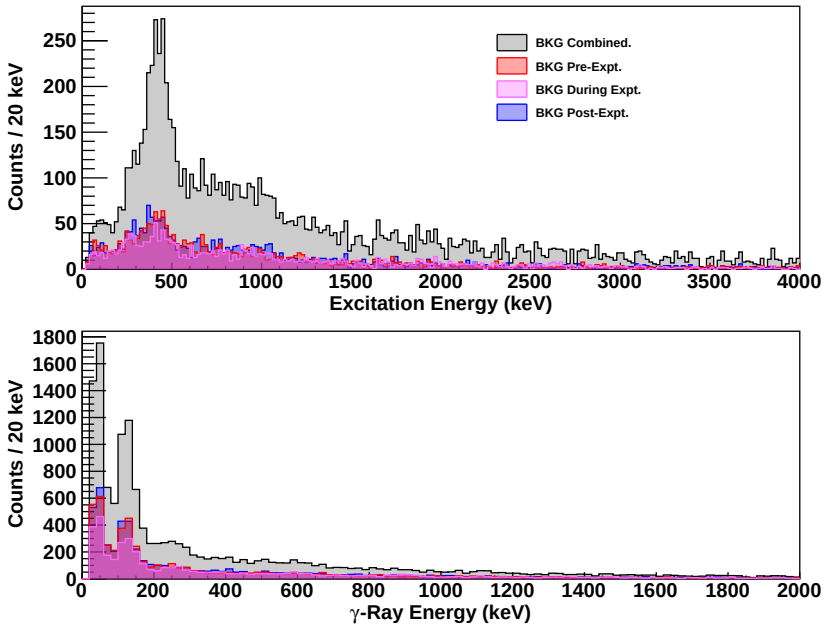
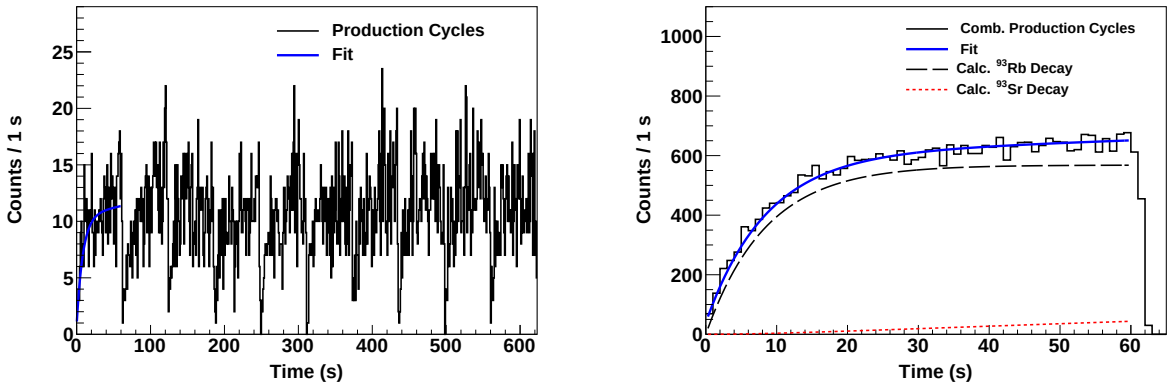


Figure 3.15: The TAS (top) and γ-ray (bottom) spectra of the background radiation were obtained from measurements before, during, and after the experiment.

for production runs ($\hat{M}$) and daughter runs ($\hat{D}$). The matrices are integrated as a function of energy from an energy threshold, E_{th}, to a final energy, E_f. The normalization factor $\mathcal{N}$ is applied to $\hat{D}$, which then is subtracted from $\hat{M}$, and thus the remainder of events are from the β decay of ^{93}Rb. A comparison between the total β-gated events and the contamination-subtracted events is shown in Fig. 3.17 and 3.18.

The TAS spectra in Fig. 3.17 illustrates the comparison between experimental spectra of the raw β-γ coincidence data, the contamination-subtracted data, and the time-gated contamination data. As the β-decay of ^{93}Sr has a low Q-value 4.141(12) MeV [23], excited states in ^{93}Y are populated at or below the Q-value, which is observed in the experimental spectrum labeled decay daughter in Fig. 3.17. The normalized decay daughter spectrum is subtracted from the raw experimental spectra producing the TAS spectrum of the β decay of ^{93}Rb. As expected from the NNDC-reported β-decay intensities (Fig. 2.3), the β decay populated states predominately at approximately 4 MeV. The γ-ray spectra in Fig. 3.18 illustrates the γ rays emitted following the β decay of ^{93}Rb and ^{93}Sr. Similar to the previous observation regarding populated excitation energies, the comparison of γ-ray spectra highlights that the β decay of ^{93}Sr influences measurements at γ-ray energies below 2 MeV. The measured daughter-subtracted TAS and γ-ray spectra construct the so-called 2D β-Oslo matrix shown in Fig. 3.19. This raw matrix of excitation energy on the y-axis and γ-ray energy on the x-axis is analyzed using the β-Oslo Method, where results are discussed in Chapter 5.



(a) Ten cycles of a production run.

(b) Combined cycles of a production run.

Figure 3.16: The activity measured of a production run, which is composed of 57 cycles of beam implantation for one minute followed by immediate removal and replacement of tape in-line with the beam. *(a)* The first 10 minutes of the production run are plotted along with a fit of the first cycle using Eq. 3.5 and a constant background. *(b)* The 57 cycles are combined so as to fit data with high statistics, which resulted in a implantation rate of 11.2 pps and a background of 1.6 s^{-1}. The individual decays of ^{93}Rb and ^{93}Sr are calculated using the implantation rate obtained from the fit.

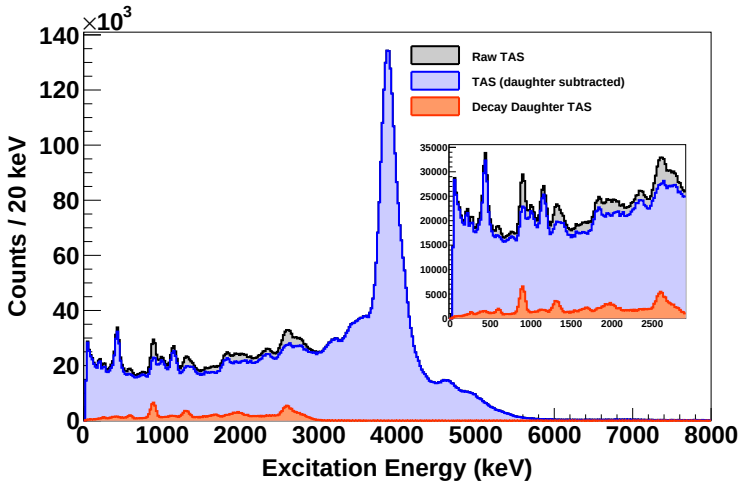


Figure 3.17: Comparison of the raw TAS spectrum to the TAS spectrum of the decay parent ^{93}Rb. Decay daughter ^{93}Sr β-γ coincidence events were subtracted from the total (raw data set) β-γ coincidence events recorded.

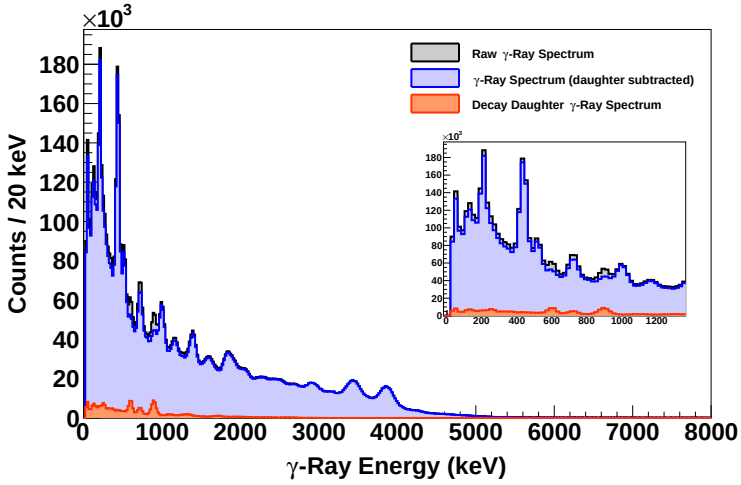


Figure 3.18: Comparison of the raw γ-ray spectrum to the γ-ray spectrum of the decay parent ^{93}Rb. Decay daughter ^{93}Sr β-γ coincidence events were subtracted from the total (raw data set) β-γ coincidence events recorded.

3.4 Response Function for ^{93}Rb$\rightarrow$^{93}Sr Experiment

The initial step in the β-Oslo Method, which is discussed in detail in Chapter 4, is to unfold the γ-ray spectra of the raw matrix shown in Fig. 3.19. A detector response function was developed using GEANT4 [80] to model the interaction of γ rays and electrons with the fiber detector and SuN. The detectors and tape holder were constructed in GEANT4 with the physical and material attributes described Section 3.2. Individual γ rays over an energy range of 200 keV to 7.4 MeV were simulated to measure the response of each NaI segment to γ rays emitted by the β-decay of ^{93}Rb.

The previous GEANT4 simulation utilized a resolution function which characterized the the eight NaI segments of SuN [81, 82]. Modifications to the GEANT4 simulation included the response to electrons emitted from β decay, as well as the construction of the fiber detector and Fiber and Tape Holder. While the modified GEANT4 simulation accurately describes the experimental setup and phenomena of β and γ decay, the modified response function is not statistically different from the original response function, as illustrated by the spectra of varying γ-ray energies shown in Fig. 3.20. In addition, the resolution relative to the response to 1332 keV γ rays is unaltered as shown in Fig. 3.21a. However, a noticeable difference is observed between the efficiency of the original and modified simulations shown in Fig. 3.21b, which is a result of the coincidence gate implemented in the modified GEANT4 simulation requiring detection of both the β particle and the γ ray. Additional elements of the resolution function are the interactions of γ rays with matter that result in the partial or full absorption of the γ-ray energy, such as the probability of measuring the

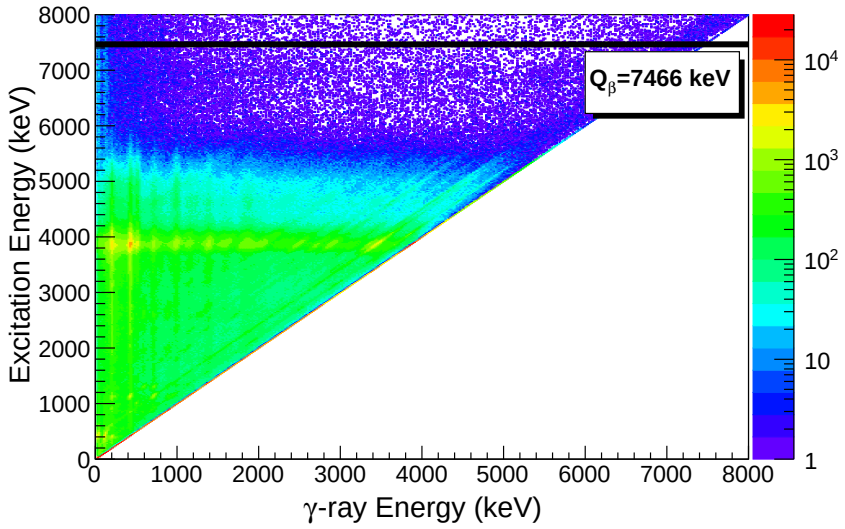
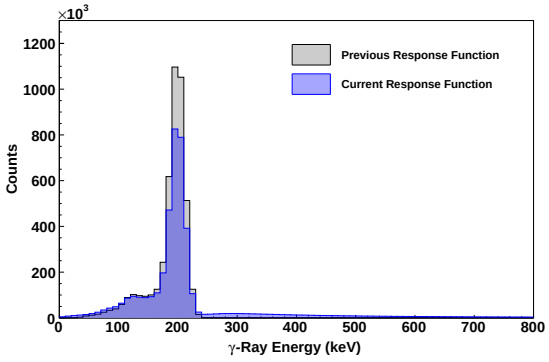
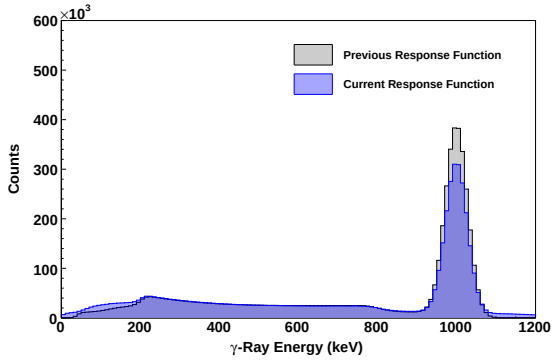


Figure 3.19: Raw 2D β-Oslo matrix for the decay of ^{93}Rb to excited states in ^{93}Sr. The normalized decay daughter β-γ coincidence events have been subtracted from the experimental spectra. The γ-ray energies on the x-axis represent the energy deposited in each of the individual inner NaI segments of SuN. The excitation energies on the y-axis represent the total energy deposited in the SuN detector after the β-decay of ^{93}Rb.

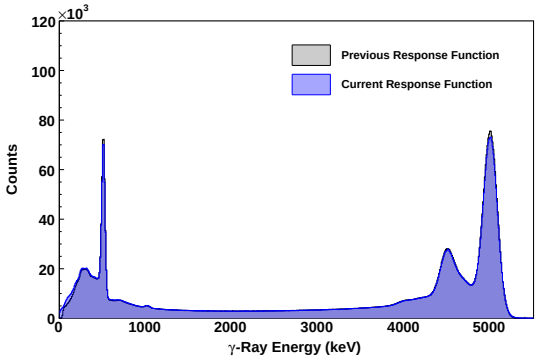
full energy deposition (full energy peak), the escape of a single annihilation photon (single escape peak), the escape of both annihilation photons (double escape peak), the annihilation radiation from pair production within the surrounding material (annihilation peak), and the Compton scattering of incident γ rays with an electron in the surrounding material (Compton Scattering, background). For low energy incident γ rays ($E < 1.6$ MeV), the intensity of the full energy peak is 40-60 %. For high energy incident γ rays, as expected, the probability of other interactions with matter increases, such that Compton scattering and pair production become possible and the intensity of the full energy peak is on average 27% with a standard deviation of 8%. These characteristics of SuN, especially its high detector efficiency for individual γ rays which are subsequently summed to determine the total excitation energy of the populated nuclei, make it a suitable detector for β-Oslo analysis.



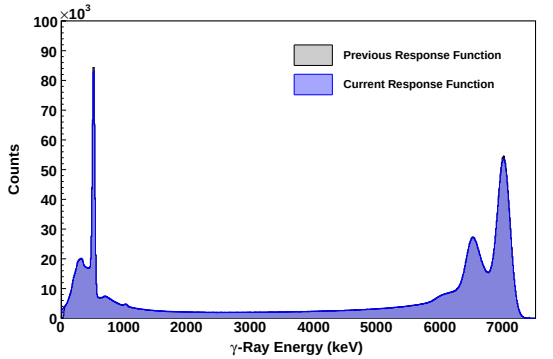
(a) Simulated 200 keV γ-ray spectra



(b) Simulated 1000 keV γ-ray spectra

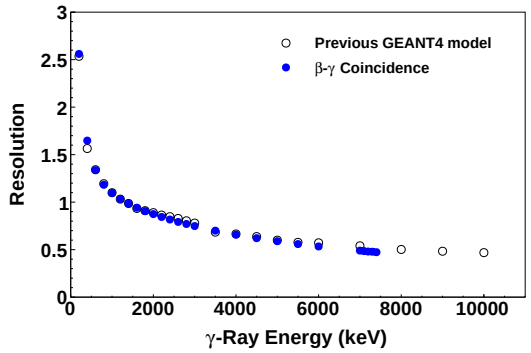


(c) Simulated 5000 keV γ-ray spectra

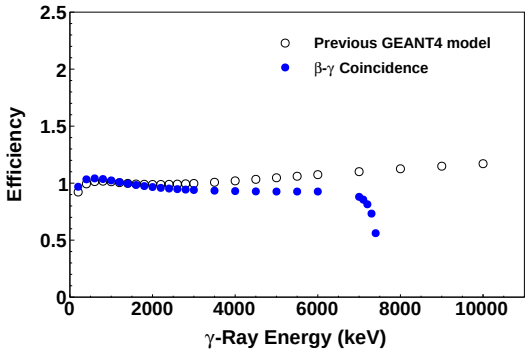


(d) Simulated 7000 keV γ-ray spectra

Figure 3.20: Comparison of original and modified simulation of response to γ rays of varying energies.



(a) Simulated resolution of inner segments of SuN



(b) Simulated efficiency of inner segments of SuN

Figure 3.21: Comparison of the original simulated detector response to γ rays (open circles) and the modified GEANT4 simulation of detecting β-γ coincidence for the decay of ^{93}Rb (Q_β=7466(9) keV [23]) (blue circles). The detection efficiency and the resolution are relative to the response to a 1332 keV γ ray.

Chapter 4

Methodology: β-Oslo Method

The traditional Oslo Method is a set of analytical methods and techniques that is used to extract basic nuclear properties, the nuclear level density (NLD), and the γ-ray strength function (γSF) from γ-ray spectra for a given excitation energy which is accessed by light particle reactions, such as direct reactions (^{3}He, α) and (^{3}He, ^{3}He') [83, 9]. While the traditional Oslo Method is applied to particle-γ coincidence data, the β-Oslo Method is applied to nuclei formed through β decay. The β-Oslo Method was first introduced in Reference [10] as a technique which can be used to determine the neutron capture cross section specifically for short-lived isotopes. In addition to accessing highly excited states near the neutron separation energy by β decay, the β-Oslo Method utilizes total absorption spectroscopy (TAS), rather than the difference between the reaction Q-value and ejectile energy, to determine the excitation energy. The four main steps of the (β-)Oslo Method, described in detail in this chapter, entail:

1. Unfolding of the γ-ray spectra [84],
2. extraction of the first generation of γ-rays [83],
3. extraction of the NLD and γSF,
4. and normalization of the NLD and γSF [9],

4.1 Unfolding the γ-Ray Spectra

Thallium-activated sodium iodide, NaI(Tl), scintillation detectors are used to measure γ rays emitted after an interaction which transfers all or part of the photon energy to an electron in the detector material with a high efficiency. The most significant features of a γ-ray spectrum are: full energy, single escape, double escape, and annihilation peaks, as well as Compton events, which result in complicated detector response functions. These features and the development of a response function are discussed in Chapter 3. To obtain true full energy γ-ray spectra, the observed spectra must be unfolded.

The detector response function $R(E, E_\gamma)$, where E is the energy deposited in the detector, is ideally established for all possible incident γ-ray energies E_γ; however $R(E_x, E_\gamma)$ is measured for only a few monoenergetic γ rays that ranged from 200 keV to the Q_β-value of ^{93}Rb. The large-volume segmented Summing NaI(Tl) detector (SuN), a total absorption spectrometer with a high summing efficiency, is well suited for β-Oslo Method analysis. A detailed discussion of SuN and the detector setup is presented in Chapter 3. Briefly, the detector covers a solid angle of approximately 4π surrounding the sample in the center of the bore hole of SuN. Individually emitted γ rays are measured, and from the sum of simultaneously emitted γ rays the excitation energy is determined. In addition to the full energy of the γ rays deposited in the detector material, the experimental γ-ray spectra includes the Compton continuum as well as the single escape, double escape, and annihilation peaks and random coincidence events.

As the response function was developed from several monoenergetic γ-ray energies, an interpolation procedure was used to develop a continuous function for all energies E_γ [84]. In brief, the interpolation between peak structures is performed by adding a Gaussian distribution at the interpolated peak position with a known detector efficiency and energy resolution. The Compton continuum requires a more complicated treatment, as the Compton edge for each $R(E, E_\gamma)$ depends on its respective full energy peak. Figure 1 of Reference [84] illustrates the treatment of the Compton continuum response functions between the measured response functions c_1 and c_2 as a function of the energy deposited in the detector, E, as a result of the incident γ-ray energy, E_γ, and the scatter angle, θ. The detected γ-ray energy can be expressed as

$$E = E_\gamma - \frac{E_\gamma}{1 + \frac{E_\gamma}{m_e c^2}(1 - \cos(\theta))}, \tag{4.1}$$

where $m_e c^2 = 511$ keV is the rest mass energy of an electron. The unfolding process, presented in the following sections of this chapter, is composed of two primary steps: a folding iterative method followed by a Compton subtraction method.

The Folding Iterative Method

Given a defined response matrix $\boldsymbol{R}$, the elements R_{ij} each represent the energy (corresponding to channel i) which is deposited when the detector is hit by γ rays with an energy corresponding to channel j. Each j response function is normalized to 1, i.e., $\sum_i^N R_{ij} = 1$. The objective of the Folding Iterative Method is to obtain the unfolded matrix u, which is related to the folded matrix f through the relationship given by

$$f = \boldsymbol{R}u \tag{4.2}$$

which can also be expressed in the form expanded for all γ-ray energies (from $j = 1$ to $j = N$) as given by

$$\begin{pmatrix} f_1 \\ f_2 \\ \vdots \\ f_N \end{pmatrix} = \begin{pmatrix} R_{11} & R_{12} & \dots & R_{1N} \\ R_{21} & R_{22} & \dots & R_{2N} \\ \vdots & \vdots & \dots & \vdots \\ R_{N1} & R_{N2} & \dots & R_{NN} \end{pmatrix} \begin{pmatrix} u_1 \\ u_2 \\ \vdots \\ u_N \end{pmatrix}. \tag{4.3}$$

The folding method begins with a first trial function u^0 for the unfolded spectrum that is folded to obtain f, which is then compared to the observed spectra r. This process is accomplished following the steps as outlined below:

1. Assign first trial functions for the unfolded spectra as the observed spectra r: $u^0 = r$.
2. Fold first trial spectra: $f^0 = \boldsymbol{R}u^0$.
3. Obtain next trial functions from the difference spectra $r - f^0$: $u^1 = u^0 + (r - f^0)$.
4. Fold new trial function: $f^1 = \boldsymbol{R}u^1$.
5. Obtain the next unfolded spectra: $u^2 = u^1 + (r - f^1)$.

In this process, Steps 4 and 5 are repeated until the i^{th} iteration is reached where $f^i \sim r$. The iterative folding procedure continues until the folded spectrum agrees with the observed spectrum within the experimental uncertainties. Reference [84] finds that the condition is met by the 10^{th} iteration.

The Compton Subtraction Method

The Compton subtraction method begins by deriving the contribution of five spectrum components: the full energy u_f, single escape u_s, double escape u_d, and annihilation u_a, from the unfolded spectra of the last iteration, $u = u^{10}$. The probabilities of the five spectrum components are denoted, respectively, as $p_f(i)$, $p_s(i)$, $p_d(i)$, and $p_a(i)$ for an event at channel i, and thus the contribution of each is

$$u_f(i) = p_f(i)u(i), \tag{4.4}$$

$$u_s(i - i_{511}) = p_s(i)u(i), \tag{4.5}$$

$$u_d(i - i_{1022}) = p_d(i)u(i), \tag{4.6}$$

$$u_a(i_{511}) = \sum_i p_a(i)u(i). \tag{4.7}$$

In the aforementioned equations, i_{511} and i_{1022} represent the channels with energies 511 keV and 1022 keV, respectively. The Folding Iterative Method results in unfolded spectra with artificially better resolution, so to correct for this effect, the contributions of each of the five spectrum components are smoothed with the experimental resolution.

Subtracting these features from the observed spectra r results in isolating only the Compton continuum contribution:

$$c(i) = r(i) - \nu(i), \tag{4.8}$$

where $\nu(i)$ is the sum of the described structures. In the development of this method, Reference [84] notes strong oscillations from channel-to-channel in the Compton continuum spectra, so an additional smoothing of $2\text{FWHM}^{\text{exp}}$ is applied to the Compton contribution, $c(i)$. This is justified by the concept that $c(i)$ should be a spectrum which varies slowly as a function of energy as discussed at the beginning of Section 4.1. To obtain the spectra of only full energy peaks, the Compton continuum and other structures are removed from the observed spectra presented in Eq. 4.9:

$$u_{unf}(i) = r(i) - c(i) - u_s(i - i_{511}) - u_d(i - i_{1022}) - u_a(i_{511}). \tag{4.9}$$

The spectra of full energy peaks are then adjusted to the probability that an event is a full energy peak, and then corrected for the γ-ray detection efficiency ϵ_γ, resulting in Eq. 4.10:

$$U(i) = \frac{u_{unf}(i)}{p_f(i)\epsilon_\gamma}. \tag{4.10}$$

It was demonstrated in Reference [84] that the unfolding method reliably obtains unfolded spectra with the correct overall shape of the observed spectra with small fluctuations.

4.2 Distribution of First-Generation γ Rays

As a consequence of large decay widths at high excitation energies, discriminating between overlapping states with very short lifetimes is challenging, and as a result, γ rays are not well separated in energy and time. The authors of Reference [83] developed an iterative subtraction method to separate the primary γ ray from the γ rays which originate from the later steps in the decay cascade. The method relies upon the assumption that the compound nucleus (CN) mechanism dominates in both instances where a state is populated directly by a particle reaction or by the first γ-transition from a state above. The assumption then implies that the decay pathways are the same whether they proceed from a nuclear reaction or from γ decay initiated at high excitation energies.

From the first step of the β-Oslo Method, as presented in Section 4.1, the unfolded spectra are obtained, which will henceforth be referred to as f_i for each excitation energy bin i. Figure 4.1 illustrates the method of removing 2^{nd}, 3^{rd}, and higher generation γ rays from each excitation energy bin i. Relying on the discretization of excitation energy bins as $i = 1, 2, \ldots, N$ where $i = 1$ is the lowest excitation energy bin and N is the highest excitation

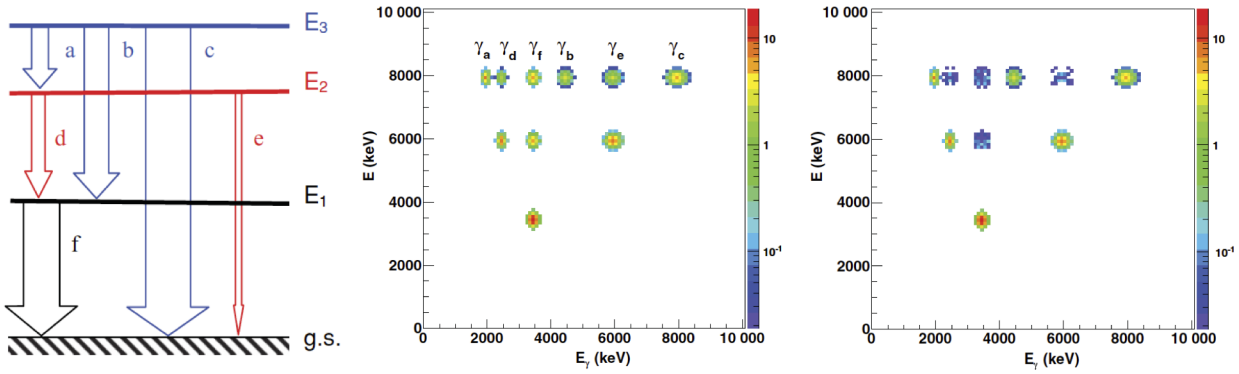


Figure 4.1: Hypothetical decay scheme (left) of primary γ rays and higher generation γ rays. The matrix of unfolded γ-ray spectra (center) as a function of excitation energy (E_1, E_2, E_3) is compared to resulting primary γ-ray matrix (right) highlighting the removal of higher-order γ rays [85].

energy bin, the primary (i.e., first generation) γ rays are the sole difference between the spectrum f_i and all spectra $f_{j<i}$. This inter-spectra relationship which is used to determine the first generation γ-rays spectrum h_i can be expressed compactly in the form presented in Eq. 4.11,

$$h_i = f_i - g_i, \tag{4.11}$$

where g_i is the weighted sum of all spectra $f_{j<i}$ by a correction coefficient n_{ij} and decay probability w_{ij}, as shown in Eq. 4.12:

$$g = \sum_{j}^{N} n_{ij} w_{ij} f_j. \tag{4.12}$$

The decay probabilities w_{ij} from high excitation states i to underlying states j are normalized to one. In essence, w_{ij} are the branching ratios of the primary γ rays, and thus w_{ij} is equivalent to the first generation spectrum h_i normalized to one. Initially the w_{ij} coefficients are unknown, so a trial function is assumed and is iterated over using the following steps:

1. Select a trial function w_i^0.
2. Calculate $h_i^0 = f_i - g_i^0$.
3. Select next set of decay probabilities $h_i^0 = w_i^1$.
4. Repeat steps 2 and 3 until $w_i^1 \approx w_i^0$

The effects of an improper choice of the decay probabilities can be mended with a coefficient close to unity called α, which is applied to the area of spectra g_i thus Eq. 4.11 becomes

$$A(h_i) = A(f_i) - \alpha A(g_i). \tag{4.13}$$

Equation 4.13 results in γ-ray spectra with multiplicity of one. In Eq. 4.13, the number of primary γ rays in f_i equals $A(f_i)/\langle M_i\rangle$, where $\langle M_i\rangle$ is the average multiplicity of spectrum i. As the number of γ-decay cascades, i.e., the number of primary γ rays, must remain constant, then the relationship given by Eq. 4.14 must be met throughout the first-generation process:

$$A(h_i) = A(f_i)/\langle M_i\rangle. \tag{4.14}$$

Substituting Eq. 4.14 in 4.13 results in an expression for α:

$$\alpha = (1 - 1/\langle M_i\rangle)\frac{A(f_i)}{A(g)}. \tag{4.15}$$

Here, the correction factor α is restricted to between 0.85 and 1.15, i.e., area correction is restricted to 15%.

In addition to the small correction α, the n_j coefficient adjusts the intensity populating states in bin i and underlying bins j, and represents the multiplicative factor applied to each unfolded spectra to maintain a fixed number of cascades. Reference [83] describes two manners of calculating n_j: singles normalization and multiplicity normalization. For particle-coincidence data analyzed using the standard Oslo Method, the singles normalization is utilized, while total absorption data from β-Oslo experiments are analyzed using a multiplicity normalization method. It is observed experimentally that the multiplicity, as a function of excitation energy, is related to the γ-ray energy [86, 87]. Assuming that $\langle E_\gamma\rangle$ represents the average γ-ray energy for an excitation state E with N cascades and the i^{th} of N cascade with a multiplicity M_i, Eq. 4.16 holds true:

$$\langle E_\gamma\rangle = N \cdot \frac{E}{\sum_{i=1}^{N} M_i} = \frac{E}{\frac{1}{N}\sum_{i=1}^{N} M_i} = \frac{E}{\langle M\rangle}. \tag{4.16}$$

In other words, the average multiplicity for excitation energy bin i can be expressed as $\langle M_i\rangle = E_i/\langle E_\gamma\rangle$. The number of counts measured for bins i and j is proportional to $A(f_i)/\langle M_i\rangle$ and $A(f_j)/\langle M_j\rangle$, respectively. The normalization factor n_j can be expressed as the form given in Eq. 4.17:

$$n_{ij} = \frac{\langle M_j\rangle A(f_i)}{\langle M_i\rangle A(f_j)}. \tag{4.17}$$

In summary, the iterative process varies the w_{ij} functions used in Eq. 4.12 to calculate the area representative of higher order γ rays, which is then subtracted from the total area $A(f_i)$. The procedure outlined continues to calculate and update the values of w_{ij} and α until convergence is reached within a tolerance of 10^{-2} ($w_i^{new} \approx w_i^{old}$) and $\alpha = 1.0 \pm 0.15$. Reference [83] applied the method to simulated γ spectra and achieved convergence within three iterations. In general, for experimental data, convergence is achieved with 20 iterations or less.

4.3 Extraction of the Nuclear Level Density and γ-ray Strength Function

From the γ-ray spectra of the first emitted γ-rays, information regarding the density of final states E_f (NLD) and the γ-ray strength function (γSF) can be extracted. The probability for an excitation energy E_i to decay by emitting a γ ray with energy E_γ can be compactly expressed as a matrix of first generation γ-ray spectra, $P(E_i, E_\gamma)$.

The first generation matrix $P(E_i, E_\gamma)$ is proportional to two independent functions: the NLD $\rho(E_f)$ and the transmission coefficient $\mathscr{T}(E_\gamma)$ (or the γSF) and is expressed as

$$P(E_i, E_\gamma) \propto \rho(E_f)\mathscr{T}(E_\gamma). \tag{4.18}$$

The transmission coefficient $\mathscr{T}(E_\gamma)$ is directly related to the γSF by Eq. 2.35. In addition, $\mathscr{T}(E_\gamma)$ and $f_{XL}(E_\gamma)$ are linked to the NLD through the mean total width of the capture state $\langle\Gamma(E, J^\pi)\rangle$ given by Eq. 2.50 (Eq. 6 from Reference [88]). Furthermore, the $\langle\Gamma(E, J^\pi)\rangle$ relates the $f_{XL}(E_\gamma)$ to neutron resonance data with the expression given by Eq. 4.19,

$$f_{XL}(E_\gamma) = \frac{\langle\Gamma(E, J^\pi)\rangle}{E_\gamma^{2L+1} D_{XL}}, \tag{4.19}$$

where D_{XL} is the s-wave neutron level spacing. The right-hand side of Eq. 4.19 can be replaced with the definition of γSF from Eq. 2.35 and can be used to solve for $\mathscr{T}(E_\gamma)$. The resulting relationship between $\mathscr{T}(E_\gamma)$ and $\langle\Gamma(E, J^\pi)\rangle$ can then be substituted into Eq. 2.50 to yield:

$$\mathscr{T}(E_\gamma) = \frac{2\pi}{D_{XL}} \frac{1}{\rho(E, J^\pi)} \sum_{XL} \sum_{J_f, \pi_f} \int_{E_\gamma=0}^{E} dE_\gamma E_\gamma^{2L+1} \times f_{XL}(E_\gamma)\rho(E - E_\gamma, J_f, \pi_f) \tag{4.20}$$

The shape of the $\mathscr{T}(E_\gamma)$ (or the $f_{XL}(E_\gamma)$) is highly dependent on the NLD, as will be shown in Chapter 5.

To extract the functional forms of $\rho(E_f)$ and $\mathscr{T}(E_\gamma)$, the first generation γ-ray spectra for each excitation energy must first be normalized to one so as to represent the decay probability of emitting γ energies at an initial excitation energy E_i, i.e.,

$$\sum_{E_\gamma=E_\gamma^{\min}}^{E_i} P(E_i, E_\gamma) = 1. \tag{4.21}$$

From the initial assumption, Eq. 4.18, the first generation matrix can be normalized as

$$P_{th}(E_i, E_\gamma) = \frac{\rho(E_i - E_\gamma)\mathscr{T}(E_\gamma)}{\sum_{E'_\gamma=E_\gamma^{\min}}^{E_i} \rho(E_i - E'_\gamma)\mathscr{T}(E'_\gamma)} \tag{4.22}$$

Reference [9] illustrates that if one solution to Eq. 4.22 can be found, then an infinite number of functions can be constructed which provide equivalent fits to the $P(E_i, E_\gamma)$ matrix by Eqs. 4.23 & 4.24:

$$\tilde{\rho}(E_i - E_\gamma) = A\rho(E_i - E_\gamma)e^{\alpha[E_i - E_\gamma]}, \tag{4.23}$$

$$\tilde{\mathscr{T}}(E_i - E_\gamma) = B\mathscr{T}(E_\gamma)e^{\alpha E_\gamma}. \tag{4.24}$$

Parameters A, B, and α are determined by three normalization conditions discussed in the following section.

Solutions to Eq. 4.22 are approximated through a χ^2-minimization iterative method developed by Schiller *et al.* [9]. The iterative method minimizes the difference between the theoretical and experimental first generation γ-ray matrices, namely:

$$\chi^2 = \frac{1}{N_{\text{free}}} \sum_{E_i=E_i^{\min}}^{E_i^{\max}} \sum_{E_\gamma=E_\gamma^{\min}}^{E_i} \left(\frac{P_{th}(E_i, E_\gamma) - P(E_i, E_\gamma)}{\Delta P(E_i, E_\gamma)} \right)^2 \tag{4.25}$$

where N_{free} is the number of degrees of freedom and $\Delta P(E_i, E_\gamma)$ is the uncertainty in the experimental first generation γ-ray matrix. The reduced χ^2 is minimized in respect to $\rho(E_i - E_\gamma)$ and $\mathscr{T}(E_\gamma)$,

$$\frac{\partial}{\partial \mathscr{T}(E_\gamma)}\chi^2 = 0 \qquad \text{and} \qquad \frac{\partial}{\partial \rho(E_i - E_\gamma)}\chi^2 = 0, \tag{4.26}$$

which allows one to extract the zeroth- and higher-order estimates $\rho^{(n)}(E_i - E_\gamma)$ and $\mathscr{T}^{(n)}(E_\gamma)$. The zeroth-order estimate assumes $\rho(E_f)^0 = 1$ and estimates the transmission coefficient, using Eq. 4.22 while maintaining the condition $E_i \geq E_\gamma$, as given by

$$\mathscr{T}^0(E_\gamma) = \sum_{E_x=E_i^{\min}}^{E_i^{\max}} P(E_i, E_\gamma). \tag{4.27}$$

The method is iteratived over updated values of $\chi^{2^{(n)}}$, which are calculated from $\rho^{(n)}(E_i - E_\gamma)$ and $\mathscr{T}^{(n)}(E_\gamma)$ inserted into Eq. 4.25. Schiller *et al.* demonstrate that the method convergences to a minimum value of χ^2 quickly, but in cases where the χ^2 minimum is shallow, such as at high excitation energy where counts are sparse, a restriction on the maximum variation of ρ and $\mathscr{T}$ is placed to enhance the convergence.

To ensure that these extracted functions correspond to statistical γ rays, gates are placed on the γ-ray energy and excitation energy. A gate of $E_{\gamma,\text{low}}$ is placed on the γ-ray energy to avoid experimental problems of threshold walk of the analog-to-digital convertor (ADC) and bad timing properties of low-energy γ rays. In addition, the main assumption behind the Oslo Method is not valid at low excitation energy because the thermalization time might compete with the lifetime of the state leading to a more purely direct reaction than CN

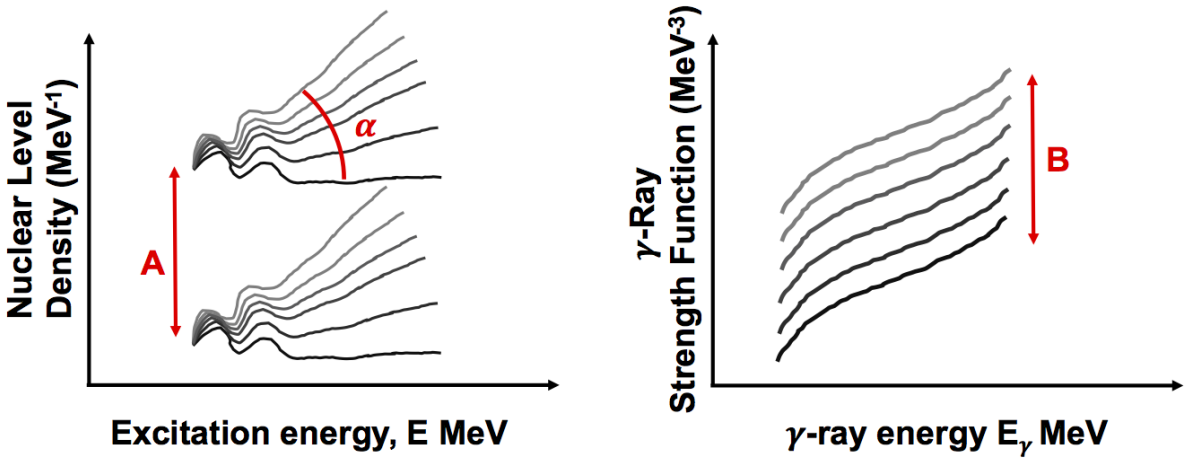


Figure 4.2: Hypothetical A, α, and B parameters used to determine the most physical solution for the NLD (left) and γSF (right).

state. For this reason gates at $E_{x,\text{low}}$ and $E_{x,\text{high}}$, determined by inspecting the multiplicity fluctuations, are imposed on the excitation energy.

The transmission coefficient $\mathscr{T}(E_\gamma)$ is a function of γ-ray energy and is independent of excitation energy, as proposed by the Brink-Axel hypothesis [45, 46] discussed in Chapter 2 through the example of ^{64,65}Ni shown in Fig. 2.6 [49]. In brief, it states that at all levels exhibit the same collective giant dipole mode as the ground state. This was illustrated for both a high NLD nucleus such as ^{238}Np and lower NLD nuclei such as ^{64,65}Ni to demonstrate the impact of Porter-Thomas fluctuations, which are greater for lighter nuclei [50, 49].

While error propagation through these methods discussed in Sections 4.1-4.3 has heretofore not been performed, Reference [9] placed a great deal of effort in estimating the statistical uncertainty of NLD and γSF. In addition, the effects of the normalization methods within each procedure are shown in Chapter 5.

4.4 Normalization of the Nuclear Level Density & γ-ray Strength Function

The previous section discussed how to extract and construct functions of the NLD and transmission from an infinite set of solutions that fit the $P(E_i, E_\gamma)$ matrix equally well. The functions given by Eqs. 4.23 and 4.24 are normalized to known data in order to obtain the most physical solution. Parameters A, B, and α are determined from neutron resonance data, which for many neutron rich nuclei are incomplete, as is the case for ^{92}Sr(n,γ). In such cases, various normalization approaches that utilize global systematics of Refs. [30, 31, 32] within phenomenological models and semi-experimental $\rho(S_n)$ values of neighboring stable

nuclei are investigated. An additional normalization approach utilized in this dissertation is estimated values from the Hartree-Fock-Bogoliubov plus combinatorial (HFB + c) model fit to the discrete states of ^{93}Sr [20]. The use of these approaches to estimate normalization parameters are discussed in Chapters 2 and 5.

The slope α and absolute value A of the NLD are obtained from anchoring $\tilde{\rho}(E_f)$ at low excitation energy to the number of discrete levels, as well as at high excitation energy to an estimate of the level density at the neutron separation energy $\rho(S_n)$. Typically, a known number of experimentally-obtained levels are reported by the Evaluated Nuclear Structure Data (ENSDF) library [23]. The level density at the neutron separation energy $\rho(S_n)$ is estimated from available neutron resonance spacing data reported by the Reference Input Parameter Library (RIPL-3) [36]. If the s-wave neutron level spacing D_0 is known, then the total level density can be calculated at S_n by the expression

$$\rho(S_n) = \frac{2\sigma^2}{D_0} \frac{1}{(J_t+1)\exp[-(J_t+1)^2/2\sigma^2] + J_t\exp[-J_t^2/2\sigma^2]}, \tag{4.28}$$

where J_t is the target spin and σ is the spin-cutoff parameter. Generally, D_0 is obtained from neutron-capture experiments; however, this value is experimentally unknown for short-lived nuclei. In this case, as was previously demonstrated by successful experiments using the (β-)Oslo Method (*e.g.* ^{75}Ge(n,γ) [10], ^{89}Y(p,γ) [73], and ^{64}Ni$(d,p\gamma)$ [89]), D_0 is determined by inspecting the systematics of neutron resonance data of the surrounding mass region.

As α is present in both Eqs. 4.23 and 4.24, the slope of the transmission coefficient, and consequently the γSF, is dependent on the normalization of the NLD. The remaining parameter B in Eq. 4.24 determines the absolute normalization of the γSF. The resulting shifts of these three parameters are illustrated in Fig. 4.2. In Reference [88], it is assumed that the main radiation contributing to the γSF are of type and multipolarity: $E1$ and $M1$, and that levels populated are of equal amounts of positive and negative parity for any energy and spin. Higher order multipoles are negligible as $E1$ and $M1$ transitions are five orders of magnitude more probable than quadrupole transitions [18]. The transmission coefficient can be expressed in terms of the $E1$ and $M1$ strength (comparable to Eq. 2.35):

$$B\mathscr{T}(E_\gamma) = [f_{E1}(E_\gamma) + f_{M1}(E_\gamma)]E_\gamma^3. \tag{4.29}$$

To solve for B, Eq. 2.50 (developed by Reference [88]) is used in combination with Eq. 4.29 to yield the average total radiative width for s-wave neutron capture by a target nucleus of spin J_t and parity π_t, as shown by Eq. 4.30,

$$\langle\Gamma(S_n, J_t \pm 1/2, \pi_f)\rangle = \frac{1}{2\rho(S_n, J_t \pm 1/2, \pi_f)} \int_{E_\gamma=0}^{S_n} dE_\gamma B\mathscr{T}(E_\gamma)\rho(S_n - E_\gamma)\times \sum_{j=-1}^{1} g(S_n - E_\gamma, J_t \pm 1/2 + j); \tag{4.30}$$

where $g(E, J)$ is the spin distribution function. The last normalization parameter, the absolute value B, is determined by solving Eq. 4.30 given a known D_0 and $\langle\Gamma_0\rangle$. Similar to the case of obtaining D_0 experimentally, $\langle\Gamma_0\rangle$ is determined in photoabsorption experiments, which is not possible for short-lived nuclei. Lastly, the γSF $f_1(E_\gamma)$ is obtained from the extracted $\mathscr{T}(E_\gamma)$, and is subsequently normalized using the B parameter. In the case of ^{93}Sr, an estimated $\langle\Gamma_0\rangle$ value was obtained from a linear fit of known value for neighboring stable nuclei as a function of mass number as shown in Fig. 2.12 of Chapter 2.

The extracted $\rho(E_f)$ was obtained for an excitation energy range of 0 MeV to $S_n - E_{\gamma,\text{low}}$, while the extracted $f_1(E_\gamma)$ corresponds to γ-ray energies of $E_{\gamma,\text{low}}$ to $\sim S_n$ for ^{93}Sr. For $E_f > S_n - E_{\gamma,\text{low}}$ counts are expected to be relatively low, so it is necessary to extrapolate the experimentally determined $\rho(E_f)$using the Back-Shifted Fermi Gas or Constant Temperature model in order to solve Eq. 4.30 [88]. Reference [88] found the contribution from extrapolating the γSF to be $\leq 15\%$; thus, this contribution is generally considered an insignificant contributor to the error calculation.

The standard Oslo Method as well as the β-Oslo Method depend on a fourth normalization parameter that represents the mismatch in populated levels between an indirect technique such as charged particle reactions or β decay and the direct neutron-capture reaction. In the case of a large mismatch between the observed populated states and predicted total level density, a reduction factor is implemented to determine the appropriate slope of the NLD and γSF as was for the case for Th, Pa, U, and Pu [90, 91]. Consequently, when the reduction parameter can not be experimentally obtained, e.g, determining the γSF for ^{76}Ge using the β-Oslo Method [10] and γSF for ^{243}Pu using the standard Oslo Method [91], the reduction factor is estimated using phenomenological and microscope model approaches. The spin distribution of ^{93}Sr and its impact in reducing the NLD are discussed with experimental results in Chapter 5.

Chapter 5

Experimental Results

The β decay of ^{93}Rb was studied using the β-Oslo Method to extract the nuclear level density (NLD) and γ-ray strength function (γSF) of the neutron rich fission fragment ^{93}Sr. As there is currently no available experimental nuclear level density parameters or neutron resonance parameters for ^{93}Sr, various approaches were investigated to estimate normalization parameters. The resulting γSF from the normalization of the NLD appears to be described by a pygmy resonance at 5.06(7) MeV with a width Γ_{pyg}=0.62(11) MeV and cross section σ_{pyg}=0.74(11) mb and an enhancement at low γ-ray energies below 2 MeV. The influence of utilized normalization approaches on the neutron capture cross section is discussed in Chaper 6.

5.1 ^{93}Rb Decay

The half-life of ^{93}Rb is 5.84 (2) s [23] and populates the ground state of ^{93}Sr with a β-decay intensity of 35% [25]. The β decay from the $5/2^-$ ground state of ^{93}Rb to the $5/2^+$ ground state of ^{93}Sr results in a Q-value of 7.466(9) MeV. The known β-feeding intensities as reported by ENSDF shown in Fig. 2.3, indicate that there is a high likelihood β decay will populate the ground states and states between 3.8 MeV and 4 MeV. The first and second excited states, 213.431 keV [A] and 432.604 keV [B], are populated by β decay with an intensity of $\leq$1.5% and $\leq$6.5%. In addition to the first two excited states, the third, fourth, and fifth excited states, 986.12 keV [C], 1142.55 keV and 1148.20 keV [D], are visible in the TAS spectrum of ^{93}Sr in Fig. 5.1. At 1.15 MeV the resolution of the SuN detector is approximately 30 keV, therefore the states at 1142.55 keV and 1148.20 keV [D] appear as one peak. Following the ground state, the most intensely populated states by β decay are those at approximately 3.8-4.0 MeV which predominantly emit $\leq$2 MeV γ rays. The 3890.64 keV [E] level is the most β-populated level in the region. In addition, the strongest β-delayed γ-ray transition is 432.61(3) keV [M] with a relative intensity of 20.2(14)%. The next four most intense γ-ray transitions are also visible in the γ-ray spectrum of ^{93}Sr shown in Fig. 5.2: 213.43(11) keV [L] (I_γ = 7.76(57)%), 709.95(5) keV [N] (I_γ = 6.22(54)%), 986.05(6) keV [P] (I_γ = 7.90(56)%),

and 1385.21(8) keV [Q] ($I_\gamma = 6.63(46)\%$).

As for the decay daughter of ^{93}Sr, the TAS spectrum of ^{93}Y in Fig. 5.1 highlights several of the strongly β-populated states: 875.85 keV [F], 1300.521 keV and 1308.56 keV [G], as well as the most populated states within the detector's resolution of 53 keV, 2569.95 keV and 2575.04 keV [H]. In Fig. 5.2, the four most intense γ-ray transitions are visible: 590.238(23) keV [R] ($I_\gamma = 68(5)\%$), 710.312(17) keV [S] ($I_\gamma = 21.76(150)\%$), and 875.73(6) keV [T] ($I_\gamma = 24.48(174)\%$) and 888.13(5) keV [T] ($I_\gamma = 22.1(15)\%$), which are seen as one peak due to the detector resolution of 26 keV at 880 keV. The decay daughter ^{93}Y most often de-excites through the emission of <1 MeV γ rays.

The raw spectra discussed also include photon interactions with matter that result in a detector response less than the energy of the photoabsorption peak of an incident γ ray. However, the probability of detecting the full energy peak (p_{FE}) using the SuN detector is high for individual γ rays below one MeV, $p_{FE} = 43 - 64$ %, while the probability of single or double escape peaks and an annihilation peak is zero. In the case of both ^{93}Sr and ^{93}Y, highly excited states often de-excite by emitting $\leq$2 MeV γ rays, but nevertheless there is a probability of high-energy γ-emission. For $E_\gamma < 5.5$ MeV, $p_{FE} = 22 - 41$ % while the probability of single and double escape peaks is still low, $p_{SE} = 2.0 - 6.4\%$ and $p_{DE} = 0.1 - 0.2\%$, and the probability of the annihilation peak is $p_{511} = 1.3 - 6.5\%$. The impact of Compton scatter is small while pair-production interactions are zero for ^{93}Sr γ peaks, 213.43(11) keV [L], 432.61(3) keV [M], 709.95(5) keV [N], as well as for ^{93}Y γ peaks, 590.238(23) keV [R] and 710.312(17) keV [S]. In contrast, Compton scatter is more impactful while pair-production interactions have a finite impact on 986.05(6) keV [P], 1385.21(8) keV [Q], 875.73(6) keV [T], and 888.13(5) keV [T].

5.2 From β-γ Coincidence Data to Primary γ-ray Spectra

The initial γ-ray energies and excitation energies experimentally measured using total absorption spectroscopy (TAS) are histogrammed into a 2D matrix representing the raw β-Oslo matrix. Initial β-γ coincidence measurements are shown in Fig. 5.3a, where γ-ray spectra are expressed as a function of excitation energy. The measured β-delayed γ rays include both the decay of ^{93}Rb into ^{93}Sr and ^{93}Sr into ^{93}Y, which represents a form of contamination. The decay daughter contamination of ^{93}Y shown in Fig. 5.3b is subtracted from the initial experimental matrix; thus a β-Oslo matrix is obtained for states in ^{93}Sr shown in Fig. 5.3c. The method used for the contamination subtraction is described in Chapter 3. These three raw matrices are shown in Fig. 5.4 using 40 keV wide bins on both the γ-ray energy and excitation energy axes.

The decay daughter-subtracted raw matrix (Fig. 5.3c) is unfolded along the horizontal axis using the response function of SuNTAN and the unfolding procedure described in Chapter 4. Figure 5.4a shows the unfolded matrix of ^{93}Sr γ-ray spectra. These unfolded

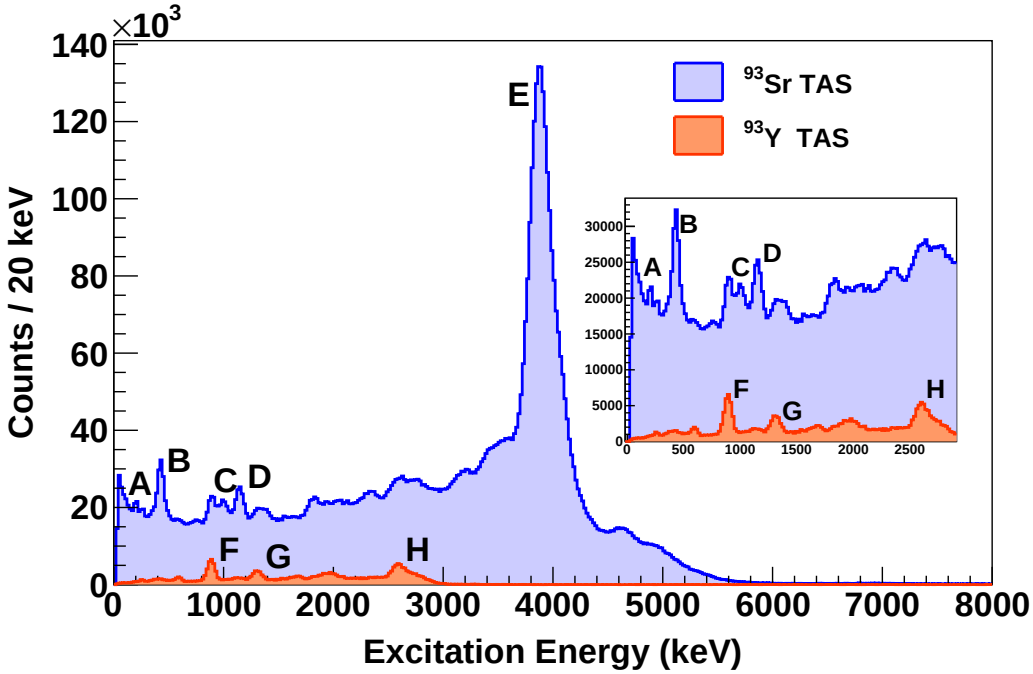


Figure 5.1: The raw ^{93}Sr TAS spectrum (blue) following the subtraction of the ^{93}Y decay daughter contaminant spectrum (orange). Labeled excited states populated by β decay are discussed in the text.

γ-ray spectra include first generation and higher order γ rays, which are removed using the procedure described in Chapter 4. This procedure utilizes an iterative subtraction method, which depends on a normalization factor based on the average γ-ray multiplicity per excitation energy bin. Figure 5.4b shows the primary γ rays separated by a later step in the decay cascade. The average γ multiplicity calculated using Eq. 4.16 is shown in Fig. 5.5 as a function of excitation energy. Above the neutron separation energy (S_n), the average γ multiplicity decreases as particle emission is possible. The low-energy levels of ^{92}Sr will determine an upper excitation energy threshold in the analysis of the ^{93}Sr NLD and γSF.

Figure 5.4b of the unfolded primary matrix exhibits an absence of primary transitions in various locations. In the case of $(E_\gamma, E_x) = (0.89, 1.49)$ MeV and $(1.29, 4.09)$ MeV, the absence of these primary transitions is in agreement with ENSDF reported levels and γ rays. For instance, from excitation energies between 1.39-1.59 MeV, no primary γ rays between 0.79-0.99 MeV are reported by ENSDF. In the case of excitation energies between 3.99-4.19 MeV, ENSDF reports that the 4097.3 keV level emits a 1359.92(16) keV γ with a relative intensity of 37(3)%; however, the 4097.3 keV level is populated less intensely by β decay compared to the levels immediately below such as those near 3.8-3.89 MeV. In addition, the energy level at 1385.31 keV decays only by primary γ-ray emission to the

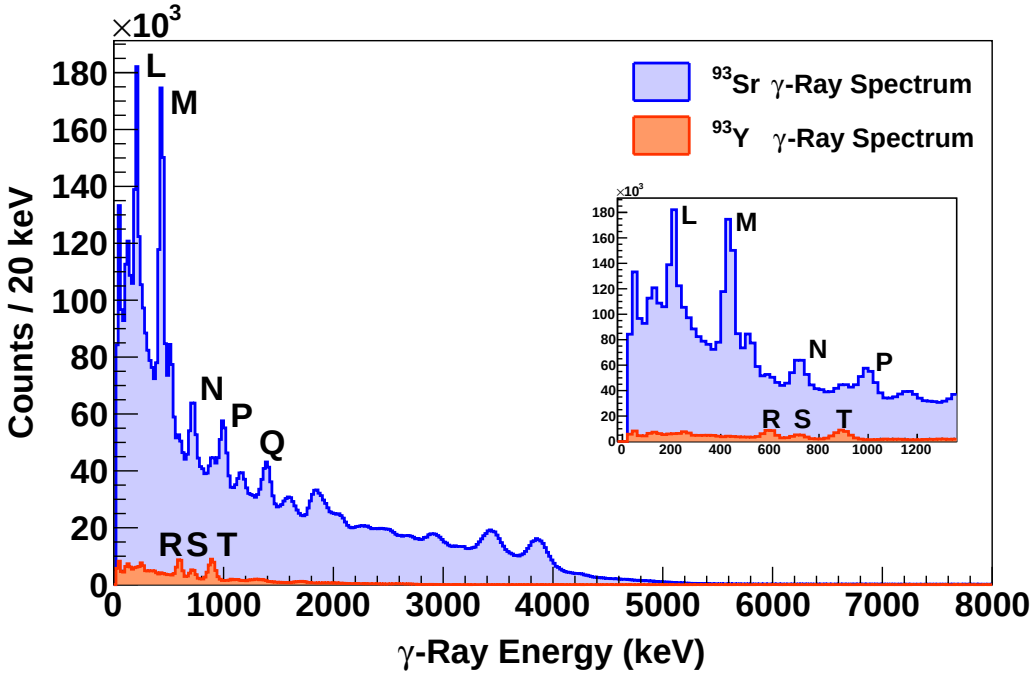
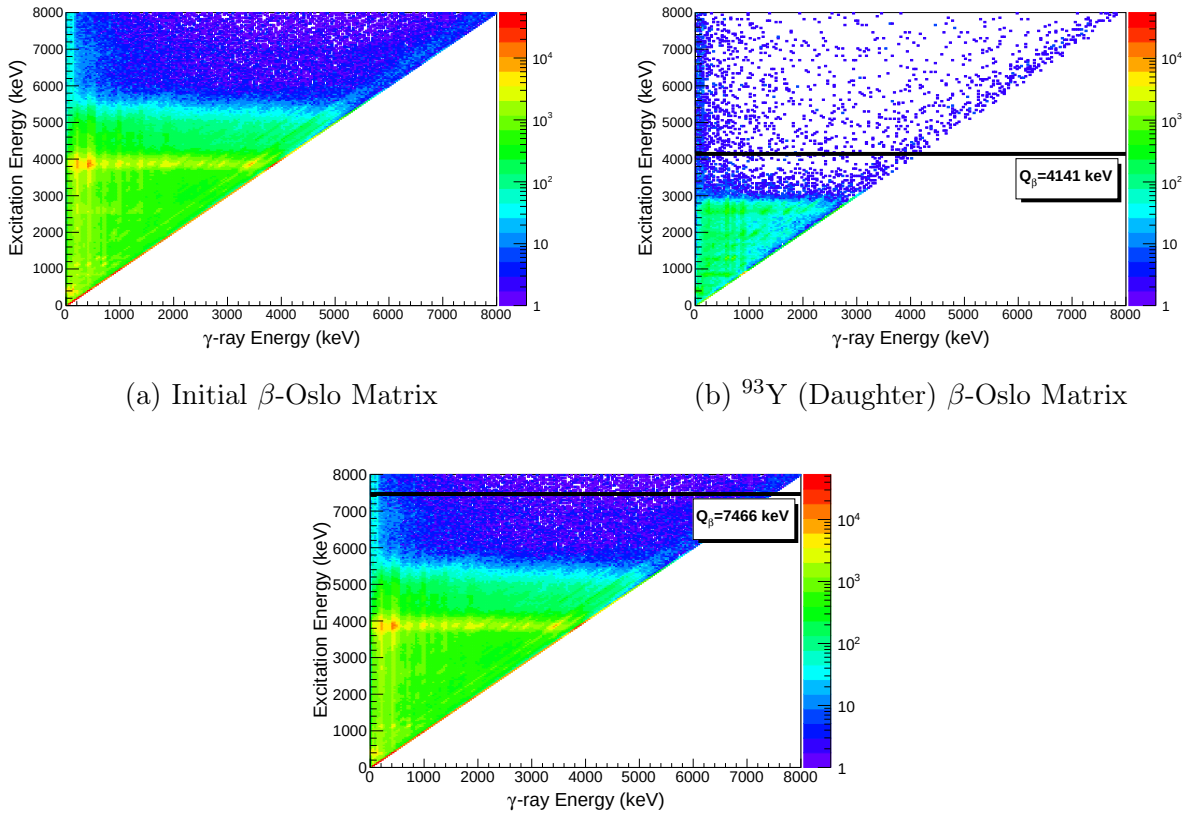


Figure 5.2: The raw ^{93}Sr γ-ray spectrum (blue) following the subtraction of the ^{93}Y decay daughter contaminant spectrum (orange). Labeled β-delayed γ-ray transitions populated by β decay. Peaks of strongly populated levels are labeled and discussed in the text.

ground state compared to the level at 4097.3 keV which decays primarily by 3664.75(19) keV γ to the second excited state. For excitation energies greater than 5.4 MeV, which is 100 keV above S_n, few primary γ rays were observed with energies below 1.5 MeV, visible in the upper-left corner of the triangle in Fig. 5.4b, and few primary γ transitions leading to the ground state, visible in the upper-right corner of the triangle in Fig. 5.4b. However, for excitation energies between 2.8 MeV and S_n, few low energy primary γ rays between 600-900 keV were seen which disagrees with ENSDF reported γ rays. The γ rays with energy $E_\gamma < 1.0$ MeV are not correctly subtracted, which would indicate that these levels are more strongly populated by higher excited states through γ decay than directly from initial β decay. Consequently, a γ-ray energy lower threshold is placed to exclude non-statistical γ rays with energy $E_{\gamma,low} < 1.89$ MeV.

In addition to excluding non-statistical low-energy γ rays, an upper and lower threshold is placed on the excitation energy $(E_{x,min}, E_{x,max}) = (4.09, 5.49)$ MeV as illustrated in Fig. 5.4b. This excitation energy region, henceforth referred to as the analysis region, is utilized for the NLD and γSF analysis described in Sections 5.4, 5.5, and 5.6. The lower threshold $E_{x,min}$ was selected to avoid the levels strongly populated by β decay at 3.8-4.0 MeV, which is a very selective process and thus leads to populated states of similar spins and parity in a region

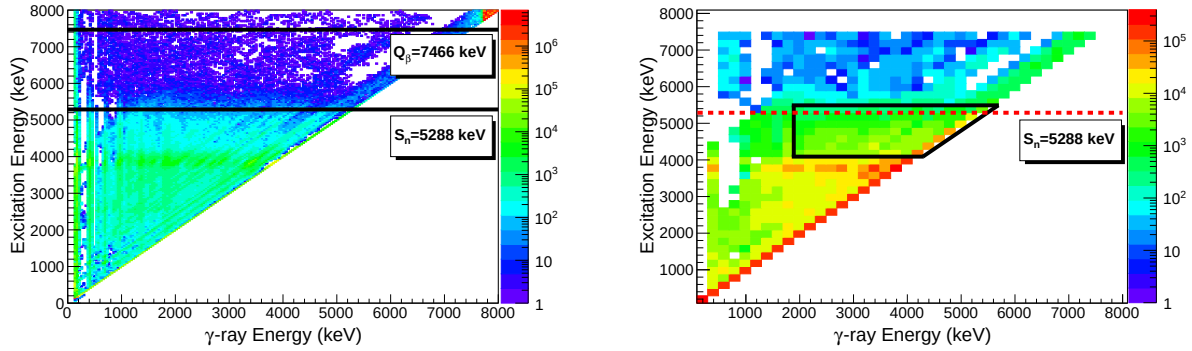


(a) Initial β-Oslo Matrix

(b) ^{93}Y (Daughter) β-Oslo Matrix

(c) ^{93}Sr (Parent) β-Oslo Matrix

Figure 5.3: Raw β-Oslo matrices shown are the initial experimentally measured γ-ray energies and excitation energies from (a) β-γ coincidences detected using SuNTAN, (b) the decay of ^{93}Sr to excited states of ^{93}Y, and (c) the decay of ^{93}Rb to excited states of ^{93}Sr. The decay daughter contamination ^{93}Y matrix (5.3b) was subtracted from the initial matrix (5.3a), resulting in the matrix of β-populated states of ^{93}Sr (5.3c). The γ-ray energies on the horizontal axes represent the individual γ rays measured by the inner NaI segments of SuN. The excitation energies on the vertical axes represent the total energies deposited in the SuN detector after the β decay event.



(a) Unfolded β-Oslo Matrix

(b) Primary β-Oslo Matrix

Figure 5.4: (a) Unfolded ^{93}Sr β-γ coincidence matrix and (b) ^{93}Sr primary γ-ray matrix. The bin width of the horizontal and vertical axes is 40 keV for the unfolded matrix (5.4a) and 200 keV for the primary matrix (5.4b). The trapezoid shown in the primary matrix marks the γ-ray and excitation energy thresholds.

of low level density. This region should be avoid as a result of low statistical distribution of levels populated by β decay. In addition, the upper threshold $E_{x,max}$ was selected to exclude γ rays emitted from the β-delayed neutron emission nucleus ^{92}Sr. As the $Q_\beta > S_n$, it is possible for ^{92}Sr excited states of energy $E_x < 2.18$ MeV to be populated. The first excited states of ^{92}Sr is 814.98(3) keV, so it is necessary to place $E_{x,high} < 6.1$ MeV to avoid including excited states from a daughter nucleus and then even lower than that to account for the detector resolution. Figure 5.6 shows the raw, unfolded, and primary γ-ray spectra of the analysis region. The primary γ-ray spectrum is also compared to the unfolded total γ spectrum and second and higher generation γ spectrum in Fig. 5.7, which shows a more bell-shaped form in the bottom panel except for a peak at around 4.0 MeV. If the primary γ spectrum of each excitation energy was inspected, a peak at $E_\gamma = E_x$ would be visible in the analysis region. This high-energy γ ray in each spectrum corresponds to a primary transition from the initial state to the ground state; however, these direct transitions are not included in the NLD as the NLD function is extracted up to $E_x = E_{x,max} - E_{\gamma,low} = 3.6$ MeV, and thus will not impact the shape of the NLD, and consequently the γSF shape. The impact of selecting a statistical region on the NLD and the γSF will be demonstrated in the following sections.

5.3 Obtaining the Normalization Parameters

The experimentally extracted NLD and γSF from the ^{93}Sr primary matrix require normalization to external nuclear data, if available; however, for a nuclei far from stability,

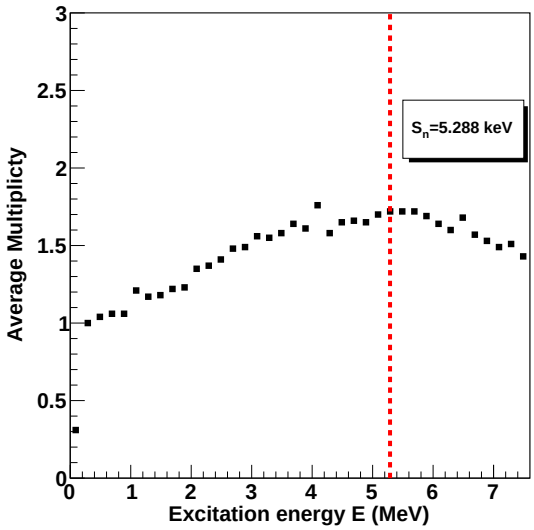


Figure 5.5: Calculated average γ-ray multiplicity using Eq. 4.16 for ^{93}Sr. See text for details on multiplicity normalization in Chapter 4.

normalization to estimates and model predictions is an alternative approach. In the case of ^{93}Sr, the first 20 discrete levels are used to normalize the NLD at low energy. The second normalization point at high excitation energy around S_n utilizes the average s-wave neutron resonance spacing D_0 to determine $\rho(S_n)$, which is not experimentally known for ^{93}Sr. A simple approach used when external nuclear data is unavailable is to calculate the normalization parameters in part from phenomenological models. Table 5.1 lists the three phenomenological models examined in this work: the Constant Temperature (CT), Back-shifted Fermi gas (BSFG), and Rigid Moment of Inertia (RMI) models, which were discussed in Chapter 2. For each model listed, the spin-cutoff parameter σ, nuclear level density $\rho(S_n)$, and s-wave neutron-resonance spacing D_0 for ^{93}Sr are calculated values obtained from the semi-empirical expressions of Ref. [30] and [32].

The phenomenological models chosen were used to calculate predicted $\rho(S_n)$ values for ^{86,88}Rb, ^{85,87,88,89}Sr, ^{90}Y, and $^{91-95,97}$Zr. However, for these neighboring nuclei of ^{93}Sr, the neutron resonance parameters: D_0 and $\langle\Gamma_\gamma\rangle$ are known [36] such that $\rho(S_n)$ can be estimated through Eq. 2.47. Model predicted values of $\rho(S_n)$ were fit to these experimentally-derived $\rho(S_n)$ values to determine a common scaling factor of $0.16^{+0.08}_{-0.07}$ for CT, $0.34^{+0.08}_{-0.07}$ for BSFG, and $0.31^{+0.09}_{-0.10}$ for RMI. If the fit is applied to only even-Z, odd-N, the scaling factors are $0.37^{+0.15}_{-0.16}$ for CT, $0.36^{+0.12}_{-0.11}$ for BSFG, and $0.31^{+0.18}_{-0.18}$. By using these scaling factors and upper/lower χ^2 uncertainties, the estimated $\rho(S_n)$ and D_0 for ^{93}Sr were obtained and are listed in Tables 5.2 and 5.3. The NLD at S_n ranges from 889 MeV^{-1} to 3023 MeV^{-1}, excluding the CT model estimates, which assumes an energy-independent σ [30]. The neutron-resonance

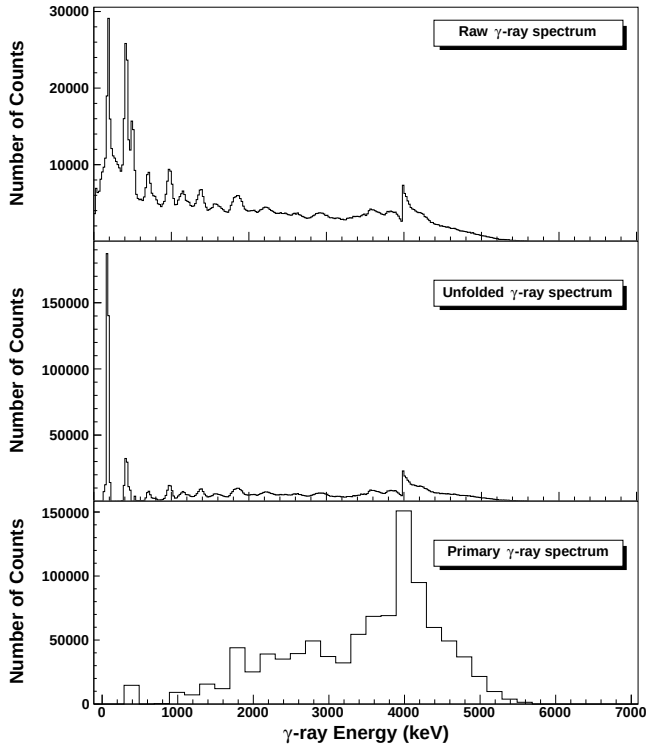


Figure 5.6: Raw, unfolded and primary γ-ray spectra of ^{93}Sr for excitation energy between 4.0-5.6 MeV. The γ-ray energy bins of the raw and unfolded spectra are 20 keV wide, while the bin width for the primary γ-ray spectrum is 200 keV.

spacing ranges from 13990 eV to 47550 eV. This range in normalization parameters serves as a range of the systematic uncertainty of the extracted NLD discussed in Section 5.5.

In contrast to the phenomenological approaches discussed, a microscopic model was also implemented to estimate the normalization parameters. The microscopic approach utilizes the Hartree-Fock-Bogoliubov plus combinatorial (HFB + c) method described by Ref. [42] to estimate the total nuclear level density from tabulated NLD values which are compared at low energy to known discrete levels to anchor calculated values to experimental nuclear data. The HFB + c tabulated NLD values can be shifted in energy by δ and in shape by c as so

$$\rho(E_x, J, \pi) = \rho_{HFM}(E_x - \delta, J, \pi)e^{c\sqrt{E_x - \delta}}. \tag{5.1}$$

The tabulated NLD were shifted by δ to determine the best agreement with the 20 known discrete levels of ^{93}Sr using a χ^2 approach. Table 5.4 list a range of δ values, of which δ=0.12 resulted in the best comparison. The HFB + c with δ=0.12 yields $\rho(S_n)$= 5.12×10^3(330) MeV^{-1}

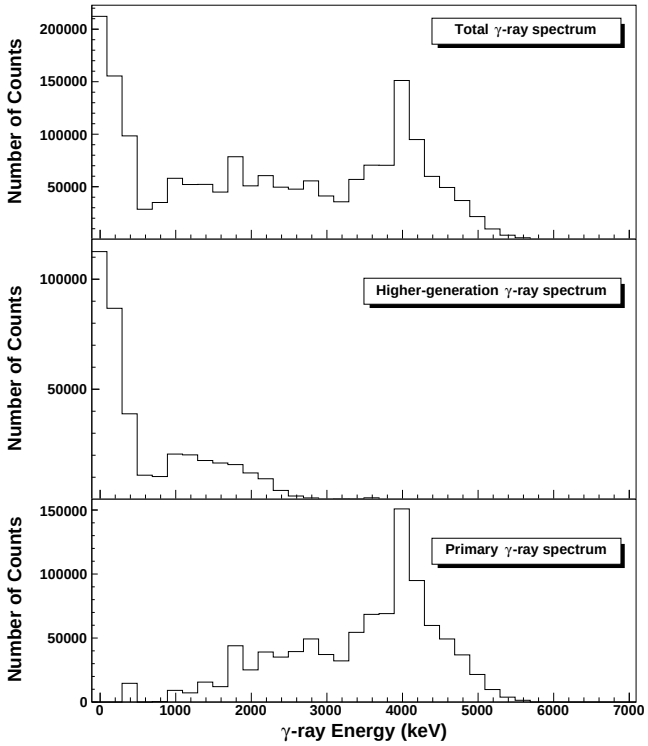


Figure 5.7: Unfolded total, higher-generation, and primary γ-ray spectra of ^{93}Sr for excitation energy between 4.0-5.6 MeV. The γ-ray energy bins are 200 keV wide.

Table 5.1: Calculated NLD parameters: spin-cutoff parameter, σ, total level density at S_n, $\rho(S_n)$, and s-wave level spacing, D_0, for ^{93}Sr from semi-empirical formulations of the NLD by Refs. [30, 31, 32].

Ref.	S_n (MeV)	σ	$\rho(S_n)$ (10^3 MeV^{-1})	D_0 (eV)
CT (Ref. [30])	5.288	3.648	2.4592	11240
BSFG (Ref. [32])	5.288	3.709	4.0896	6977
RMI (Ref. [30])	5.288	4.543	5.9292	7133

Table 5.2: Estimated $\rho(S_n)$ values for ^{93}Sr using neutron resonance parameters of neighboring nuclei [36]: ^{86,88}Rb, ^{85,87,88,89}Sr, ^{90}Y, and $^{91-95,97}$Zr, and semi-empirical expressions of the spin-cutoff parameter σ and total level density $\rho(S_n)$ from Refs. [30, 31, 32]. The expressions of σ and $\rho(S_n)$ are derived from the CT [30], BSFG [32], and RMI [30] models. The label *up*/*low* represent the upper(lower) χ^2 uncertainties on predictions derived from global systematics. Entries with an * indicate only even-Z and odd-N were used in the estimate.

Ref.	S_n (MeV)	$\rho^{sys}(S_n)$ (10^3 MeV^{-1})	$\rho^{sys,up}(S_n)$ (10^3 MeV^{-1})	$\rho^{sys,low}(S_n)$ (10^3 MeV^{-1})
CT	5.288	0.39	0.59	0.22
CT*	5.288	0.91	1.28	0.52
BSFG	5.288	1.39	1.72	1.10
BSFG*	5.288	1.47	1.96	1.02
RMI	5.288	1.84	2.37	1.25
RMI*	5.288	1.96	3.02	0.89

with D_0=5452 eV obtained from an exponential fit of calculated level densities between 4.5 MeV and 5.5 MeV. In addition, a fit of Eq. 2.22 to the HFB + c tabulated NLD values around S_n resulted in σ_{HFB+c}=3.77 shown in Fig. 5.12. While the spin-cutoff is in between the BSFG [32] and RMI [30] σ values, $\rho_{HFB+c}(S_n)$ is larger than values of either phenomenological model and D_0 is an order of magnitude smaller than the phenomenological approach. The HFB + c approach to normalizing the NLD contributes another source of systematic error discussed in Section 5.5.

The last normalization point utilized to determine the magnitude of the γSF is the mean total radiative width, $\langle\Gamma(S_n)\rangle$, which is also unknown for ^{93}Sr. The ^{93}Sr γSF is normalized to an estimated $\langle\Gamma(S_n)\rangle$=120(32) meV yielded from a linear tread of stable neighboring nuclei as described in Chapter 2. In Table 5.5, the estimated $\langle\Gamma(S_n)\rangle$ is listed along with the RIPL3 reported average value of the Giant Dipole Electric Resonance parameters [36].

The β-Oslo Method depends on three normalization parameters: known levels, estimated total level density at S_n ($\rho(S_n)$), and estimated average total radiative width ($\langle\Gamma(S_n)\rangle$). As a result, the experimentally-determined NLD and γSF from this work are influenced by the normalization approach whereby phenomenological model predictions are fit to semi-empirical $\rho(S_n)$ values and microscopic model estimates are anchored to known levels. In Chapter 6 the resulting influence as a systematic error on the neutron-capture cross section is discussed in terms of three factors: model selection used to estimate the total nuclear level density at S_n (and consequently, D_0), estimated $\langle\Gamma(S_n)\rangle$ from neutron resonance parameters of neighboring nuclei, and normalization to available photoabsorption data of ^{88}Sr [63, 92].

Table 5.3: Estimated s-wave neutron-resonance spacing D_0 values at S_n for ^{93}Sr using neutron resonance parameters of neighboring nuclei [36]: ^{86,88}Rb, ^{85,87,88,89}Sr, ^{90}Y, and $^{91-95,97}$Zr, and semi-empirical expressions of the spin-cutoff parameter σ and total level density $\rho(S_n)$ from Refs. [30, 31, 32]. Estimated D_0 values were calculated using Eq. 2.47. The label *up/low* represent the upper(lower) χ^2 uncertainties on predictions derived from global systematics. Entries with an * indicate only even-Z and odd-N were used in the estimate.

Ref.	S_n (MeV)	D_0^{sys} (keV)	$D_0^{sys,low}$ (keV)	$D_0^{sys,up}$ (keV)
CT	5.288	70.25	46.82	124.80
CT*	5.288	30.37	21.61	53.50
BSFG	5.288	20.53	16.62	25.84
BSFG*	5.288	19.38	14.54	27.92
RMI	5.288	23.01	17.84	33.97
RMI*	5.288	21.62	13.99	47.55

Table 5.4: Estimated total nuclear level density at S_n for ^{93}Sr using a microscopic model implemented in TALYS [20]: Hartree-Fock-Bogoliubov plus combinatorial (HFB + c) method by Ref. [42]. Tabulated value of the NLD were shifted by a value δ in energy to link to theoretical values to experimental nuclear data.

Shift Value δ	$\rho(S_n)$ (10^3 MeV^{-1})	Shift Value δ	$\rho(S_n)$ (10^3 MeV^{-1})
-0.1	6.72(445)	0.13	5.05(337)
0.0	5.94(395)	0.2	4.63(311)
0.1	5.24(349)	0.3	4.09(285)
0.12	5.12(330)	0.4	3.60(259)

5.4 Simultaneously-Extracted Nuclear Level Density and γ-ray Strength Function

The NLD and γSF as functional forms are simultaneously extracted from the analysis region, $(E_{x,min}, E_{x,max}) = (4.09, 5.49)$ MeV and $E_{\gamma,low} > 1.890$ MeV, by the method Schiller *et al.* [9] developed, as discussed in Chapter 4. In Fig. 5.8, the product of the experimental NLD and γSF: $P(E_i, E_\gamma) \propto \rho(E_f)\mathscr{T}(E_\gamma)$ is plotted as a function of E_γ for several excitation energy bins between 4.09-5.49 MeV and compared to the theoretical expectation of the product

Table 5.5: Giant Electric Dipole Resonance Parameters (GEDR) for ^{93}Sr reported by RIPL3 [36] and average total radiative width estimated from global systematics of ^{86,88}Rb, ^{85,87,88,89}Sr, ^{90}Y, and $^{91-95,97}$Zr [36].

Γ_{E1} (MeV)	E_{E1} (MeV)	σ_{E1} (MeV)	$\langle\Gamma_\gamma\rangle$ (meV)
4.50	16.84	206.0	120(32)

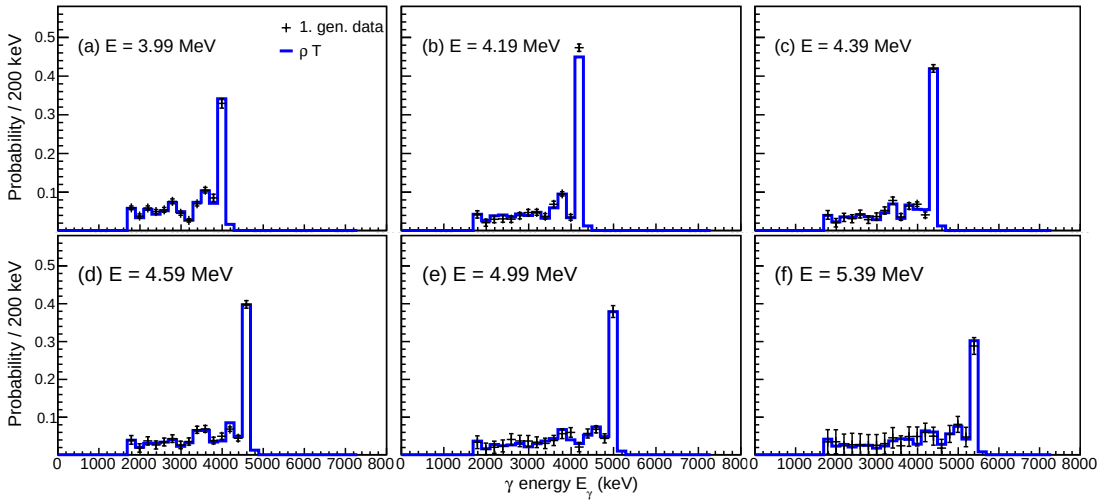
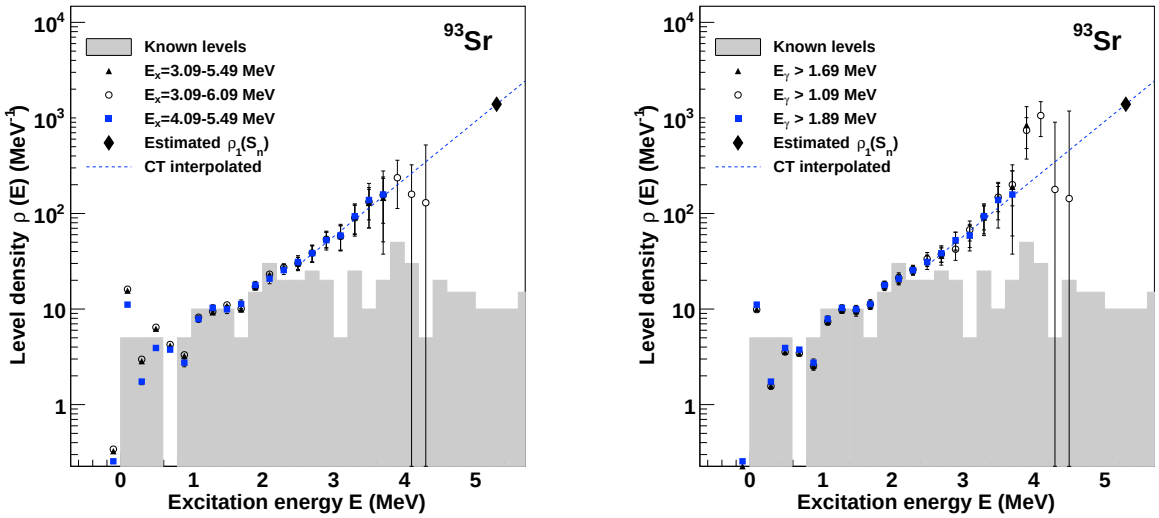


Figure 5.8: Comparison between experimental (black crosses) and theoretical (blue line) primary γ spectra from the analysis region 4.09-5.490 MeV.

given by the expression Eq. 4.22. The comparison shows increasing agreement between the observed and expected value at excitation energies near the S_n value; however beyond $S_n = 5.288$ MeV, the uncertainties are larger due to lower statistics at higher excitation energies.

5.5 Normalizing the Nuclear Level Density

The level density of known levels for ^{93}Sr continues to increase until 2 MeV, where the level density plateaus. The first 20 states serve as a normalization point at low energy for the extracted NLD. For the analysis featured in this work, a region representative of the quasi-continuum was determined by examining several excitation energy windows as shown in Fig. 5.9a, comparing a large energy region from 3.05-6.09 MeV to two narrower

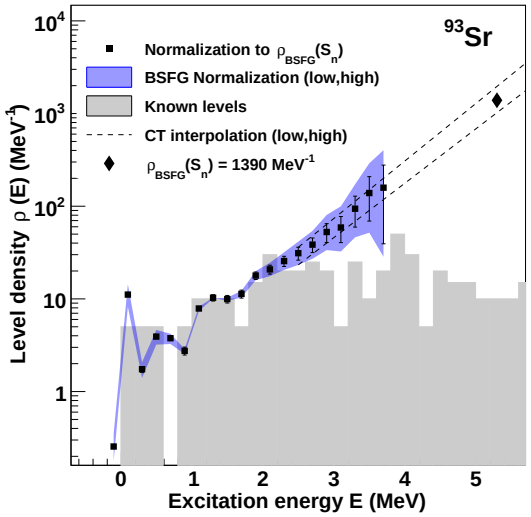


(a) Excitation energy threshold

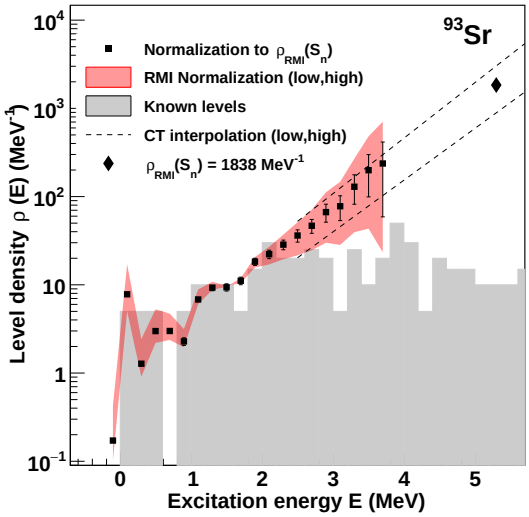
(b) γ-ray energy threshold

Figure 5.9: Excitation energy regions (left) are compared to exclude potentially non-statistical regions and incorrectly-subtracted from analysis. For $(E_{x,min}, E_{x,max}) = (4.09, 5.49)$ MeV, γ-ray energy regions (right) are investigated to exclude potentially incorrectly-subtracted regions from analysis.

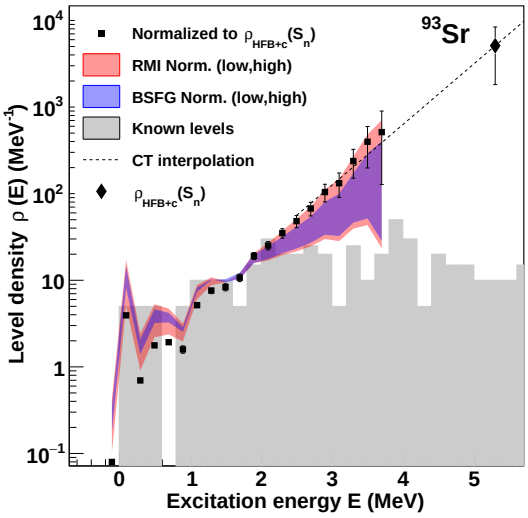
regions. The largest region includes both a portion of the continuum as well as levels strongly populated by β decay at around 3.8 MeV compared to the 3.09-5.49 MeV region which excludes the continuum. The analysis region of 4.09-5.49 MeV excluded strongly β-populated levels, as well as the continuum, where counting statistics were relatively low. In addition to selecting a region representative of the quasi-continuum, a E_γ threshold was likewise determined as shown in Fig. 5.9b, in order to exclude non-statistical γ rays. Figure 5.9b compares the three E_γ thresholds, of which the lowest at $E_\gamma = 1.09$ MeV excludes a valley at $E_x = 2.89 - 5.69$ MeV and a hole at 1.49 MeV, and the second threshold at 1.69 MeV excludes the second valley at $E_x = 5.69 - 7.49$ MeV and a hole at 4.09 MeV. The two holes agree with levels and γ rays reported by ENSDF; in other words, the three levels at 1.49 MeV do not emit primaries within the energy range of 0.89±0.20 MeV, and the six levels at 4.09 MeV emit primaries of energies greater than 1.50 MeV. The only exceptions in this data are a 473.8(6) keV γ with a relative intensity of 5.1(22)% and a 1359.92(16) keV γ with a relative intensity of 37(3)% from a level at 4.10 MeV. Regarding the two valleys in the data, the levels and primaries reported by ENSDF indicate that counts were expected in the first valley, while there are no reported primaries around 1.29 MeV emitted by levels ≥5.69 MeV. For these reasons, the E_γ threshold was increased to 1.89 MeV in order to exclude low-energy transitions that were not sufficiently subtracted in the primary γ extraction process.



(a) BSFG Normalization Limits



(b) RMI Normalization Limits



(c) NLD Normalization Approaches

Figure 5.10: Three normalization approaches are compared. The NLD in the top-left panel is normalized with BSFG-estimated $\rho(S_n)$ including upper and lower estimates. The NLD in the top-right panel is normalized with RMI estimated $\rho(S_n)$ including upper and lower estimates. The dashed lines represent an extrapolation between the extracted NLD (black square) and the estimated $\rho(S_n)$ (black diamond) using the CT model. Bottom panel includes both the BSFG and RMI approaches and the NLD normalized using a microscopic model approach (black squares).

The second normalization point is the total level density at S_n, which was estimated by a phenomenological and microscopic model approach, both of which are anchored to experimental nuclear data. In the case of the phenomenological approach, the estimated $\rho(S_n)$ for ^{93}Sr was obtained by a fit of the CT, BSFG, and RMI model to experimental total level densities for ^{86,88}Rb, ^{85,87,88,89}Sr, ^{90}Y, and $^{91-95,97}$Zr [36]. Estimated values of $\rho(S_n)$ (Table 5.2) and D_0 (Table 5.3) are used to normalize the NLD and uncertainty upper and lower limits were determined by normalization to the upper and lower estimated $\rho(S_n)$ value. Of the listed phenomenological approaches, the energy-dependent spin-cutoff parameter σ used in the BSFG and RMI models is more appropriate than the constant σ of the CT model approach. The level densities shown in Fig. 5.10c are the results yielded from the BSFG and RMI model approaches to estimating the $\rho(S_n)$. In Fig. 6.5a, the black squares in the blue shaded region represent a normalization at high excitation energies to $\rho(S_n) = 1.39 \times 10^3$ MeV^{-1}, which was estimated using the spin-cutoff parameter of the BSFG model from Reference [32]. The blue shaded region represents the NLD normalized to $\rho(S_n) = 1.96 \times 10^3$ MeV^{-1} and $\rho(S_n) = 1.02 \times 10^3$ MeV^{-1}, the upper and lower estimates using the BSFG model approach. In Fig. 6.5b, the black squares in the red shaded region represent a normalization to $\rho(S_n) = 1.84 \times 10^3$ MeV^{-1} obtained using σ of the RMI model [30]. Similar to the previous approach, the red shaded region represents the NLD normalized to the upper and lower estimates using the RMI approach. In both normalization approaches an extrapolation using the CT model is applied between the last data point and the estimated $\rho(S_n)$, shown by a dashed line. The upper and lower normalization of the BSFG is more constraining than the RMI approach as shown in Fig. 5.10c, which is also reflected in the normalization of the γSF and the neutron-capture cross section. In addition to phenomenological approaches, the HFB + c model was used to estimate $\rho(S_n) = 5.12 \times 10^3(330)$ MeV^{-1}. The normalized NLD, shown in Fig. 5.10c by black squares, was obtained using the microscopic model approach and is within the upper limits of the RMI approach shown by the red shaded region.

The obtained normalized NLD is for ^{93}Sr produced by β decay of ^{93}Rb; however, ^{93}Sr β decays to ^{93}Y, and thus consequently measurements are contaminated by the decay daughter by approximately 4%. Contamination was removed from the measurement through subtraction of the decay daughter TAS spectrum from the total measured TAS spectrum. Figure 5.11 compares the extracted NLD if contamination is removed (black circles) or included (red squares), and it was determined that the difference in the extracted NLD's was insignificant for $E_x > 2.0$ MeV. Contamination would have played a more significant role if the decay rate of the decay daughter was higher or if the signal from the decay daughter could not be removed by the use of the tape station with sufficient frequency.

5.6 Normalizing the γ-ray Strength Function

The slope of the γSF is dependent on the slope of the NLD, which is described by the coefficient α in the expression for the transmission coefficient ($\mathscr{T}(E_\gamma) \propto f(E_\gamma)$)

$$\tilde{\mathscr{T}}(E_i - E_\gamma) = B\mathscr{T}(E_\gamma)e^{\alpha E_\gamma}, \tag{5.2}$$

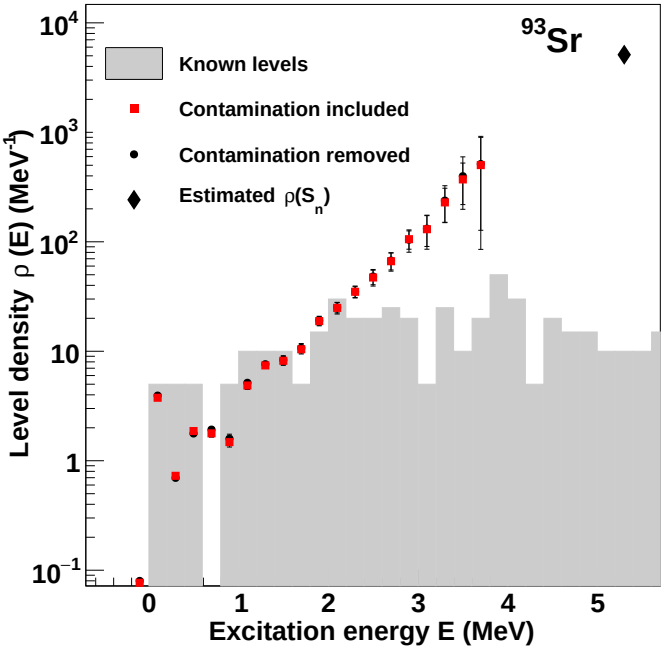


Figure 5.11: Contamination from the decay daughter ^{93}Y contributes approximately 4% to the measured activity. Inclusion of the contamination is compared to its removal yielding a difference between the measurements for E_x >1.89 MeV that is statistically insignificant.

which was determined from the NLD normalization. In addition, an estimated $\langle\Gamma(S_n)\rangle$ was used to determine the coefficient B, or the absolute magnitude of the γSF. However, the NLD is also dependent on angular momentum, and as β decay is a highly selective process, a narrow window of spins is accessed in the daughter nucleus of ^{93}Sr. Consequently, the limited spin population affects the slope of the NLD, and thus the slope of the γSF. To include this into the analysis, the NLD needs to be additionally normalized using a reduction factor representative of the spins populated.

5.6.1 Limited Spin Population from the Initial β Decay

The β decay of ^{93}Rb populates three spins: 3/2, 5/2, and 7/2, and only negative parity states. After the initial states are populated, in the case of $E1$ transitions, the emission of a β-delayed γ results in expanding the spin window of accessed states by $1\hbar$, so that the states populated are $1/2 \leq J \leq 9/2$ and of both parities. An assumption made in this work is that the spin distribution from β decay is the same at each excitation energy. In addition, as ^{93}Sr is not near either the proton or neutron shell closures, parity distribution is assumed to be equal at each excitation energy. The spin distribution for ^{93}Sr using tabulated theoretical

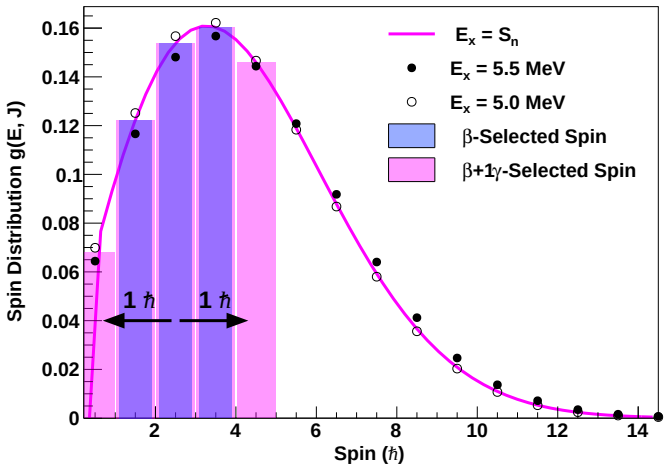


Figure 5.12: Distribution of spins based on tabulated HFB + c NLD from TALYS [20, 42] for ^{93}Sr around the neutron separation energy S_n = 5.288 MeV. By fitting Eq. 2.22 to $g(5.0\text{ MeV}, J)$ and $g(5.5\text{ MeV}, J)$, an energy-dependent spin-cutoff $\sigma(E)$ was obtained. Eq. 2.22 was fit to tabulated NLD values at lower excitations to develop a relationship between $\sigma(E)$ and excitation energy, which was fit with a linear equation to determine $\sigma(S_n) = 3.77$ for ^{93}Sr. The shaded portion in azure beneath the curve at S_n represents the spins populated by β decay of ^{93}Rb. Populated states in ^{93}Sr then initially decay by a dipole transition which expands the spin window by $1\hbar$, shown in magenta. The shaded portion represents 64% of the total NLD at S_n.

NLD values from Reference [42] is illustrated in Fig. 5.12, where distributions for E_x =5.0 and 5.5 MeV are shown with open and closed circles, respectively. The azure shaded bars (appears purple due to overlap) represent the spins populated by β decay and the magenta shaded bars represent a dipole transition from the initial β-populated state. The tabulated theoretical NLD values at several excitation energies were fit using Eq. 2.22 to determine the spin-cutoff parameter $\sigma(E)$. A linear fit was then applied to the spin-cutoff parameter as a function of excitation energy to determine $\sigma(S_n)$ used in calculating the spin distribution at $E_x = S_n$ shown by the magenta curve. For the spins populated by $\beta + 1\gamma$, the estimated percentage is 64%. In comparison, the phenomenological approaches yielded similar NLD reductions of 67% for the BSFG model approach and 52% for the RMI model approach. The NLD is then normalized at S_n with a reduced level density and a reduced number of discrete levels at low energies to determine the coefficient α, thus the slope of the γSF.

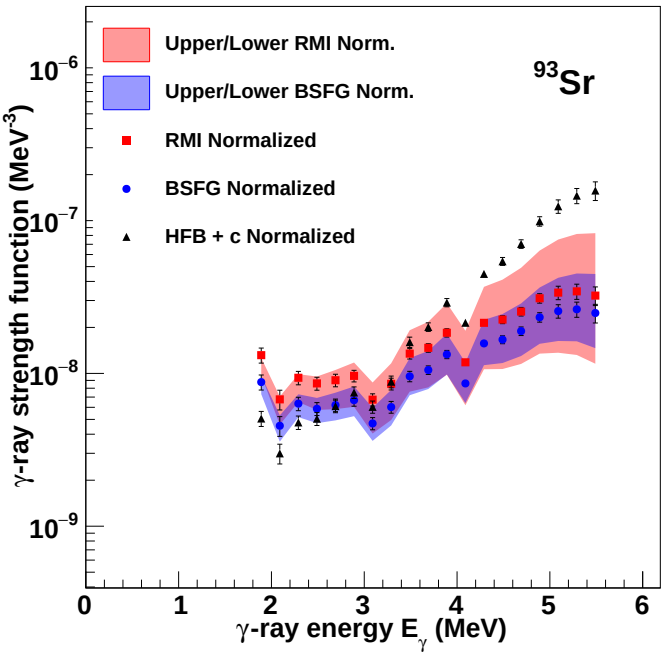


Figure 5.13: γSF normalized with estimated normalization parameters obtained from χ^2 minimization fit of phenomenological models to semi-empirical data and microscopic model approaches. The shaded regions represent upper and lower limits of the NLD normalization for the BSFG and RMI model approaches.

5.6.2 Additional Normalization to Known Photoabsorption Data

The neutron resonance parameters of neighboring stable Rb, Sr, Y, and Zr were used to estimate the average total radiative width of ^{93}Sr. An estimate was obtained from a linear fit of known $\langle\Gamma_\gamma\rangle$ values as a function of mass number A shown in Fig. 2.12. The extracted γSF of ^{93}Sr in Fig. 5.13 is initially normalized to the estimated value $\langle\Gamma_\gamma\rangle$=120(32) meV. The blue circles correspond to the BSFG model approach and the blue shaded region to the associated upper/lower limits obtained from normalizing the NLD to the upper(lower) estimated $\rho(S_n)$. Similarly, the red squares correspond to the RMI model approach and the red shaded region to the associated upper/lower limits of the NLD normalization. The black triangles of the steeper-sloped γSF correspond to the HFB + c model approach. As the γSF was normalized using an estimated $\langle\Gamma_\gamma\rangle$, additional normalization to (γ,n) data for ^{88}Sr was performed in order to give greater confidence to the estimated $\langle\Gamma_\gamma\rangle$. Several assumptions are made in this work, including that the neutron resonance parameters of ^{93}Sr can be estimated from stable nuclei and that the γSF is of similar magnitude to the last stable Sr isotope 5 nuclei away. However, unstable nuclei are unlikely to resemble stable nuclei, and

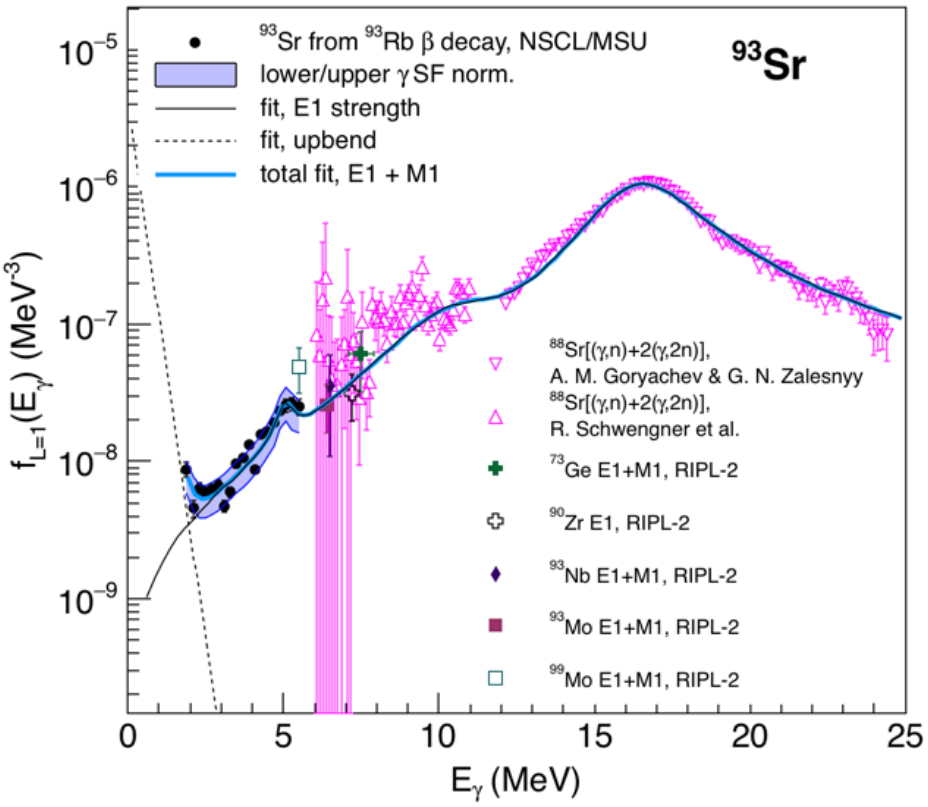


Figure 5.14: The extract γSF of this work (black circles) is normalized with an estimated $\langle\Gamma_\gamma\rangle$=120(32) meV and compared to ^{88}Sr(γ,n) data from Ref. [63] near the GDR (upward triangles) and Ref. [92] near the neutron separation energy of ^{88}Sr (downward triangles). An $E1$ GLO function (black line) fit to ^{93}Sr data from 5-25 MeV and ^{88}Sr(γ,n) data as well as an $M1$ upbend function fit to ^{93}Sr data from 0.1-5 MeV. The combined fit of the $E1$ and $M1$ strength over an energy range of 1.85 to 25 MeV is shown a cyan line. ^{93}Sr data and ^{88}Sr(γ,n) data are compared the $E1$ and $M1$ strengths of neighboring nuclei.

thus additional nuclear data is necessary in this region to improve the normalization.

The photoabsorption cross section, $\sigma_{\gamma,n}$, of ^{88}Sr was measured at around the GDR from 11 MeV to 25 MeV by A. M. Goryachev and G. N. Zalesnyy [63], as well as at 5.05 to 12.75 MeV, which borders the neutron separation energy $S_n = 11.112$ MeV, by R. Schwengner *et al.* [92]. In Fig. 5.14, the $\sigma_{\gamma,n}$ converted into a γSF is plotted along with the combined $E1$ and $M1$ strength for several neighboring nuclei: ^{73}Ge, ^{90}Zr, ^{93}Nb, and ^{93,99}Mo. The γSF of ^{93}Sr obtained from the NLD normalization with the BSFG model approach is shown with black circles. The blue shaded region here presents the γSF normalized to upper(lower)

uncertainty of the $\langle\Gamma_\gamma\rangle$. A GLO function with two pygmy functions was fit to the photoabsoption data and the ^{93}Sr data shown by the solid black line representing the $E1$ strength. The first pygmy is located at 11 MeV, i.e., the neutron separation energy of ^{88}Sr, which was initially proposed by Schwengner *et al.* [92]. The second pygmy is suggested to be at the neutron separation energy of ^{93}Sr. In addition to the $E1$ strength, an upbend function in the form of $y = Ae^{Bx}$ was fit to ^{93}Sr data at low E_γ shown as a dashed curve. The sum of the $E1$ strength and upbend fit is illustrated with a cyan curve. In comparison, a Single Particle M1 strength function was also considered and is discussed in Chapter 6 with respect to the impact of an upbend on the neutron-capture cross section. Furthermore, the impacts of the NLD and γSF normalization approaches are discussed in Chapter 6.

Chapter 6

Neutron-Capture Cross Section Calculations

The nuclear level density (NLD) and γ-ray strength function (γSF) extracted from experimental data for ^{93}Sr using the β-Oslo Method are key components in calculating the neutron-capture cross section. These statistical properties, along with an optical model potential (OMP) are input parameters in the Hauser-Feshbbach Formalism which is utilized by TALYS to calculate neutron-capture cross sections [20]. The ^{92}Sr(n,γ) cross section has not been experimentally measured in the facilities we have today; however, compared to previous theoretical determinations of this cross section, this work presents a experimentally-constrained cross-section calculation. In this chapter, the newly determined experimental ^{92}Sr(n,γ) cross section, using the β-Oslo Method, is compared to theoretical uncertainty in order to determine the impact of the reduction in errors.

6.1 Theoretical Reaction Calculation

The default theoretical ^{92}Sr(n,γ) cross section calculated with TALYS utilizes available phenomenological models. Default input parameters include the constant temperature plus Fermi gas model for the NLD, the Kopecky-Uhl generalized Lorentzian for the $E1$ strength, a $M1$ strength as a function of the $E1$ strength: $f_{E1}/(0.0588A^{0.878})$, and a global Koning and Delaroche OMP [20]. Additionally, the microscopic NLD and γSF models, listed in Table 6.1, were varied to determine the uncertainty of the theoretical cross section. The default parameter settings represent an theoretical upper-bound limit of the cross section calculation and is shown in Fig. 6.1. The lower-bound was obtained using a combination of the Hartree-Fock-Bogoliubov (Skyrme force) + combinatorial method [42] for the NLD and Hartree-Fock QRPA $E1$ strength with an $M1$ as a function of f_{E1}. This variation in the cross section is illustrated by the grey shaded region, which is overlapped with the red shaded region representing the variation in microscopic models. Along with the available microscopic models, TALYS includes three additional phenomenological NLD models, the

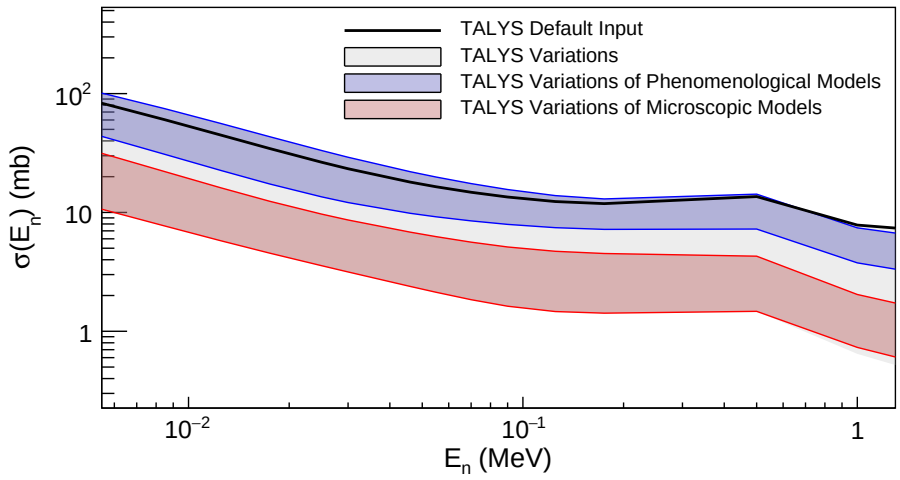


Figure 6.1: Theoretical cross section of ^{92}Sr(n,γ)^{93}Sr calculated using various phenomenological and microscopic NLD and γSF models. The black line represents the default TALYS inputs used to calculate the cross section, while the blue shaded region represents variations of phenomenological models and the red shaded region represents variations of microscopic models.

CT, BSFG, and GSM, as well as an additional γSF model, the BA model, which were varied, resulting in the blue shaded region in Fig. 6.1. By varying these possible theoretical representations of the NLD and γSF for ^{93}Sr, a wide range of cross section values between thermal and 1 MeV neutron energies was determined such that the percent difference between the upper(lower)-bound and the average value is 81%.

Table 6.1: Available microscopic models for the NLD and γSF in TALYS [20].

NLD	γSF
Hartree Fock using Skyrme force [42]	Hartree-Fock BCS [36]
Hartree-Fock-Bogoliubov (Skyrme force) + combinatorial method [42]	Hartree-Fock-Bogoliubov [36]
Temperature-dependent Hartree-Fock-Bogoliubov (Gogny force) [43]	Hartree-Fock QRPA [93]

6.2 Final Calculation of ^{92}Sr(n,γ) Cross Section and Reaction Rate

The extracted NLD and γSF from experimental TAS and γ-ray spectra for ^{93}Sr were normalized using various approaches, due to the lack of experimentally-measured nuclear level density parameters and neutron resonance parameters. NLD normalization approaches include two methods using phenomenological models: (1) a fit of BSFG-predicted total level densities to semi-empirically determined total level densities of stable Rb, Sr, Y, and Zr to estimate the $\rho_{BSFG}(S_n)$ for ^{93}Sr and (2) a fit of RMI-predicted total level densities to semi-empirically determined total level densities to estimate the $\rho_{RMI}(S_n)$ for ^{93}Sr. A third NLD normalization approach utilized theoretical tabulated level densities for ^{93}Sr by Goriely *et al.* [42] anchored to known discrete levels. The γSF is normalized to an estimated $\langle\Gamma_\gamma\rangle$=120(32) meV. Furthermore, the γSF is fit with either an $E1$ GLO + $M1$ upbend function or an $E1$ GLO + $M1$ single-particle function. Lastly, to calculate the neutron-capture cross section using the Hauser-Feshbach Formalism, an OMP is selected from the available models in TALYS. As the OMP is not experimentally obtained using the β-Oslo Method, it may introduce an additional systematic error; however, in the Fig. 6.2 for a single NLD and γSF normalization, the OMP was varied using either the global Koning and Delaroche OMP or JLM OMP. The resulting difference between the calculated cross sections is on average 21%, which is a factor of four smaller than the potential variation of theoretical NLD and γSF models.

The uncertainty associated with the estimated $\langle\Gamma_\gamma\rangle$ also introduces a systematic uncertainty to the calculated cross section shown as a blue shaded region in Fig. 6.3. The cross-hair points represent the cross section obtained from the BSFG, GLO + M1 upbend and global Koning and Delaroche OMP model approaches. Additionally, from the γSF was normalized to the estimated neutron resonance parameter $\langle\Gamma_\gamma\rangle$=120 meV. The upper- and lower-bound cross sections as the boundary of the blue shaded region are the results of the γSF normalized to $\langle\Gamma_\gamma\rangle_{up}$=152 meV and $\langle\Gamma_\gamma\rangle_{low}$=88 meV shown as the blue shaded region. On average, the difference between normalizations are an upper and lower difference of 6.7% and 28.6%, respectively, which are factor of 12 and 3 smaller than the theoretical variations the cross section shown as the grey shaded region. However, the choice of OMP and the estimated $\langle\Gamma_\gamma\rangle$ value are not the only source of systematic error. For instance, the NLD normalization approach not only affects has multiplicative effects on the uncertainty of the γSF and the neutron-capture cross section $\sigma_{\gamma,n}$.

6.3 Propagation of Systematic Error

The BSFG and RMI model approaches lead to a larger uncertainty due to the χ^2 minimization fit to semi-empirical total level densities such that the upper and lower limits of the BSFG approach on the NLD are 27.1% and 18.2%, respectively, and upper and lower limits of the BSFG approach on the NLD are 41.4% and 43.0%, respectively. Each of these

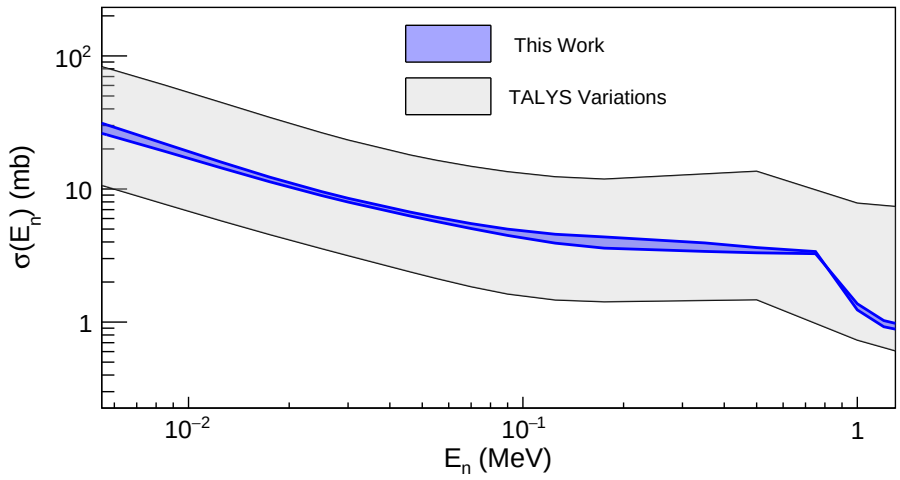


Figure 6.2: Experimentally-determined cross section of ^{92}Sr(n,γ)^{93}Sr (in blue) obtained from the BSFG and GLO + M1 upbend model approaches. The upper bound of the cross section was obtained using the global Koning and Delaroche OMP, and the lower bound was obtained using the JLM OMP. The theoretical calculations of the cross section using TALYS are also shown (in grey). The percent difference on average is 21%

approaches were applied to the extracted NLD and resulted in the calculated cross section obtained from the BSFG approach shown as a blue shaded region in Fig. 6.4a and the calculated cross section obtained from the RMI approach shown as a red shaded region in Fig. 6.4b. In both cases the γSF was normalized to $\langle\Gamma_\gamma\rangle$=120 meV and the subsequent γSF was fit with an $E1$ GLO function plus a $M1$ upbend and a pygmy resonance at approximately 5 MeV and 11 MeV. The cross sections shown as cross-hair points are constrained by the estimated uncertainty of $\rho_{BSFG}(S_n)$ and $\rho_{RMI}(S_n)$, resulting an upper and lower limits of 21.2% and 46.6%, respectively, for the BSFG model approach and 26.9% and 56.9%, respectively, for the RMI approach. In the same manner, the cross sections obtained from the BSFG and RMI model approaches shown in Fig. 6.4c and 6.4d were obtained from a γSF normalization to an $E1$ GLO function plus a $M1$ single-particle strength. This combination of normalization approaches yielded upper and lower limits of 27.9% and 19.3%, respectively, for the BSFG model approach and 42.6% and 40.9%, respectively, for the RMI approach. While the shape of the neutron capture cross section does not vary between normalization approaches, the magnitude significantly changes between the choice of NLD normalization as shown by the combined plots of Fig. 6.4.

The sensitivity of the calculated neutron-capture cross section as a function of the NLD and γSF normalization is shown Fig. 6.5, where the phenomenological NLD model approaches are compared to the microscopic NLD model approach. The cross sections shown were obtained using the NLD obtained using the BSFG, RMI, and HFB + c model ap-

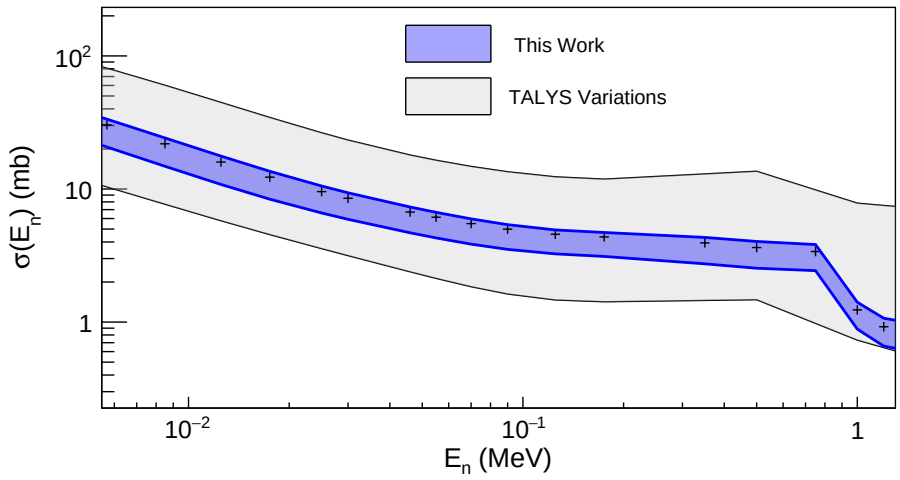
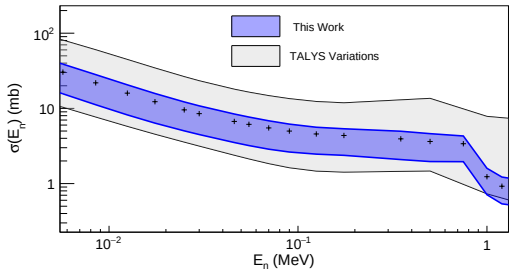
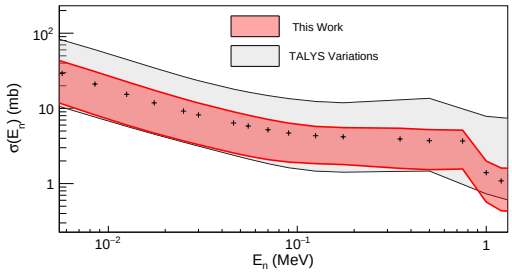


Figure 6.3: Experimentally determined cross section of ^{92}Sr(n,γ)^{93}Sr (in blue) obtained from the BSFG, GLO + M1 upbend and global Koning and Delaroche OMP model approaches. The cross-hair points represent the cross section obtained from the experimentally extracted γSF normalized to the estimated $\langle\Gamma_\gamma\rangle$=120 meV. The upper bound of the cross section was obtained using the upper limit of the γSF (to $\langle\Gamma_\gamma\rangle_{up}$ = 120+32 meV) and the lower limit was obtained using the lower limit of the γSF (to $\langle\Gamma_\gamma\rangle_{low}$ = 120-32 meV). The resulting upper and lower uncertainties on average due to the systematic error of the estimated $\langle\Gamma_\gamma\rangle$ are 6.7% and 28.6%, respectively.

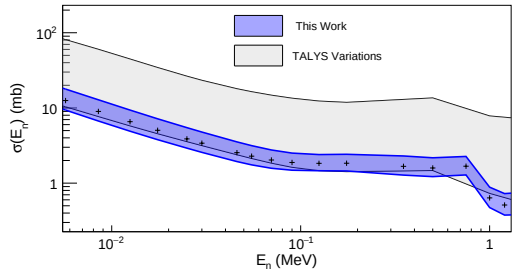
proaches and the γSF obtained using the $E1$ GLO + $M1$ upbend approach in Fig. 6.5a and the $E1$ GLO + $M1$ single-particle approach in Fig. 6.5b. In the case where the extracted γSF was fit to an M1 strength with an upbend, the NLD normalization approach did not have a signifiant impact such that the difference between the BSFG and RMI model approach is 9.7% and the difference between the BSFG and HFB + c model approach is 33.5%. In contrast, the $E1$ GLO + $M1$ single-particle approach resulted in cross sections that varied additionally depending on the NLD normalization approach such that the BSFG and RMI model approach is 24.8% and the difference between the BSFG and HFB + c model approach is 100.8%. While this combination of approaches produced some of the largest systematic uncertainties, the uncertainty associated with the experimentally determined ^{92}Sr(n,γ) cross section obtained from various normalization approaches is 1.5 to 4 factors lower than uncertainty of theoretical predictions of the cross section, and is even 12 factors lower in the case of the uncertainty of the $\langle\Gamma_\gamma\rangle$ value. This gives great confidence to the β-Oslo Method to be used to experimentally determine statistical properties for neutron rich nuclei when additional nuclear data is unavailable.



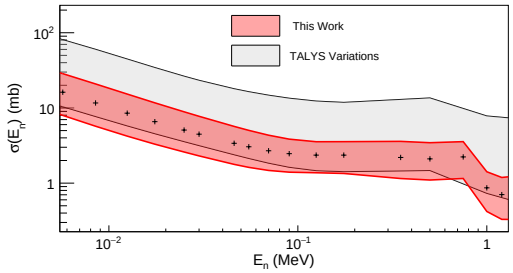
(a) BSFG Normalization, $E1$ GLO + $M1$ Upbend Normalization



(b) RMI Normalization, $E1$ GLO + $M1$ Upbend Normalization

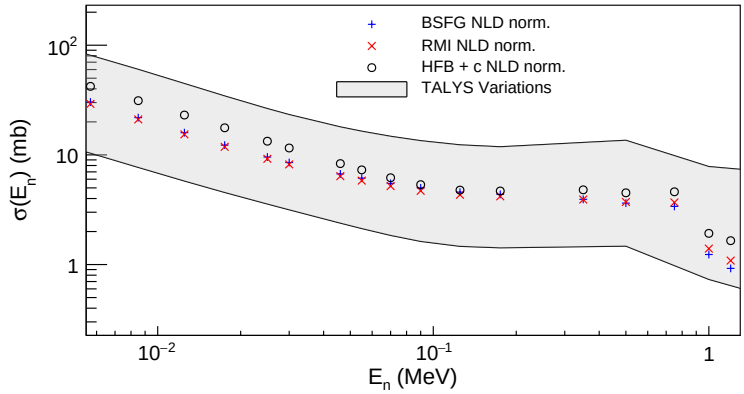


(c) BSFG Normalization, $E1$ GLO + $M1$ Single-particle Normalization

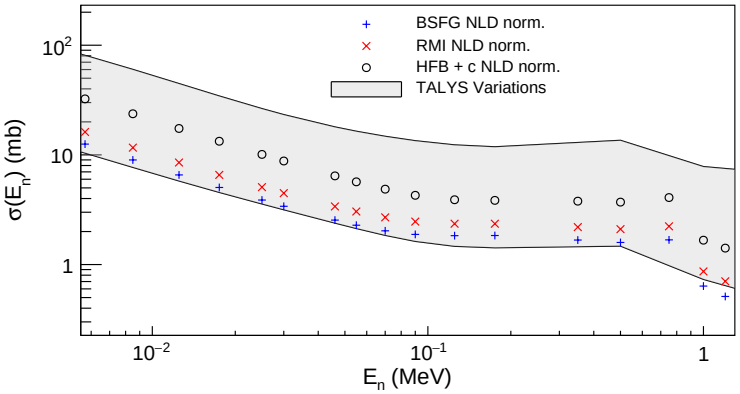


(d) RMI Normalization, $E1$ GLO + $M1$ Single-particle Normalization

Figure 6.4: ^{92}Sr(n,γ) cross section plotted as a function of neutron energy obtained from the upper- and lower-bound estimates of $\rho(S_n)$ for the BSFG model (a & c) and RMI model (b & d) approaches. The cross section determined from the BSFG and RMI estimated $\rho(S_n)$ is shown as cross-hair points on all plots. Cross sections in plots (a) and (b) are the result of a $E1$ GLO + $M1$ upbend fit of the extracted γSF, while plots (c) and (d) are the results of a $E1$ GLO + $M1$ single-particle fit. The upper and lower limits of the BSFG model approach with an upbend fit are, on average, 21.2% and 46.6%, respectively; the upper and lower limits of the BSFG model approach with a $M1$ single-particle fit are, on average, 27.9% and 19.3%, respectively. For the RMI model approach, an upbend fit resulted in upper and lower limits of, on average, 26.9% and 56.9%, respectively, while a $M1$ single-particle fit resulted in limits of 42.6% and 40.9%, respectively.



(a) $E1$ GLO + $M1$ Upbend Normalization



(b) $E1$ GLO + $M1$ Single-particle Normalization

Figure 6.5: ^{92}Sr(n,γ) cross section obtained from (a) an $E1$ GLO + $M1$ upbend fit and (b) an $E1$ GLO + $M1$ Single-particle fit of the extracted γSF. The cross section obtained utilizing a BSFG model approach is represented in both γSF normalizations by blue cross-hair points. Similarly, the cross section obtained utilizing an RMI model approach is represented by red x's. In comparison, the HFB + c approach is represented by open circles.

Chapter 7

Conclusion

7.1 Summary

Neutron-induced reaction cross section data for exotic nuclei far from stability are necessary for fundamental nuclear physics applications, reactor design, and the U.S. science-based Stockpile Stewardship mission, alike. For-neutron rich nuclei close to the neutron drip line, the N/Z ratio and the Q_β-value both increase, while, the neutron separation energy becomes smaller, and thus βn becomes a more dominant decay mode. Furthermore, direct cross-section measurements are experimentally inaccessible for short-lived fission fragments, as is the case for ^{92}Sr, and thus indirect methods are often required in order to determine statistical nuclear properties of such nuclei. In this work, the indirect method known as the β-Oslo Method was utilized to experimentally constrain the ^{92}Sr(n,γ)^{93}Sr cross section. Through β decay, highly excited states in ^{93}Sr, both near as well as above the neutron separation energy, were populated, which subsequently emitted γ rays to levels below, acting as a probe of the nuclear structure. The nuclear level density (NLD) and γ-ray strength function (γSF) were extracted from primary γ rays which were obtained from experimentally-measured γ-ray and total absorption spectra.

The NLD and γSF calculated in this work, extracted using the β-Oslo Method from an excitation energy range of 4.09 MeV to 5.49 MeV and from γ-ray energies greater than 1.89 MeV, are initially functional forms, which rely on external nuclear data such as known discrete levels, the average s-wave neutron spacing (D_0), and the average total radiative width ($\langle\Gamma\rangle$), to determine the most physical slope and magnitude. These normalization parameters are generally unavailable for neutron rich nuclei, other than for low lying discrete levels, however, as is the case for ^{93}Sr. The NLD and γSF were therefore normalized by employing various approaches utilizing experimental and semi-empirical values of neighboring stable nuclei to estimate the unavailable neutron resonance parameters of ^{93}Sr. Estimates of the neutron resonance parameters employed both phenomenological and microscopic models, which resulted in a systematic uncertainty when calculating the neutron-capture cross section using the Hauser-Feshbach formalism. The use of one normalization approach over another,

however, did not affect the general shape of the neutron-capture cross section. For neutron energies of 50 keV to 1 MeV, the resulting cross section of each normalization approach was within the theoretically predicted limits. The uncertainty in the experimentally-constrained capture cross section was reduced by a factor of 2 to 4 from a theoretical limit of 82% from the mean cross section value to an upper and lower uncertainty of 21.2% and 46.6%, respectively, by using the β-Oslo Method. Though external nuclear data was unavailable and the analysis depended on various approaches to normalize the experimentally-obtained statistical properties, a broader view of the impact of normalization techniques on the neutron-capture cross section was obtained. As the need to remedy nuclear data deficiencies with accurate neutron-capture cross section datasets in the neutron-rich region of the Table of Isotopes is a critical need for applications including reactor design, nucleosynthesis, and U.S. science-based Stockpile Stewardship, the analysis presented in this work represents a robust approach which can be employed in future fundamental nuclear physics research in order to determine statistical nuclear properties and neutron-capture cross sections with lower uncertainties than associated with using conventional purely theoretical-based approaches.

7.2 Outlook

The successful determination of the neutron-capture cross section for ^{92}Sr using the β-Oslo Method as presented in this dissertation has had a two-fold effect in addressing the imperative need for nuclear data deficiencies for short-lived fission product burn-up in high neutron flux environments. Fundamentally, important experiments such as these reassert the need to continue and encourage future analysis using the β-Oslo Method and other indirect techniques in investigating key nuclear inputs, such as neutron-capture cross sections of fission fragments. This work was motivated by the nuclear data needs of the U.S. Stockpile Stewardship Program in the modeling of nuclear weapons performance and physics without nuclear explosive testing, which in turn is part of the U.S. strategic position in assurance of allies, verification of arms control agreement, and is in support of the Treaty on the Non-Proliferation of Nuclear Weapons (NPT) regime in capabilities to deter, as well as attribute, proliferation and use should deterrence fail. In addition, this dissertation improved the accuracy of reaction-theory calculations, and thus reduced the uncertainty on the ^{92}Sr(n, γ) cross section. However, greater strides can be made through future experiments utilizing β-delayed neutron emission to additionally constrain nuclear-structure calculations, and thus improve our comprehensive understanding of neutron-induced reactions that are crucial for a wide range of nuclear physics applications, from nuclear energy and astrophysics to U.S. stockpile stewardship and other national security missions.

7.2.1 Future β-Oslo Experiments: ^{93,94,95}Sr(n,γ)

Neutron-capture reactions and β decay of exotic nuclei are particularly relevant to understanding the astrophysical conditions responsible for producing the heaviest elements as well

as reactor design, maintenance, and safety, and ensuring the safety, security, and effectiveness of the U.S. Stockpile under a non-testing regime. As a result, a Lawrence Livermore National Laboratory (LLNL)-led team of scientists was granted Priority 1 acceptance of a submitted proposal to investigate heavier Sr isotopes, such as ^{93,94,95}Sr(n,γ), using the analytical toolsets including those demonstrated in this dissertation. This project will be performed using high intensity radioisotope beams provided by the CAlifornium Rare Isotope Breeder Upgrade (CARIBU) facility at Argonne National Laboratory (ANL) with an anticipated start date sometime in Fall 2020.

The reactions ^{94}Sr(n,γ) and ^{95}Sr(n,γ) are of particular importance, as shown by Fig. 1.4, to understanding the reactions that produce and destroy ^{95}Sr, which is a high-yield fission product. The Priority 1 accepted experiment will utilize beams of ^{94,95,96}Rb ions to produce ^{94,95,96}Sr at the experimental-end-station where emitted γ rays and β particles will be measured by the Summing NaI(Tl) detector (SuN) and a plastic scintillator detector, respectively. A toolkit of methods and techniques presented by this dissertation were developed in the process of determining the neutron-capture cross section for a neutron-rich Sr nuclei using the β-Oslo Method, and will be used for future experiments. This measurement will provide an additional experimental constraint of nuclear fission product properties, which can assist in extrapolating reaction theory to nuclei even farther from stability. In addition, experimentally informed theory supports the development of more reliable and effective nuclear weapons performance modeling simulations to meet the needs outlined by the U.S. Nuclear Posture Review in a non-nuclear testing regime.

7.2.2 β-Delayed Neutron Emission Experiments

A Q_β-value greater than the neutron separation energy is a tell-tale characteristic of a strong β-delayed neutron emission probability. With regard to experimental β-Oslo analysis, this leads to a more challenging analysis as the normalization process is hindered by the unavailability of statistical properties for neutron rich-nuclei, as well as by the contamination from the activity of the $A-1$ daughter in the measurement. The strong βn branch, which in the case of ^{96,97}Rb is greater than 10%, is, however, also an advantage for experimentally determining nuclear structure properties.

As we are interested in the interactions that produce and destroy ^{95}Sr, a future β-delayed neutron experiment would make use of both a beam of ^{96}Rb and ^{97}Rb. The production mechanism will be investigated by measuring the recoil of the daughter ion following the neutron emission: ^{95}Sr+n, and thus determine the energy of the neutron as well as the level it was emitted from, and therefore determining the NLD of ^{95}Sr. The destruction mechanism will be investigated by measuring the recoil of ^{96}Sr following neutron emission. While the CARIBU facility will provide a high intensity beam, the beta-Paul Trap at ANL will enable us to accurately measure the recoil of the daughter ion. The recoil energy and the β-particle energy will be measured using plastic scintillators in a ΔE-E configuration and microchannel plates. In addition, the emitted γ's will be measured with high-purity germanium (HPGe) detectors as previously successful experiments, e.g. β-delayed-neutron studies of ^{135,136}Sb

and ^{140}I by Alan et al. [94]. This alternative path of obtaining a critical piece of nuclear data used in the β-Oslo Method can help to more accurately and reliably determine the neutron-capture cross section.

Bibliography

[1] I. Noddack. "Über das Element 93". In: *Zeitschrift fur Angewandte Chemie* 47 (1934), pp. 653–655.

[2] E. Fermi. "Possible Production of Elements of Atomic Number Higher than 92". In: *Nature* 133 (1934), pp. 898–899.

[3] O. Hahn and F. Strassmann. "Über den Nachweis und das Verhalten der bei der Bestrahlung des Urans mittels Neutronen entstehenden Erdalkalimetalle". In: *Naturwiss.* 27 (1939), pp. 11–15.

[4] O. Hahn and F. Strassmann. "Nachweis der Entstehung aktiver Bariumisotope aus Uran und Thorium durch Neutronenbestrahlung; Nachweis weiterer aktiver Bruchstücke bei der Uranspaltung". In: *Naturwiss.* 27 (1939), pp. 89–95.

[5] L. Meitner and O. R. Frisch. "Disintegration of Uranium by Neutrons: a New Type of Nuclear Reaction". In: *Nature* 143 (1939), pp. 239–240.

[6] L. Meitner and O. R. Frisch. "Products of the Fission of the Uranium Nucleus". In: *Nature* 143 (1939), pp. 471–472.

[7] S. G. Prussin. *Nuclear Physics for Applications*. Germany: Wiley-VCH, 2007.

[8] K. F. Flynn et al. "Distribution of Mass in the Spontaneous Fission of ^{256}Fm". In: *Phys. Rev. C* 5 (1972), p. 1752.

[9] A. Schiller et al. "Extraction of level density and γ strength function from primary γ spectra". In: *Nucl. Instrum. Methods Phys. Res. Sect. A* 447 (2000), p. 498.

[10] A. Spyrou et al. "Novel technique for Constraining r-Process (n, γ) Reaction Rates". In: *Phys. Rev. Lett.* 113 (2014), p. 232502.

[11] Kelsey Davenport. *Nuclear Weapons: Who Has What at a Glance*. URL: `https://www.armscontrol.org/factsheets/Nuclearweaponswhohaswhat`.

[12] Nuclear Science Advisory Committee (NSAC) Isotopes Subcommittee. *Meeting Isotope Needs and Capturing Opportunities for the Future: The 2015 Long Range Plan for the DOE-NP Isotope Program*. 2015.

[13] Arms Control Association. *Treaties and Agreements*. URL: `https://www.armscontrol.org/treaties`.

[14] President George W. Bush. *President Discusses National Missile Defense on December 13, 2001*. URL: https://georgewbush-whitehouse.archives.gov/news/releases/2001/12/.

[15] Secretary of State Press Statement Michael R. Pompeo. *U.S. Withdrawal from the INF Treaty on August 2, 2019*. URL: https://www.state.gov/u-s-withdrawal-from-the-inf-treaty-on-august-2-2019/.

[16] U.S. Depart of Defense. *Nuclear Posture Review*. URL: https://dod.defense.gov/News/SpecialReports/2018NuclearPostureReview.aspx.

[17] Comprehensive Nuclear-Test-Ban Treaty Organization. *27 January 1951- The First Nuclear Test at the Nevada Test Site*. URL: https://www.ctbto.org/specials/testing-times/27-january-1951-the-first-nuclear-test-at-the-nevada-test-site/.

[18] K. S. Krane. *Introductory Nuclear Physics*. New York: John Wiley & Sons, 1988.

[19] Pavel Denissenkov et al. "The impact of (n, γ) reaction rate uncertainties of unstable isotopes near N = 50 on the i-process nucleosynthesis in He-shell flash white dwarfs". In: *J. Phys. G Nucl. Partic.* 45 (2018), p. 055203.

[20] A. J. Koning, S. Hilaire, and M. C. Duijvestijn. "TALYS-1.0". In: *International Conference on Nuclear Data for Science and Technology, EDP Sciences* (2007), pp. 211–214.

[21] N. Bohr. "Neutron Capture and Nuclear Constitution". In: *Nature* 137(3461) (1936), pp. 344–348.

[22] H. A. Bethe. "An Attempt to Calculate the Number of Energy Levels of a Heavy Nucleus". In: *Phys. Rev.* 50 (1936), p. 332.

[23] Data extracted using the ENSDF online data serviced maintained by the NNDC; last updated 2017-09-29. URL: https://www.nndc.bnl.gov/ensdf/ensdf/ensdf.jsp.

[24] C. S. Wu et al. "Experimental Test of Parity Conservation in Beta Decay". In: *Phys. Rev.* 105 (1957), p. 1413.

[25] C. M. Baglin. "Nuclear Data Sheets for A = 93". In: *Nuclear Data Sheets* 112 (2011), pp. 1163–1389.

[26] D. A. Brown et al. "ENDF/B-VIII.0: The 8th major release of the nuclear reaction data library with CIELO-project cross sections, new standards and thermal scattering data". In: *Nuclear Data Sheets* 148 (2018), p. 1.

[27] L. E. Glendenin et al. "Mass distributions for monoenergetic-neutron-induced fission of ^{235}U". In: *Phys. Rev. C* 24 (1981), p. 2600.

[28] T. Ericson. "A statistical analysis of excited nuclear states". In: *Nucl. Phys.* 11 (1959), p. 481.

[29] T. Ericson. "The statistical model and nuclear level densities". In: *Adv. in Phys.* 9 (1960), p. 425.

[30] T. von Egidy and D. Bucurescu. "Systematics of nuclear level density parameters". In: *Phys. Rev. C.* 72 (2005), p. 044311.

[31] T. von Egidy and D. Bucurescu. "Erratum: Systematics of nuclear level density parameters". In: *Phys. Rev. C.* 73 (2006), 049901(E).

[32] T. von Egidy and D. Bucurescu. "Experimental energy-dependent nuclear spin distributions". In: *Phys. Rev. C.* 80 (2009), p. 054310.

[33] A. Gilbert and A. G. W. Cameron. "A composite nuclear-level density formula with shell corrections". In: *Can. J. Phys.* 43 (1965), p. 1446.

[34] A. J. Koning, S. Goriely, and S. Hilaire. "Global and local level density models". In: *Nucl. Phys. A* 810 (2008), pp. 13–76.

[35] A. P. Tonchev et al. "Capture cross sections on unstable nuclei". In: *EPJ Web Conf.* 146 (2017), p. 01013.

[36] R. Capote et al. "RIPL - Reference Input Parameter Library for Calculation of Nuclear Reactions and Nuclear Data Evaluations". In: *Nuclear Data Sheets* 110(12) (2009), pp. 3107–3214. URL: `https://www-nds.iaea.org/RIPL-3/`.

[37] J. Bardeen, L. N. Cooper, and J. R. Schrieffer. "Theory of Superconductivity". In: *Phys. Rev.* 108 (1957), p. 1175.

[38] A. V. Ignatyuk et al. "Density of discrete levels in ^{116}Sn". In: *Phys. Rev. C* 47 (1993), p. 1504.

[39] A. V. Ignatyuk, K. K. Istekov, and G. N. Smirenkin. "Role of collective effects in the systematics of nuclear level densities". In: *Sov. J. Nucl. Phys.* 29 (4) (1979), p. 450.

[40] S. Goriely, F. Tondeur, and J. M. Pearson. "A Hartree-Fock nuclear mass table". In: *Atom. Data Nucl. Data Tables* 77 (2001), p. 311.

[41] P. Demetriou and S. Goriely. "Microscopic nuclear level densities for practical applications". In: *Nucl. Phys. A* 695 (2001), p. 95.

[42] S. Goriely, S. Hilaire, and A. J. Koning. "Improved microscopic nuclear level densities within the Hartree-Fock-Bogoliubov plus combinatorial method". In: *Phys. Rev. C.* 78 (2008), p. 064307.

[43] S. Hilaire et al. "Temperature-dependent combinatorial level densities with the D1M Gogny force". In: *Phys. Rev. C* 86 (2012), p. 064317.

[44] G. A. Bartholomew et al. *Advances in Nuclear Physics.* 1973, p. 229.

[45] D. M. Brink. PhD thesis. Oxford University, 1955.

[46] P. Axel. "Electric dipole ground-state transition width strength function and 7-MeV photon interactions". In: *Phys. Rev.* 126 (1962), p. 671.

[47] M. A. Lone. "Neutron induced reactions". In: *Proc. 4th. Int. Symp.* (1985). J. Kristiak, E. Betak, D. Reidel, Publ. Comp. Dordrecht, Holland, 238 (1986).

[48] "RIPL-1: Handbook for calculations of nuclear reaction data, IAEA, Vienna, Report No. IAEA-TECDOC-1024 (1998); RIPL-2: Handbook for calculations of nuclear reaction data, IAEA, Vienna, Report No. IAEA-TECDOC-1506 (2006)". In: (), pp. 117–138. URL: http://www-nds.iaea.org/RIPL-2/.

[49] L. Crespo Campo et al. "Test of the generalized Brink-Axel hypothesis in ^{64,65}Ni". In: *Phys. Rev. C* 98 (2018), p. 054303.

[50] M. Guttormsen et al. "Validity of the Generalized Brink-Axel Hypothesis in ^{238}Np". In: *Phys. Rev. Lett.* 116 (2016), p. 012502.

[51] C. E. Porter and R. G. Thomas. "Fluctuations of Nuclear Reaction Widths". In: *Phys. Rev.* 104 (1956), p. 483.

[52] Luna Pellegri. "Lecture I - Pygmy Dipole Resonance". Oslo Summer School: Resonances in atomic nuclei. 2019. URL: https://www.mn.uio.no/fysikk/english/research/projects/nuclear-shapes-and-resonances-in-education/summer-schools/oslo-2019/.

[53] A. Van der Woude. "Giant resonances". In: *Prog. Part. Nucl. Phys.* 18 (1987), pp. 217–293.

[54] Y. Suzuki, K. Ikeda, and H. Sato. "New type of dipole vibration in Nuclei". In: *Prog. Theor. Phys.* 83(2) (1990), pp. 180–184.

[55] S. Krewald and J. Speth. "Pygmy dipole resonances". In: *Int. J. Mod. Phys. E* 18(07) (2009), pp. 1425–1451.

[56] K. Heyde, P. von Neumann-Cosel, and A. Richter. "Magnetic dipole excitations in nuclei: Elementary modes of nucleonic motion." In: *Rev. Mod. Phys.* 82(2) (2010), p. 2365.

[57] R. R. Doering et al. "Observation of Giant Gamow-Teller Strength in (p,n) Reactions". In: *Phys. Rev. Lett.* 35 (1975), p. 1691.

[58] J. Kopecky and M. Uhl. "Test of gamma-ray strength functions in nuclear reaction model calculations". In: *Phys. Rev. C* 41 (1990), p. 1941.

[59] S. G. Kadmenskiĭ, V. P. Markushev, and V. I. Furman. In: *Yad. Fiz.* 37 (1983). Sov. J. Nucl. Phys. **37**, 165 (1983), p. 277.

[60] V. M. Kolomietz, V. A. Plujko, and S. Shlomo. "Interplay between one-body and collisional damping of collective motion in nuclei". In: *Phys. Rev. C* 54 (1996), p. 3014.

[61] V. A. Plujko. "An investigation of interplay between dissipation mechanisms in heated Fermi systems by means of radiative strength functions". In: *Nucl. Phys. A* 649 (1999), p. 209.

[62] S. Goriely and E. Khan. "Large-scale QRPA calculation of E1-strength and its impact on the neutron capture cross section". In: *Nucl. Phys. A* 706 (2002), p. 217.

[63] A. M. Goryachev and G. N. Zalesnyy. In: *Vopr. Teor. Yad. Fiz.* 8 (1982), p. 121.

[64] S. S. Dietrich and B. L. Berman. "Atlas of photoneutron cross sections obtained with monoenergetic photons". In: *At. Data Nucl. Data Tables* 38 (1988), p. 199.

[65] Data extracted using the EXFOR online data serviced maintained by the NNDC; last updated 2017-09-29. URL: `https://www.nndc.bnl.gov/exfor/`.

[66] U. Kneissl, H. H. Pitz, and A. Zilges. "Investigation of nuclear structure by resonance fluorescence scattering". In: *Prog. Part. Nucl. Phys.* 37 (1996), p. 349.

[67] J. E. Escher et al. "Compound-nuclear reaction cross sections from surrogate measurements". In: *Rev. Mod. Phys.* 84 (2012), p. 353.

[68] S. Siem and M. Wiedeking et al. "proposal to the iThemba LABS Program Advisory Committee". In: (2014).

[69] A. Ratkiewicz et al. "Towards Neutron Capture on Exotic Nuclei: Demonstrating (d,pγ) as a Surrogate Reaction for (n,γ)". In: *Phys. Rev. Lett.* 122 (2019), p. 052502.

[70] A. J. Koning and J. P. Delaroche. "Local and global nucleon optical models from 1 keV to 200 MeV". In: *Nucl. Phys. A* 713 (2003), p. 231.

[71] J. P. Jeukenne, A. Lejeune, and C. Mahaux. "Microscopic calculation of the symmetry and Coulomb components of the complex optical-model potential". In: *Phys. Rev. C* 15 (1977), p. 10.

[72] S. N. Liddick et al. "Experimental Neutron Capture Rate Constraint Far from Stability". In: *Phys. Rev. Lett.* 116 (2016), p. 242502.

[73] A. C. Larsen et al. "Experimentally constrained (p,γ)^{89}Y and (n,γ)^{89}Y reaction rates relevant to p-process nucleosynthesis". In: *Phys. Rev. C* 93 (2016), p. 045810.

[74] A. Simon et al. "SuN: Summing NaI(Tl) gamma-ray detector for capture reaction measurements". In: *Nucl. Instrum. Methods Phys. Res. Sect A* 703 (2013), p. 16.

[75] D. J. Morrissey et al. "Commissioning the A1900 projectile fragment separator". In: *Nucl. Instrum. Methods Phys. Res. Sect B* 204 (2003), p. 90.

[76] K. Cooper et al. "Extraction of thermalized projectile fragments from a large volume gas cell". In: *Nucl. Instrum. Methods Phys. Res. Sect A* 7663 (2014), p. 543.

[77] K. L. Cooper. "Commissioning and Characterization of the NSCL's Large Volume Linear Gas Cell". PhD thesis. Michigan State University, 2016.

[78] J. C. Hardy et al. "The essential decay of pandemonium: A demonstration of errors in complex beta-decay schemes". In: *Phys. Lett. B* 71 (1977), p. 307.

[79] G. .D. Alkhazov et al. "Experimental test of the ^{145}Gd decay scheme and the decay of pandemonium". In: *Phys. Lett. B* 157 (1985), p. 35.

[80] S. Agostinelli et al. "Geant4 – a simulation toolkit". In: *Nucl. Instrum. Methods Phys. Res. Sect A* 506 (2003), p. 250.

[81] S. J. Quinn. "Capture Cross Sections for the Astrophysical p process". PhD thesis. Michigan State University, 2015.

[82] A. .C. Dombos. "β-Decay Total Absorption Spectroscopy Around A =100-110 Relevant to Nuclear Structure and the Astrophysical r process". PhD thesis. Michigan State University, 2018.

[83] M. Guttormsen, T. Ramsøy, and J. Rekstad. "The first generation of γ-rays from hot nuclei". In: *Nucl. Instrum. Methods Phys. Res. Sect. A* 255 (1987), p. 518.

[84] M. Guttormsen et al. "The unfolding of continuum γ-ray spectra". In: *Nucl. Instrum. Methods Phys. Res. Sect. A* 374 (1996), p. 371.

[85] A. C. Larsen et al. "Analysis of possible systematic errors in the Oslo method". In: *Phys. Rev. C* 83 (2011), p. 034315.

[86] J. Rekstad et al. "A Study of the Nuclear Structure at High Energy and Low Spin". In: *Nucl. Instrum. Methods Phys. Res. Sect A* 703 (2013), p. 16.

[87] A. C. Larsen. "Statistical properties in the quasi-continuum of atomic nuclei". PhD thesis. University of Oslo, 2008.

[88] A. Voinov et al. "γ-ray strength function and pygmy resonance in rare earth nuclei". In: *Phys. Rev. C* 63 (2001), p. 044313.

[89] L. Crespo Campo et al. "Investigating the γ decay of ^{65}Ni from particle-γ coincidence data". In: *Phys. Rev. C* 96 (2017), p. 014312.

[90] M. Guttormsen et al. "Scissors resonance in the quasicontinuum of Th, Pa, and U isotopes". In: *Phys. Rev. C* 89 (2014), p. 014302.

[91] T. .A. Laplace et al. "Statistical properties of ^{243}Pu, and ^{242}Pu(n, γ) cross section calculation". In: *Phys. Rev. C* 93 (2016), p. 014323.

[92] R. Schwengner et al. "Dipole response of ^{88}Sr up to the neutron-separation energy". In: *Phys. Rev. C* 76 (2007), p. 034321.

[93] E. Khan et al. "Photodisintegration of ultra-high-energy cosmic rays revisited". In: *Astropart. Phys.* 23 (2005), p. 191.

[94] B. S. Alan et al. "Beta-delayed-neutron studies of ^{135,136}Sb and ^{140}I performed with trapped ions". In: *Phys. Rev. C* 101 (2019), p. 025806.

Appendix A

Fermi Theory Golden Rule

The decay constant, w, in the limit of first-order perturbation for a weak interaction which converts an initial nuclear state $\Psi_{o,i}$ to a final state $\Psi_{o,f}$, such as β and γ decay, can be described by the Fermi Golden Rule Number 2:

$$w = \frac{2\pi}{\hbar}|M_{f,i}|^2\rho(E), \tag{A.1}$$

where $\rho(E)$ is the number of final states available to the emitted particle and $M_{f,i}$ is the matrix element.

A.1 Density of Final States for β Decay

In the Fermi Theory of allowed β decay that describes the probability that a specific initial nuclear state decays to some specific final state, the number of possible decay paths is represented by the density of final states $\rho(E)$. The density of final states $\rho(E)$ is representative of the leptons that are emitted into a "continuum" of quantized states as compared to the initial and final nuclei which are definite states. The particle in a box approximation is used to determine the maximum of states available with momenta 0 to p_{max} in a three-dimensional space of volume V and length L such that V=L^3, and thus the number of available states N of a given spin projection is

$$N = \frac{1}{2}\frac{\pi}{3}(\frac{\mathrm{p}_{max}\mathrm{L}}{\pi\hbar}). \tag{A.2}$$

An additional approximation used to determine $\rho(E)$ is that the number of states between p and p+dp is continuous, and thus the derivative of the number of available states for electrons and antineutrinos is

$$\frac{dN}{d\mathrm{p}} = \frac{4\pi\mathrm{V}}{(2\pi\hbar)^3}\mathrm{p}^2. \tag{A.3}$$

The total number of states available for electron and antineutrinos is

$$\frac{dN_{tot}}{d\mathrm{p}_e d\mathrm{p}_{\bar{\nu}}} = \frac{dN_e dN_{\bar{\nu}}}{d\mathrm{p}_e d\mathrm{p}_{\bar{\nu}}}, \tag{A.4}$$

where the total momentum of the leptons is constrained by the total decay energy E_o, i.e., the Q-value of the decay. The differential total number of states can be written in terms of the total decay energy as

$$dN_{tot} = \frac{16\pi^2 \mathrm{V}^2}{(2\pi\hbar)^6 c^3}(E_o - E_e)^2 \mathrm{p}_e^2 d\mathrm{p}_e dE_o, \tag{A.5}$$

which was obtained by substituting the momentum of the antineutrino in terms of total decay energy E_o and electron kinetic energy E_e. Finally, the derivative of the total number states available for electrons and antineutrinos with respect to the total decay energy is

$$\frac{dN_{tot}}{dE_o} \equiv \rho(E_o), \tag{A.6}$$

such that the density of states is a function of only the volume, the total decay energy, and the energy of electrons emitted with momenta p_e to p_e+dp_e.

A.2 Probability of γ Transition

The absorption or emission of a photon by a bound excited state is highly dependent on the photon energy. The photon interaction can be described by the sum of two Hamiltonians: (1) the interaction between a nucleon with all other nucleons due to the strong nuclear force and (2) the interaction between a nucleon and the electromagnetic field. The perturbation potential is oscillatory in nature, and thus the matrix element of the Fermi Golden Rule can be expressed as

$$M_{f,i} = \langle \psi_f | \, \mathrm{H}_1 \, | \psi_i \rangle = \left(\frac{\hbar c}{\epsilon_o R_o}\right)^{1/2} \left[\frac{(L+1)}{L}\right]^{1/2} \frac{1}{(2L+1)!!} \left(\frac{\omega}{c}\right)^{L+1/2} \langle \psi_f | \, O_{LM}^{EL(ML)} \, | \psi_i \rangle \tag{A.7}$$

where the perturbation potential, H_1, converts an initial state, ψ_i, to a final state by the absorption or emission of a photon of the proper energy, parity, and multipole order, EL or ML, through a multipole operator: O_{LM}^{EL} and O_{LM}^{ML}, for electric and magnetic radiation, respectively. The constant ϵ_o is the vacuum permittivity. In addition, the frequency ω can be expressed in terms of photon energy as $E = \omega\hbar$. By substituting this matrix element and the density of final states:

$$\rho(E_f) = \frac{R_o}{\pi\hbar c}, \tag{A.8}$$

into the Fermi Golden Rule, similar transition probability for electric and magnetic transitions are obtained. The transition probability of both electric and magnetic types are dependent on the photon energy as $\propto E^{2L+1}$, but the angular momentum is slightly different

for EL and ML:

$$f(EL) = \frac{L+1}{L[(2L+1)!!]^2(3+L)^2} \tag{A.9}$$

$$f(ML) = \frac{L+1}{L[(2L+1)!!]^2(2+L)^2}. \tag{A.10}$$

In contrast, internal conversion is the process where the energy difference between an initial and final state is transferred directly to an atomic electron. The perturbation potential is the electromagnetic interaction as in the case of photon emission. As electric multipole radiation is predicted to take place with probabilities two orders of magnitude larger, the potential for internal conversion interactions is restricted to competition with electric multipole radiation such that the potential is expressed as due to only the Coulomb field:

$$H' = -k_c \sum_{\text{all e, p}} \frac{e^2}{|r_p - r_e|}, \tag{A.11}$$

where r_p and r_e are the radius vectors to the proton and electron and the summation is taken over all protons and electrons in the system. Due to this dependence, internal conversion become more significant as a competitive decay process for high Z nuclei, high multipole orders, and low atomic shells.

A.3 Connecting Probability of γ Transition to Decay Width and Photoabsorption Cross Section

Beginning with the probability for the transition from a initial state i to a final state f described by matrix element in Eq. A.7, the transition probability observed is the sum of transitions for all initial and final magnetic substates m_i and m_f, respectively, and is expressed as such

$$T_{i\to f} = \frac{1}{2J_i+1} \sum_{m_i,m_f} \mathrm{w}_{f,i}^{EL(ML)} = \frac{1}{2J_i+1} \frac{2}{\epsilon_0 \hbar} \frac{(L+1)}{L[(2L+1)!]^2} \Big(\frac{E_\gamma}{\hbar c},\Big)^{2L+1} |M_{f,i}|^2, \tag{A.12}$$

where $2J_i+1$ is the total number of magnetic substates. This expression for the observed average transition probability can also be described in terms of a reduced transition probability given as

$$B_{i\to f}^{EL(ML)} = \frac{1}{2J_i+1} \sum_{m_i,m_f} |\left\langle \psi_f \right| O_{LM}^{EL(ML)} \left| \psi_i \right\rangle|^2. \tag{A.13}$$

Thus, the reduced transition probability $B_{i\to f}^{EL(ML)}$ is directly related to the transition probability, and consequently the decay constant. The decay constant is directly related to the decay with Γ by

$$\Gamma = \hbar\lambda, \tag{A.14}$$

which yields a direct relationship between the decay width and $B_{i\to f}^{EL(ML)}$. In addition, as the photoabsoprtion cross section is described by a Lorentzian shape parameterized by the resonance energy, cross section and width, the photoabsoprtion cross section is then too directly dependent on $B_{i\to f}^{EL(ML)}$.

Appendix B

Additional Phenomenological γ-Ray Strength Functions

B.1 Kadmenskiĭ, Markushev, and Furman (KMF) model

The Kadmenskiĭ, Markushev, and Furman (KMF) model [59] for $E1$ strength is expressed as

$$f_{KMF}(E_\gamma, T) = \frac{1}{3(\pi\hbar c)^2} \frac{0.7\sigma_G\Gamma_G^2(E_\gamma^2 + 4\pi^2T^2)}{E_G(E_\gamma^2 - E_G^2)^2}, \tag{B.1}$$

where the resonance parameters $(E_G, \Gamma_G, \sigma_G)$ describe the centroid, width, and cross section of the Giant Dipole Electric Resonance (GDER) and the nuclear temperature of the final states is given by T.

B.2 Modified Lorentzian (MLO) model

The Modified Lorentzian (MLO) model for $E1$ strength is expressed as

$$f_{MLO}(E_\gamma, T) = \frac{1}{3(\pi\hbar c)^2} \mathcal{L}(E_\gamma, T) \frac{\sigma_G E_\gamma \Gamma_G \Gamma(E_\gamma, T)}{(E_\gamma^2 - E_G^2)^2 + E_\gamma^2\Gamma^2(E_\gamma, T)}, \tag{B.2}$$

where the scaling factor:

$$\mathcal{L}(E_\gamma, T) = \frac{1}{1 - e^{-E_\gamma/T}} \tag{B.3}$$

describes γSF enhancement due to the nuclear temperature T of the final state and the damping width $\Gamma(E_\gamma, T)$ can be expressed by various semi-empirical parameterizations [36].

Appendix C

Additional Experimental Details

The tables included here present the gain matching scale factors and calibration sources used in the experiment discussed in Chapter 3.

Table C.1: Final scaling factors after gain matching the SuN PMTs using the ^{40}K background peak. The label of individual PMTs refers to the top "T" or bottom "B" half of SuN and the first number refers to the segment of SuN, while the second number refers to the PMT within the segment.

PMT	Scaling Factor	PMT	Scaling Factor
T11	1.0656	B11	1.0342
T12	1.0093	B12	0.9569
T13	1.0772	B13	1.0323
T21	1.0730	B21	1.0216
T22	1.0	B22	0.9586
T23	1.0709	B23	1.0284
T31	1.0719	B31	1.0451
T32	1.0178	B32	0.9569
T33	1.0783	B33	1.0313
T41	1.0719	B41	1.0313
T42	1.0028	B42	0.9645
T43	1.0751	B43	1.0462

Table C.2: Sources used in calibrated segments of SuN.

Energy (keV)	Calibration Source
59.5409 (1)	^{241}Am
569.698 (2)	^{207}Bi
661.657 (3)	^{137}Cs
1063.656 (3)	^{207}Bi
1173.228 (3)	^{60}Co
1332.492 (4)	^{60}Co
2614.511 (10)	^{228}Th (^{208}Tl)

Appendix D

TALYS calculations of the ^{92}Sr(n,γ) cross section

The TALYS input file using the experimentally determine Nuclear Level Density (NLD) and γ-ray Strength Function (γSF) is given below. The neutron resonance parameters calculated by TALYS using the experimentally determined NLD and γSF reproduced the estimated values used in the BSFG model normalization approach: D_0=20.41 keV and $\langle\Gamma_\gamma\rangle$=132.76 meV.

```
#
# TALYS input file, 92Sr(n,g)93Sr
#
# b-Oslo EXPT INPUT FOR NLD & GSF
#

projectile n
element sr
mass 92
energy energies.txt
massmodel 2

transeps 1.00E-15
xseps 1.00E-25
popeps 1.00E-25
preequilibrium y
#outspectra y
fileresidual y

# THIS IS NOW CT MODEL EXTRAPOLATION WITH FERMI GAS SPIN DISTRIBUTION
ldmodel 4
ptable 38 93 0.0
```

```
ctable 38 93 0.0

# Use first 20 discrete levels
Nlevels 38 93 20

# GAMMA STRENGTH FUNCTIONS
# Gamma strength: tables for the E1 and M1 components
E1file 38 93 E1_gsf_93Sr_TALYSformat.txt
M1file 38 93 M1_gsf_93Sr_TALYSformat.txt
gnorm 1.



# global parameters for the n-OMP
localomp y

outlevels y
outdensity y
outgamma y

# astro n to get cross section, astro y to get rates and MACS
astro n
#astro y
```